POLYMER NANOCOMPOSITE-BASED WIDE BAND STRAIN SENSOR FOR 3D FORCE MEASUREMENT USING PIEZOELECTRIC AND PIEZORESISTIVE DATA FUSION

by

Ahmed Mohammed H. Al Otaibi

A Dissertation

Submitted to the Faculty of Purdue University

In Partial Fulfillment of the Requirements for the degree of

Doctor of Philosophy

School of Mechanical Engineering

West Lafayette, Indiana

August 2021

THE PURDUE UNIVERSITY GRADUATE SCHOOL
STATEMENT OF COMMITTEE APPROVAL

Dr. Sohel Anwar, Co-Chair

School of Engineering and Technology, IUPUI

Dr. George T. Chiu, Co-Chair

School of Mechanical Engineering

Dr. Mangilal Agarwal

School of Engineering and Technology, IUPUI

Dr. Martin Byung-Guk Jun

School of Mechanical Engineering

Approved by:

Dr. Nicole L. Key

ACKNOWLEDGMENTS

I would like to thank my wife Maram, my parents Mohammed and Hawa, my kids Mohammed, Rose, and Bayan, my sisters, and my little brother for their help, support, and encouragement during my PhD studies.

I would like to thank Prof. Sohel Anwar, the Co-Chair of my committee, for his constant assistance, encouragement, guidance, and the tremendous amount of support and opportunities he provided me throughout my doctoral studies. He has provided me with endless encouragement and guided me through the multitude of challenges to be expected in conducting any research doctorate. I know I cannot thank my mentor and adviser Prof. Sohel enough, but at least I can promise that I will try to be a similar coach and mentor to my own students in the future.

I would like to thank Prof. George T. C. Chiu, the other Co-Chair of my committee, for encouraging me to determine appropriate solution methodologies. He spent time discussing my research, evaluating topics for me to investigate, and providing me with countless ways to improve upon my dissertation.

I would like to thank Prof. Mangilal Agarwal for his support and attentiveness during the fabrication process, the characterization of the nanocomposite, and for providing the necessary assistance and academic resources. Also, I would like to thank his former PhD student, Dr. Ali Daneshkhah, and current graduate students Pias Kumar Biswas and Asel Habarakada Liyanage for their support during our work at the INDI lab.

I would like to thank Prof. Martin Byung-Guk Jun for his advice, references about my research topic, and insightful discussions. Evaluating new topics with him was always interesting for me to investigate and he often provided me with alternative ways to improve my dissertation.

TABLE OF CONTENTS

LIST OF TABLES

LIST OF FIGURES

ABSTRACT

Polymer nanocomposites (PNC) have an excellent potential for in-situ strain sensing applications in static and dynamic loading scenarios. These PNCs have a polymer matrix of polyvinylidene fluoride (PVDF) with a conductive filler of multi-walled carbon nanotubes (MWCNT) and have both piezoelectric and piezoresistive characteristics. Generally, this composite would accurately measure either low-frequency dynamic strain using piezoresistive characteristic or high-frequency dynamic strains using piezoelectric characteristics of the MWCNT/PVDF film sensor. Thus, the frequency bands of the strain sensor are limited to either piezoresistive or piezoelectric ranges. In this study, a novel weighted fusion technique, called Piezoresistive/Piezoelectric Fusion (PPF), is proposed to combine both piezoresistive and piezoelectric characteristics to capture the wide frequency bands of strain measurements in real-time. This fuzzy logic (FL)-based method combines the salient features (i.e., piezoresistive and piezoelectric) of the nanocomposite sensor via reasonably accurate models to extend the frequency range over a wider band. The FL determines the weight of each signal based on the error between the estimated measurements and the actual measurements. These weights indicate the contribution of each signal to the final fused measurement. The fuzzy inference system (FIS) was developed using both optimization and data clustering techniques. In addition, a type-2 FIS was utilized to overcome the model's uncertainty limitations. The developed PPF methods were verified with experimental data at different dynamic frequencies that were obtained from existing literature. The fused measurements of the MWCNT/PVDF were found to correlate very well with the actual strain, and a high degree of accuracy was achieved by the subtractive clustering PPF's FISs algorithm.

3D force sensors have proven their effectiveness and relevance for robotics applications. They have also been used in medical and physical therapy applications such as surgical robots and Instrument Assisted Soft Tissue Manipulation (IASTM). The 3D force sensors have been utilized in robot-assisted surgeries and modern physical therapy devices to monitor the 3D forces for improved performances. The 3D force sensor performance and specifications depend on different design parameters, such as the structural configuration, placement of the sensing elements, and load criterion. In this work, different bioinspired structure

configurations have been investigated and analyzed to obtain the optimal 3D force sensor configuration in terms of structural integrity, compactness, the safety factor, and strain sensitivity. A Finite Element Analysis (FEA) simulation was used for the analysis to minimize the time of the development cycle.

A tree branch design was used as the 3D force sensor's elastic structure. The structure was made of aluminum with a laser-cutting fabrication process. The PVDF/MWCNT films contained piezoresistive and piezoelectric characteristics that allowed for static/low strain measurements and dynamic strain measurements, respectively. Two compositions with 0.1 wt % and 2 wt.% PVDF/MWCNT sensing elements were selected for piezoelectric and piezoresistive strain measurements, respectively. These characteristic measurements were investigated under different vibration rates in a supported beam experiment. The 3D force sensor was tested under dynamic excitation in the Z-direction and the X-direction. A Direct Piezoresistive/Piezoelectric Fusion (DPPF) method was developed by fusing the piezoresistive and piezoelectric measurements at a given frequency that overcomes the limited frequency ranges of each of the strain sensor characteristics. The DPPF method is based on a fuzzy inference system (FIS) which is constructed and tuned using the subtractive clustering technique. Different nonlinear Hammerstein-Wiener (nlhw) models were used to estimate the actual strain from piezoresistive and piezoelectric measurements at the 3D force sensor. The DPPF method was tested and validated for different strain signal types using presumed Triangle and Square signal waves data. The DPPF has proven its effectiveness in fusing piezoresistive and piezoelectric measurements with different types of signals. In addition, an Extended Direct Piezoresistive/Piezoelectric Fusion (EPPF) is introduced to enhance the DPPF method and perform the fusion in a range of frequencies instead of a particular one. The DPPF and EPPF methods were implemented on the 3D force sensor data, and the developed fusion algorithms were tested on the proposed 3D force sensor experimental data. The simulation results show that the proposed fusion methods have been effective in achieving lower Root Mean Square Error (RMSE) than those obtained from the tuned nlhw models at different operating frequencies.

1. INTRODUCTION

Sensors are both fundamental and essential for many 21^{st} century applications, such as biochemical and medical diagnoses [1], [2], industrial and fabrication processes [3], and environmental and structural health monitoring [4], [5]. A sensor converts a physical phenomenon into an electrical signal. The signal is then processed and calibrated to ensure that the measurements obtained are both accurate and reliable. As industry technologies develop, new sensors which provide increased accuracy,improved quality, more capacity must also be developed. Specifically, strain and force sensors have gained much attention in recent years because they are applied in new, 21^{st} century contexts such as surgical robots [6], polishing machines [7], and biomedical and physical therapy instruments. [8]–[11].

In the past, different sensing technologies have been implemented in various contexts to obtain strain and force measurements. For example, strain gauges, piezoelectric ceramics, capacitance, fiber brag grating and most recently, laser beam diffraction using knife edges have all been used and investigated in the medical and industrial fields. These types of sensors still present challenges because they require complex signal conditioning, have complex structures, and are sometimes constructed from very expensive materials. In addition, shape and flexibility are also limitations for these technologies. Today, most load cells use metallic foil strain gauges because they are both affordable and accurate; however, they have too have limitations, such as low gauge factors, low resistance, and temperature-dependant drift. Consequently, foil strain gauges are not suitable for the miniature and high-resolution applications necessary for 21^{st} century contexts [12].

Recently, Polymer Nanocomposites (PNCs) have attracted much attention in the material science and engineering fields due to their unique characteristics. To construct these composites, a polymer matrix is combined with non-organic fillers. One of the non-organic fillers is in a nanoscale dimension. The resulting composite retains the advantages of both the original polymer matrix and the added filler. Because of these advantages, the properties of CNTs have been deeply investigated by many researchers and have been shown to possess extraordinary mechanical, electrical, optical, and thermal properties. For example, Carbon Nanotubes (CNTs), discovered in 1991 by Iijima [13], greatly advanced the nanocomposite materials field. CNTs implemented in different Polymer Nanocomposites applications because of their mechanical [14], [15], electrical [16], [17], optical [16], and thermal [15], [18], [19] properties. Specifically, CNTs have a one dimensional structure and a high aspect ratio (length-to-diameter ratio), which makes them conducive fillers for producing electrically conductive PNCs [20]. As a result, high conductivity PNCs can be achieved with a lower concentration of CNT compared to other conductive nano-fillers.

The percolation threshold of PNC-CNT has a significant influence on the sensing elements' performance and sensitivity. The percolation threshold, or the percentage concentration of the conductive nano-filler inside the composite at which the electrical resistivity of the composite increases significantly [21], is also influenced by the aspect ratio of the nano-filler inside the composites [22], [23]. The volume fraction, conductivity, and topology of the nano filler networks, and interaction between the polymer and fillers also control the PNC's overall conductivity [24], [25]. For strain measurement, the PNC-CNT's piezoresistivity is influenced by the demolition of the conductive networks, tunneling resistance, and the changes of the CNT piezoresistivity [26]. However, the CNT piezoresistivity changes are less influenced due to the relatively small change in resistance [27]. The tunneling resistance occurs between the crossings or the neighboring of the CNTs, and it is the most dominant factor in the overall composite conductivity [28].

Polyvinylidene Fluoride (PVDF), a type of polymer matrix, has been widely studied and used for piezoelectricity based sensing and actuation applications because of its affordable cost, mechanical characteristics, and chemical stability. PVDF has been used in force/pressure sensing, energy harvesting, humidity and gas flow sensors, and acoustic and ultrasonic sensors [29]–[35]. Several researchers have investigated the advantages of mixing CNT with PVDF. The presence of multi-walled CNTs (MWCNTs) advances the electromechanical characteristics of the composite [36] and the piezoelectric properties of the MWCNT/PVDF films are activated at lower voltages due to the presence of the CNT, whereas the PVDF films alone need higher voltages [37]. Moreover, CNTs change the formations of the semi-crystalline structure from the α phase to the β phase, which is where the highest polarization can be achieved [38].

The PVDF/MWCNT sensors have piezoresistive and piezoelectric properties which make them unique, wide-band strain transducers. Static or low and high excitation strain measurements can be measured using the piezoresistive and piezoelectric characteristics, respectively. Several attempts to combine and fuse these characteristics have been made using either the optimum linear smoother-based method[39] or the stack fabrication process [40], [41]. In one particular study [39], the fusion method uses a constant weighting for each signal through different frequency bands. Additionally, the smoothing technique generally relies on future measurements, resulting in measurement delay. In the tactile sensors [40], [41], only one characteristic can be used at a time and no fusion algorithm was proposed because that would result in limiting the operating frequency to either static/low or high excitation strain measurements. The PVDF/MWCNT sensor has a great potential for different 21st century applications, including lower and higher dynamic measurements.

3D force/torque (F/T) sensors have been frequently used in diversified engineering applications to measure the three axial forces (Fx, Fy, Fz) and the three axial moments (Tx, Ty, Tz) simultaneously. 3D force sensors are essential in many robotic, medical, and machining applications for quantifying the three axial forces due to the higher precision needed at these applications. Some of these applications are surgical robots [6], polishing machines [7], and biomedical and physical therapy instruments [8]–[10], [42]. The forces are monitored so the instruments can successfully complete task monitoring, excessive force prevention, and precision placement. These 3D force sensors typically consisted of an elastic structure and sensing elements which quantify the strain at the elastic structure. Both elements significantly influence the sensor performance and criteria [8]. Furthermore, cross-coupling between the axes' measurements is a limitation that affects the sensor. Several mechanical and bioinspired structures have been used for the 3D force sensors, such as a cross beam [43], a parallel mechanism [44] and a Stewart platform [45], and tree branches [46]. Some structure configurations could potentially minimize the cross-coupling and improve the sensor's performance despite the configuration's complex structure and the expensive materials required [47].

In the last few decades, nature has been a great motivation and solution for multiple engineering problems. Features such as structure, shape, and mechanisms of motion have been drawn from animals, plants, and microorganisms. These features have been implemented in robotics applications such as soft robotics [9]. As a result, bio-inspired and bio-mimicry engineering has attained a great attention in the 21st Century. In addition, many force and tactile sensors have taken advantage of the flexibility and uniqueness resulting from designs inspired by biological structures [48].

1.1 Problem statement and objectives

After extensive investigation and reviewing the relevant research studies, different limitations have been identified with the MWCNT/PVDF strain sensors and 3D force sensors. The *in situ* MWCNT/PVDF nanocomposite strain sensor has the potential to capture both low and high-frequency dynamic strain measurements using both piezoresistive and piezoelectric measurements, respectively. However, the strain sensor's band frequencies are limited to either piezoresistive or piezoelectric, depending on the design or measurements criteria. Also, the 3D force sensor operating frequency is limited by the sensing elements characteristic of either lower or higher frequency strain measurements. In addition, the 3D force sensors' structure configurations affected the sensor sensitivity and measurements coupling. The objective and the proposed solution for the identified problems are proposed in the following subsections.

The first objective is to develop a real-time weighted fusion technique to combine piezoresistive and piezoelectric broadband dynamic strain measurements. This technique aims to overcome the piezoresistive and piezoelectric characteristic frequency-dependent limitation using a weighted combination of both measurements. The frequency response of piezoresistive and piezoelectric characteristics was investigated at different frequencies up to 1000 Hz dynamic loading strain. The proposed fuzzy logic-based PPF methods were developed and verified with experimental data at different dynamic frequencies using a 3D force sensor's experimental data and data presented in the literature [39]. The PPF methods could be applied to different sensing applications where frequency or other phenomena influencing their performance. The proposed fusion algorithms have the potential to improve the overall CNT-PNC strain sensor's accuracy by fusing both piezoresistive and piezoelectric strain measurements at different operating frequency ranges. Different CNT-PNC fabrication processes were investigated and optimized in this work, including spray coating and electrospinning techniques.

The 3D force sensor performance is influenced by structural configuration, sensing elements placements, and load criterion. Different bio-inspired structure configurations have been investigated and analyzed for their sensitivity and force coupling in this work. One of the main objectives of this work was to obtain the optimal 3D force sensor configuration in terms of structural integrity, compactness, safety factor, and strain sensitivity. Finite Element Analysis (FEA) simulation was used to investigate the structure configuration performance at different loading scenarios. The *in situ* 0.1 wt.% and 2 wt.% MWCNT/PVDF strain sensors were fabricated using a spray-coating process and were chosen for piezoelectric and piezoresistive strain measurements at the fabricated 3D force sensor, respectively. The proposed PPF methods were implemented to generate a 3D force sensor that would measure forces over a wide range of frequencies. The produced 3D force sensor is designed to measure 60 N along the X-axis and Y-axes, a force of 100 N in the Z direction, and operate at frequencies up to 100 Hz.

2. LITERATURE REVIEW

2.1 MWCNT/PVDF Nanocomposites Strain Sensor

The MWCNT/PVDF composite film is a unique sensing element that can measure strain using either piezoresistive or piezoelectric properties. The piezoresistive strain measurement is appropriate for static or low loading frequencies. By contrast, the piezoelectric strain measurement can capture high frequency measurements with high sensitivity and accuracy. The piezoresistivity of the composite film was characterized by Zhihui et al. [49] who reported that a hot pressed 1 wt.% MWCNT/PVDF film was less sensitive at high frequency (2000 Hz) than a 6.5 wt.% carbon black (CB)/PVDF strain sensor. Furthermore, another study has shown that 1 wt.% MWCNT/PVDF film failed to match the output from 1 wt.% Graphene/PVDF and 6 wt.% CB/PVDF films at 200 Hz dynamic loading [50]. Piezoelectric measurements were taken by sandwiching a MWCNT/PVDF film between two polypropylene (PP) films and applying compression loads ranging from 200 N to 350 N at a low frequency (0.5 Hz) [51]. The piezoelectric output voltage was relatively small at a high magnitude force of 200 N. A mechanically stretched and electrically poled (corona poling) PVDF/MWCN strain sensor that is frequency dependent was reported by Park et al. [39]. For obtaining strain measurements below 5 Hz, the piezoresistive sensing provided accurate measurements whereas piezoelectric sensing offered accurate measurements for strain measurements above 5 Hz up to 1000 Hz [39]. For optimal piezoresistive and piezoelectric strain-sensing performance, 0.1 wt.% and 2 wt.% of CNT exhibited better accuracy, respectively [39].

Frequency-dependent strain measurements are affected by multi-label parameters such as the composite's electrical, mechanical, and physical properties, all of which ultimately contribute to the sensor's performance. In terms of piezoresistivity, the gauge factor (GF) and the matrix's mechanical response places an upper bound on the measurement's amplitude at high frequencies [49]. In addition, the complex viscosity of a compressed molded MWCNT/PVDF composite sample decreases with increasing frequency [52]. A decreased complex viscosity limits the movement of the CNTs with respect to each other and reduces the tunneling resistance changes. Nevertheless, the carbon nanofiller volume fraction and dispersion, both of which are affected by the fabrication process, have a significant effect on a sensors' performances. For piezoelectricity, the strain coefficient D33 is greater than D31 for lead zirconate titanate (PZT) and PVDF materials. Consequently, the resonant frequency mode of D33 limits the measurements at which low-frequency vibration is desirable [53].

Researchers have attempted to combine both piezoresistive and piezoelectric characteristics to capture both static and dynamic mechanical stimulation using a stake fabrication process. For example, He et al. [40] introduced a multi-layered piezoelectric-piezoresistive tactile sensor. The sensor consisted of three electrodes layers: a piezoelectric layer, a piezoresistive layer, and a common electrode layer. The piezoelectric and piezoresistive layers were made of PVDF (-TrFE) and MWCNTs/ Polyurethane (PU). Similarly, Khan [41] reported two multi-layered pressure sensors made from (PVDF-TrFE) and (PVDF-TrFE)-MWCNTs sensing materials using screen-printing technology. These studies introduced sensors that have the capability to measure both static and dynamic measurements. However, each measurement was performed with fixed connections or setup; that is, either static or dynamic, but not both.

The PVDF, which is considered a semi-crystalline material, has four distinct conformations: the α phase, the β phase, the γ phase, and the δ phase [54]. In the β phase, the C-F bonds are polar, all dipoles are aligned in the same direction, and the high polarization could be attained [39]. On the other hand, all dipoles are placed in random directions in the α phase, resulting in zero polarization. Therefore, the α phase should be converted to the β phase and a longer β phase is needed to produce a more sensitive piezoelectric sensor. Several techniques have been used to achieve this purpose, including mechanical stretching, solution casting, electric poling, spin coating, and electrospinning [55]. Additionally, sequential mechanical stretching and electric poling have been found to be effective in enhancing the presence of the β phase in the PNC piezoelectric film [56]–[58]. Fourier-Transform Infrared Spectroscopy (FTIR) was used to determine the presence of these phases before and after treatment. The absorbance peak at 840 cm^{-1} is signature for both β and γ phases [59]. Also, the β phase has an absorbance peak at the band 1279 cm^{-1}. Another study has identified similar values for β phase and recorded observed peaks at 765 cm^{-1}, 795 cm^{-1}, and 975 cm^{-1} for the α phases [60]. In this study [61], contact poling was used on the MWCNT/PVDF nanocomposite specimen and the capacitance was increased by 64.44 %.

2.2 Modeling of the CNT-PNCs

To understand the electromechanical properties of polymer nanocomposites, many researchers have constructed theoretical models. These models are used to generate estimates for percolation threshold, electrical conductivity, and other electromechanical properties of PNCs. Different approaches have been utilized to construct these models, including statistical, geometric, or thermodynamic models, sometimes with the help of structure-oriented models [62]. Several other methods have been introduced in the literature to simulate and characterized the CNT-PNCs' properties, including the Representative Volume Element (RVE) [39], Molecular Dynamics [63], the Continuum Method [64] and the Molecular Structural Mechanics Method [65]. The Finite Element Method (FEM) has also been used in these models. However, several assumptions have been considered in these models which could lead to less accurate predictions of the electromechanical properties of polymer nanocomposites.

Despite these assumptions, the Representative Volume Element (RVE) has been used to simulate the CNT-PNCs with high accuracy. The RVE represents the whole system with the smallest measurable unit [66]. Li et al. [65] have constructed a RVE model which considered CNTs directly inside the polymer matrix which is not the case in using most of the PNC fabrication processes. In another study [67], they introduced a PNC's RVE that takes the waviness of the CNTs into account without considering the dispersion of the CNTs inside the matrix. Shi et al. [68] came up with a more sophisticated RVM model that has both CNTs' distribution and waviness attributes. Many of these CNT-PNC modeling studies use a probabilistic method to randomly distribute the CNT and generate CNTs with random geometries in the RVE model to accurately represent the reality and estimate the mechanical properties of the PNC [69], [70]. Li et al. [71] found the highest electrical conductivity can be achieved for any PNC when CNTs are randomly aligned at an angle between 70 - 80 °.

The piezoresistive characteristic of the CNT-PNCs mainly depends on the internal conductive network of the CNTs inside the polymer nanocomposite. One study [72] explored the effect of this microstructure on electrical conductivity, including short fiber, as it was modeled under finite strain. The effective conductivity is estimated based on the power-law conductivity relationship. In another study [73], a 3D statistical model consisting of a resistance network was constructed to predict the resistance change under applied strain. The model used both the tunneling resistance and the random distribution of CNTs inside the composite to evaluate resistance change. A mathematical model was proposed by Ramaratnam et al. [36] to estimate the piezoelectric properties of the MWCNT/PVDF and verified using experimental results. Park et al. [39] predicted the piezoelectric coefficient of the PNC using a 2D Monte Carlo numerical simulation. Taken together, these modeling methods are excellent tools for analyzing the electromechancial properties of CNT-PNCs. However, they are often computationally expensive and not practical for real time application.

Other researchers have used the Electrochemical Impedance Spectroscopy (EIS) technique to evaluate the conductivity of CNT-PNCs and the degree of CNTs' alignment [61], [74]. The EIS model is an equivalent circuit model with different structures that are used to represent the overall resistance and capacitance relation of the sensor with respect to the AC frequency variation, but not the excitation frequency. Despite the tremendous amount of literature that records efforts to understand the electromechanical properties of the CNT-PNCs, none of them has had the effect of excitation frequency on strain measurement in their models.

Finally, R-C equivalent circuit piezoresistive models have been used in different civil engineering applications. Garcia et al. [75] have proposed an R-C equivalent circuit piezoresistive model which considers the effect of frequency on strain measurements in [76] a Cement/CNT nanocomposite. An electrode for resistance is connected in series with two R-C circuits which are connected in parallel.. The first R-C circuit represents internal resistance and capacitance changes and the second for interface path. A current source is connected in parallel with first the R-C component to simulate the effect of frequency on strain measurement. Finally, the model's parameters are fitted under compression tests.

2.3 Sensors' data fusion

Sensor fusion is a method that combines multiple sensory measurements which could be of similar or different types of signals and are not sufficient by themselves to provide a useful output. Data fusion may be necessary in different applications including military applications, law enforcement, remote sensing, automated monitoring of equipment, medical diagnosis, and robotics [77]. Any sensor measurements are subject to limitations such as if the measurement is restricted to a narrow area of an otherwise broad environment [78]. Similarly, image fusion is the process of combining features from different images to produce a higher quality image [79]. Fuzzy set theory has been implemented in different image processing and image fusion algorithms. A novel image fusion algorithm, which was based on two-scale image decomposition integrated with fuzzy set theory and image morphology, was introduced by Zhang et al. [80]. They presented a new fusion method based on Non-Subsampled Contourlet Transform (NSCT) with intuitionistic fuzzy sets for the infrared and visible image fusion [80]. Yang et al. proposed a novel multimodal sensor medical image fusion method based on Type-2 Fuzzy Logic in NSCT domain [81]. The image fusion method has retained more informative and higher-quality fused medical images by using the fuzzy logic. The fuzzy set-based image fusion algorithms have shown more effective fusion performance than other conventional image fusion methods [82].

Park et. al. [39] proposed a fusion methodology for the piezoelectric and piezoresistive MWCNT/PVDF nanocomposite sensors. The technique is analogous to an optimum linear smoother developed by Fraser and Potter in 1969, which combines two optimal linear filters or estimates [83]. The fusion equation uses piezoelectric and piezoresistive signals, compensation coefficients, and their covariances to compute the final fused signal [39]. The compensation coefficients were fixed during the transitioning frequencies (5 - 160 Hz) bands, which might lead to measurement data being lost and any resonant frequency effects being excluded. An accurate and robust frequency-based fusion method for real-time strain measurement is needed to overcome the stated limitation and the disadvantages of previous attempts to combine both piezoresistive and piezoelectric characteristics.

In the current strain sensing technology, the piezoresistive and piezoelectric characteristics are sensitive and accurate at low- and high-frequency measurements, respectively. A Kalman Filter Fuzzification (KFF) is used for estimating the measurements of position, velocity, and acceleration in a 3D target tracking application [84]. In this method, the Kalman Filter

(KF) estimated the state for each measurement and associated each estimate with different scalar weights [85], [86]. The final fused estimate is calculated using 5.1 [85], [86]:

$$\hat{X}_f^{KFF}(k) = w_1\hat{X}_1^{KF}(k) + w_2\hat{X}_2^{KF}(k) \tag{2.1}$$

Where w_1 and w_2 are the weight for each sensor in the final measurement and $\hat{X}_1^{KF}$ and $\hat{X}_2^{KF}$ are the estimate for the KFs of each sensor. The w_1 and w_2 are generated by the Fuzzy Inference System (FIS) for both sensors. These weights define the contribution of each signal to the final fused state. They are generated by the Fuzzy Inference System (FIS) for both sensors based on the calculated normalized errors between the estimates and the actual measurements. Sensor fusion is a great tool to advance and improve the MWCNT/PVDF strain sensors' sensitivity by combining both characteristics using a more sophisticated fusion method.

Despite the fact that MWCNT/PVDF strain sensors' characteristics are frequency dependent, few researchers have addressed these limitations and these characteristics not being dealt with in depth with regards to sensor fusion. Consequently, the aim of this work is to overcome the piezoresistive and piezoelectric characteristic frequency dependent limitation using a weighted combination of both measurements when necessary. Here, a novel fuzzy logic-based PPF fusion method has been designed, developed, and verified with experimental data at different dynamic frequencies that were presented in the Park et al. study [39]. This technique can be generalized to any other sensor fusion methods where performance is frequency-dependent. Finally, the uniqueness of this work is that it is a frequency-based real-time measurements fusion method that efficiently weights each signal to achieve an accurate estimate. Most prior research on such sensors studied their performance under a fixed measurement setup, e.g. either static to low frequency ranges or high frequency ranges. The proposed fusion algorithm has the potential to improve the overall accuracy in fusing both piezoresistive and piezoelectric strain measurements over a wide frequency range for a PNC strain sensor.

2.4 3D force sensors

The performance of a 3D force sensor is influenced by structure configuration, the placement of sensing elements, and load criterion. Key design parameters include improving the cross coupling, isotropy, and stiffness and sensitivity. These parameters are influenced by structure's configuration of the sensor [8]. Different structure configurations have been used to overcome these issues by implementing various structure mechanisms and arrangements. Some of these structures are the cross beam [43], the parallel mechanism [44] and the Stewart platform [45]. Some structures have obtained good cross-coupling and high-range characteristics. However, they are bulky, complicated and made of expensive materials.

In Yao et al, a six-axis F/T sensor with eight parallel limbs was constructed from titanium alloy powder using 3D printing technology [87]. These strain gauges were used as sensing elements for strain measurements. The measurements were then used to derive the F/T measurements using a calibration matrix. The sensor measured force and torque ranges of 150 N and 3.5 Nm along and about the three 3D axes, respectively. However, the sensor diameter was 108 mm which made it difficult to embed such a sensor in many small-to-medium robotics applications.

Another strain gauge based six-axis F/T sensor has been implemented for a humanoid robot foot [88]. The sensor was made of stainless steel and had ranges of Fz = 1000 N, Fx = Fy = 400 N, Tz = 10 Nm and Tx = Ty = 20 Nm. A great thickness reduction to 12 mm was achieved by using two layers of cross-beam structures; however, the sensor diameter was still 50 mm. A six-axis F/T force was designed based on six capacitive centrodes attached to a PCB and a ground plate which acted as the elastic structure [89]. The elastic structure was made of aluminum 7075 and the sensor was constructed using seven different part with a thickness of 19 mm. The sensor could measure force and torque ranges of 50 N and 1 Nm along and about the 3D axes, respectively.

Finite Element Analysis (FEA) is an effective way to understand how any mechanical structure becomes deformed, stressed or strained in response to applied loads. This analysis facilitates the design process using a computer-aided design (CAD) model and simulates the feasibility and performance of a component before moving to the actual prototyping stage. As a result, designers and industries have achieved great time and expense reduction by incorporating FEA in their production processes. In this work, different bio-inspired 3D force sensors were designed and analyzed using virtual prototyping for compact design, safety factor and strain sensitivity.

2.5 Applications

The PVDF/MWCNT strain sensor is proposed to be used for *in situ* strain measurement and structural health monitoring applications such as civil structures, aerospace, and machining. This sensing element is sprayable to any complex structure including machining tools and tables. The PPF method is a potential application for any transducer whose performance is influenced by the operation frequencies. The system of PVDF/MWCNT strain sensor and PPF will result in a wide band strain-sensing element. The 3D force sensors have very diverse applications including various robotics applications, machine tools, and tables where applied force measurements are needed. Applied force measurements are often needed in prosthetics research, physical therapy and rehabilitation research, automation, and automotive testing and research.

In the physical therapy and rehabilitation field, 3D force sensors have been used in different Instrument Assisted Soft Tissue Mobilization (IASTM) devices to quantify the applied 3D force measurements during the treatment. The MWCNT/PVDF nanocomposite sensing elements would help miniaturize and enhance the flexibility of these IASTM devices. In addition, the proposed PPF methods could be implemented with the proposed 3D force sensor at different treatment frequencies.

3D force sensors have been utilized at different surgical robots' arms due to their higher precision measurements and task mounting capability. A 3D force sensor based on *in situ* MWCNT/PVDF nanocomposite sensing elements could minimize the robot arm size and produce more compact surgical robots. In addition, complex surgical tools are used in the field of conventional surgical procedures. The *in situ* nanocomposite sensing elements can be used to monitor the applied forces during procedures. That can be accomplished with single sensing elements for 1D force measurement or multiple sensing elements for 2D or

3D force measurements. Where the MWCNT/PVDF sensing elements are attached to their structures.

3. DEVELOPMENT OF 3D FORCE SENSOR

3.1 Design criteria of 3D force sensor

In a F/T sensor, the relationship between the applied force and the measured strain is assumed to be linear and to operate in the elastic region [43]. This relationship is governed by the calibration $[C]$ matrix which represents the contribution weight of each sensing element's placement or bridge circuit as a result of a pure unit loading. In the case of 3D force measurement, the relationship can be represented as shown in Equation 3.1.

$$\vec{S}_{3\times1} = [C]_{3\times1}\vec{F}_{3\times1} \tag{3.1}$$

The output strain from the sensing elements or bridge circuit is stored in the n×1 strain output vector $\vec{S}$. Because there are three axes where measurements are taken, n=3 $\vec{F}_{3\times1} = [F_x, F_y, F_z]^T$. The calibration matrix can be derived using a physical experiment by applying a pure unit loading and defining the strain contribution at each bridge or at the placement of the sensing elements. The purpose of this study was to build bio-inspired elastic structures for a 3D force sensor with an overall diameter of 20 mm, high force ranges (Fx = Fz = 60 N and Fy (normal) = 100 N) and a maximum thickness of 10 mm. In addition, these elastic structures were investigated and analyzed for deformations, equivalent stresses, the factor of safety, and sensitivity.

3.2 Structure and sensing elements configurations

Four bio-inspired 3D force sensors structures were modeled in Creo Parametric 4.0 [90]. These designs were a spider, a turtle, a modified turtle, and tree branches. All the modeled designs were based on their natural biological structure. Each bio-inspired structural body responded in its own way to the applied 3D force, which will be discussed in the following section. All designs have a diameter of 20 mm, a maximum height of approximately 10 mm, and a bolt hole with diameter of 2 mm for loading mounting. 3D forces were applied at the bolt hole.

The spider design has four legs instead of eight because of the size constraint of the proposed sensor, as shown in Figure 3.1, b. Spider legs are very complex structures. Each leg consists of seven parts: 1) coxa, 2) trochanter, 3) femur, 4) patella, 5) tibia,6) metatarsus, 7) tarsus and claws [91]. The three larger parts, the femur, the tibia, and the metatarsus, were considered to be the sensor's elastic beam which was oriented in a similar way to a spider's actual leg. The sensor consisted of an inner upper ring with a diameter of 6 mm, an outer lower ring with a diameter of 20 mm, and four connected beams. Four sensing elements placements were chosen to cover the inclined flat areas, as shown in Figure 3.1, a. Each sensing element's placement had an abbreviation of $f_{\#}$, where # indicated the associated axis' direction, arm or beam on which the strain's sensing element attached. The sensing element placement's area was approximately 23.6 mm^2 with an upper side beam's width of 2.8 mm, lower side beam width of 4.3 mm, and a wall thickness of 1.7 mm.

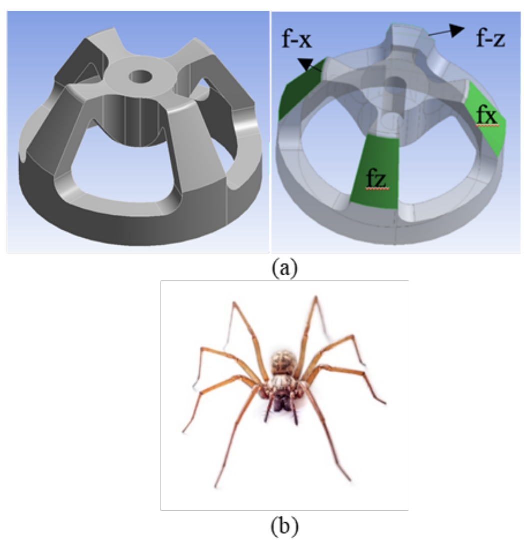

Figure 3.1. Spider 3D force sensor cad model and sensing elements' placements (a) And a real spider [92] (b).

Turtles have a very strong structure configuration, having both an internal and external skeleton, as shown in Figure 3.2, b. The external skeleton grants a turtle safety and support of their internal origins, it possesses a skeletal shell, which consists of the lower plastron and the upper carapace [93]. A turtle' carapace is an approximately convex shaped part of the turtle's structure [94]. Thus, because of the size constraint, the turtle elastic structure was constructed using four ribs. Four sensing elements were assigned to cover the inclined convex areas at each beam, as shown in Figure 3.2, a. The sensing element placement's areas were approximately 30 mm^2 each with side beam's width of 5 mm and wall thickness of 2 mm.

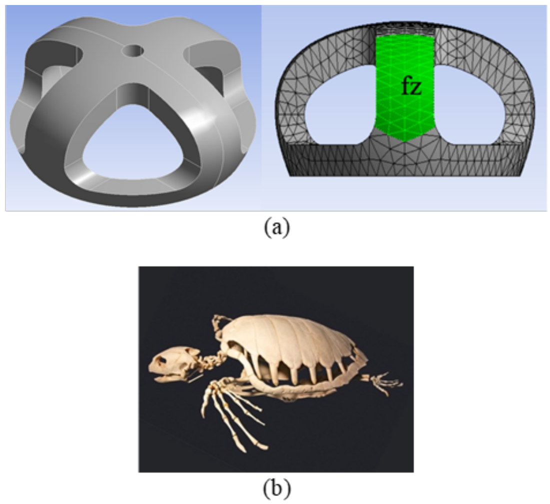

Figure 3.2. Turtle 3D force sensor cad model and sensing elements' placements (a) And a turtle skeleton [93] (b).

As shown in Figure 3.3, the turtle design was modified by reducing the rib's width to approximately 1.7 mm and by increasing the shell's thickness to 3 mm to investigate different sensing element's placement along the thickness of the beams. In addition, a cylinder with outer diameter and height of 4 mm was inserted as an inner ring to strengthen the sensor structure around the loading mounting area. Eight different sensing elements were assigned to the right side of each of the ribs to investigate the force measurements. Using both sides of the ribs would be useful for 3D torque measurements and will be investigated in future study. The area and width of each sensing element placements was approximately 18 mm^2 and 3 mm, respectively.

Tree's branches are excellent elastic structures that can resist different severe weathers scenarios and natural forces. The tree branch's elastic structure sensor was designed to mimic the upper view distribution of tree branches, as shown in Figure 3.4, a, b. This design consisted of inner and outer rings with diameters of 6 mm and 20 mm, respectively. The sensor had four main branches and each branch divided into two branches near the outer rings, connecting the rings together. This shape increased the sensor's stiffness and secured

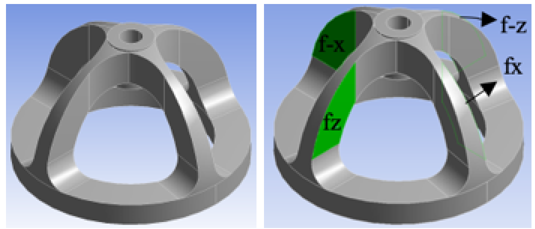

Figure 3.3. Modified turtle 3D force sensor cad model and sensing elements' placements

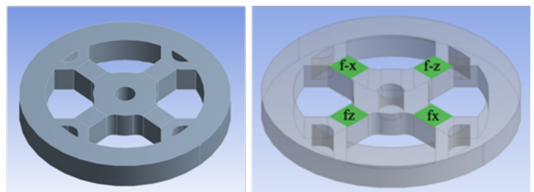

(a)

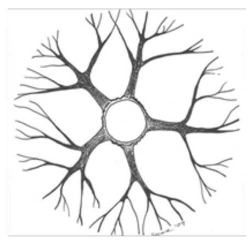

(b)

Figure 3.4. Tree branches 3D force sensor cad model and sensing elements' placements (a) And tree branches top view [95] (b).

the structure against excessive normal forces. The sensors placements were assumed to be attached to the surface of the areas between the inner hub and the branches separations, as shown in Figure 3.4, a. The area of each sensing element placement was approximately 5.75 mm^2 with a beam's width of 2 mm and the sensor's overall thickness of 2 mm.

Finally, the traditional Maltese cross beam structure, widely used for a 3D force sensor as an elastic structure, has been modeled for the purpose of characteristics comparison, as shown in Figure 3.5. The Maltese cross beam design is constructed similar to the tree branches model, except that the branch separations were removed. Otherwise, both have the same sensing element placements and dimensions.

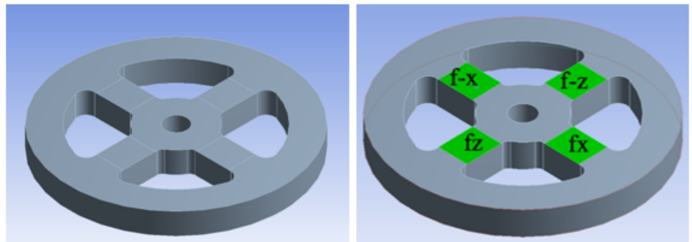

Figure 3.5. Cross 3D force sensor cad model and sensing elements' placements.

3.3 Virtual prototyping

Finite Element Analysis (FEA) was used to characterize these sensors' performances. In this paper, FEA simulations were conducted using ANSYS Workbench R19.2 [96] to investigate and analyze the proposed bio-inspired 3D force sensors for strain and 3D force measurements. The material of the bio-inspired sensors was the structural steel from the ANSYS library [96]. The material had the mechanical properties shown in Table 1.

Table 3.1. Structure steel's mechanical properties from ANSYS library [96].

Density	7850 kg m^{-3}
Poisson's Ratio	0.3
Tensile Yield strength	2.5E+08 Pa
Compressive Yield strength	2.5E+08 Pa
Tensile Ultimate strength	4.6E+08 Pa

The surface splitter tool from the design modular toolbar was used to split surfaces of the sensing elements from the overall sensors' connected areas. This led to both accurate and targeted strain measurements at those areas. An automated meshing was generated for the models and refinements of two were applied at each sensing element's placement for more accurate results, as shown in Figure 3.6. In terms of boundary conditions, the bottom outer rings' surfaces of the spider, the turtle, and the modified turtle were assumed to be fixed supports and the external circumference areas of outer rings were assigned to be fixed in the tree branches and cross designs. Then, two loading scenarios were applied and investigated. Perpendicular (Y-axis) and lateral (X-axis) forces were applied on the bolt hole for each mode. Forces were applied separately and gradually, increasing with five increments up to the maximum force range of 100 N and 60 N for Fy and Fx, respectively. Force was not applied to or analyzed in the Z-axis because all designs are symmetric and the structures were expected to behave similarly to lateral (X-axis) force scenario.

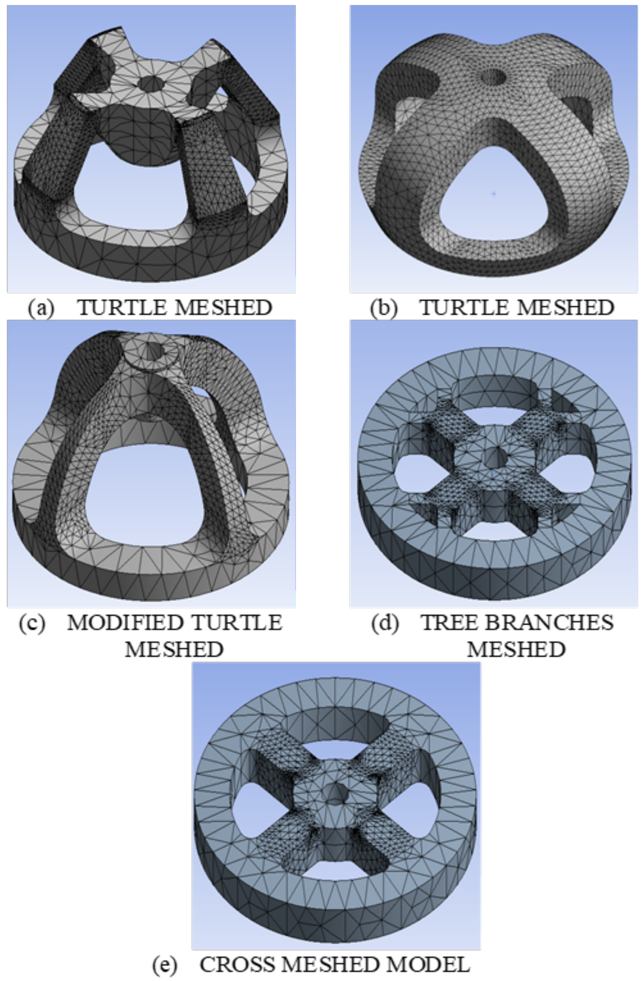

Figure 3.6. Meshed 3D force sensors models.

After the simulation was run and the solution was retrieved, the design was analyzed for structural failure and strain measurements were taken at the sensing elements' placements. The yield strength and equivalent stresses were used to asses the elastic structures' durability and their ability to withstand the applied force's ranges. In terms of strain, a normal elastic strain criterion was used to indicate the expected strain measurements at the sensing placements. Normal elastic strain represents the measured extension or shrinking of imaginary paths along a specific direction of the body's surface [96]. Thus, the strains along specific directions were retrieved based on which directions gave more sensitive and symmetric strain responses. In the spider model, the normal elastic strain orientation was assigned along each of the inclined beam directions. In the turtle model, the normal elastic strain orientation was assigned in the lateral direction. In the modified turtle design, the normal direction of the inner faces was used. Finally, for both the tree branch and cross beam models, the strain orientations were assigned along each of the beam directions. Structure sensitivity was investigated using the average normal elastic strain values recorded along each of these surfaces.

4. STRAIN SENSOR FABRICATION AND EXPERIMENTAL TESTING

4.1 Spray-coated sensor fabrication

The Polyvinylidene Fluoride (PVDF) was chosen as matrix for the nanocomposite sensor because of its high piezoelectricity characteristic. In terms of the nano-conductive filler, the Multi-Walled Carbon Nanotube (MWCNT) was used for the strain sensor. The PVDF powder was purchased from Sigma Aldrich. The average molecular weight (Mw) of the powder was approximately 534,000 mol wt. The MWCNT was purchased from Cheap Tubes. Their outer diameter was 13-18 nm, their length was 1-12 μm, and their purity was $\sim$ 99 wt %. The film was fabricated using solution mixing and spray coating and followed the same procedure as [39]. First, the PVDF was fully dissolved in N-N dimethylformamide (DMF) and stirred on a hot plate for 3 hrs at a temperature of 80 °C. Then, a different concentration of MWCNT was mixed with DMF and the solution was sonicated for 30 min at room temperature until full dispersion of the mixture was achieved. In total, four different sensors were fabricated and the MWCNT, PVDF and DMFs are shown in Table 4.1.

Table 4.1. The MWCNT, PVDF and DMF concentrations for each sensor for spray-coating fabrication process.

		1st solution		2nd solution	
Sensor #	%wt	PVDF(g)	DMF (ml)	MWCNT (g)	DMF (ml)
1	0	2	20	----	----
2	0.1	4	40	0.004	10
3	2	1	10	0.02	50
4	4	0.6	6	0.024	60

The percentage of PVDF to DMF was 0.1 g/mL in the 1st solution, whereas the percentage of the MWCNT to the DMF was 0.0004 g/mL [39]. Then, the two solutions were mixed together at room temperature and stirred for one hour. For random MWCNT dispersion, spray-coating was selected to fabricate the proposed sensors. An air brush was used to manually spray the PVDF/MWCNT sensor located on the glass substrates, as shown in Figure 4.1.

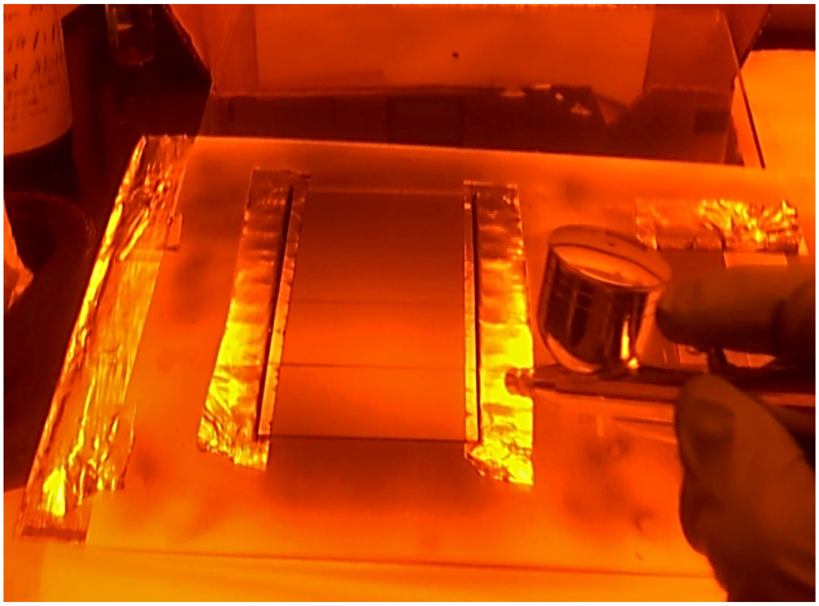

Figure 4.1. Spray-coating process of 4% MWCNT/PVDF during fabrication.

The PVDF/MWCNT solution was poured inside the air brush's color cup and sprayed in a zig-zag path for about 50 rounds. The 4 wt% sensor received 93 rounds. Each spray round traveled from left to right and then from up to down; respectively, until the whole substrate was covered with nanocomposite droplets. Each deposited layer was air dried between rounds. The sprayed films on the substrates were then placed on hot plate at 80 C until all of the solvent is evaporated. Then, they were placed in a sonication container for few minutes to peel the film off the glass substrates. These fabrication processes for the PVDF/MWCNT film sensor using solution mixing and spray-coating are summarized in Figure 4.2.

Afterwards, the films were removed from their substrates and taken out of the sonication container, the nanocomposite films were easily removed out of the substrate by hand, as shown in Figure 4.3. The thicknesses of the fabricated films, each made with a different concentration, were then measured. The films' thicknesses decreased as MWCNT concentration increased even if the number of spray rounds was the same. The more PVDF concentration in the composite, the more film thickness was achieved. The average thickness of the 0 wt

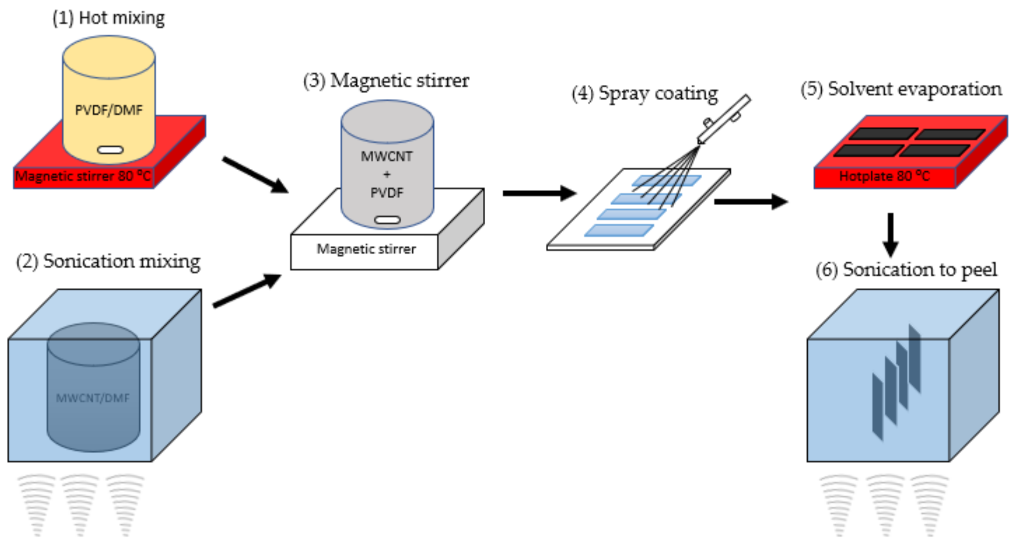

Figure 4.2. Fabrication processes of the PVDF/MWCNT films using spray-coating.

%, 0.1 wt%, 2 wt % and 4% sensors were found to be 27.4 μm, 24.5 μm, 8 μm and 9.5 μm, respectively.

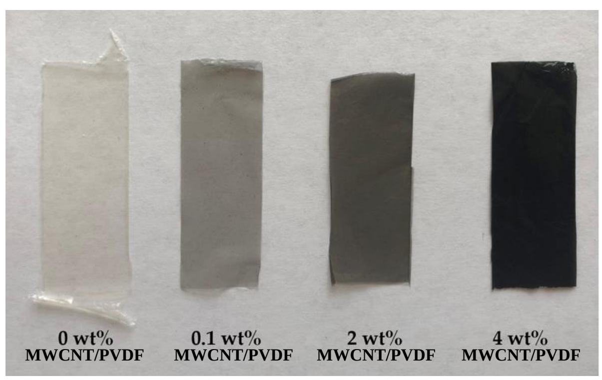

Figure 4.3. The fabricated MWCNT/PVDF films using spray-coating.

For the final experiment and 3D force sensor, the 0.1 wt.% and 2 wt.% MWCNT/PVDF nanocomposites were chosen because of their optimal performance for piezoelectric and piezoresistive measurements, respectively [39]. The same PVDF powder was used for the new films as was used for the previous films. However, new MWCNTs were purchased from Sigma Aldrich. Their outer diameter and length were 7-15 nm, and 0.5-10 μm, respectively. The film was fabricated using the fabrication process discussed in Figure 4.2. The

PVDF/MWCNT solutions were sprayed in a zig-zag pattern for about 144 and 330 rounds for the 0.1 wt.% and 2 wt.% MWCNT/PVDF films, respectively. The average thickness of the 0.1 wt.% and 2 wt.% films were 40 μm and 25 μm, respectively.

4.2 Electrospun sensor fabrication

The fabrication of the proposed MWCNT/PVDF strain film using the electrospinning technique was investigated. Two solution mixing methods were used to achieve the desired fibers, which was a challenging process. The 0.1 and 2 wt.% MWCNT/PVDF nanocomposites were produced using each method. The MWCNT, PVDF, and DMF concentrations and weights are described in Table 4.2. The first solution mixing method used the spray-coating's solution mixing method as discussed in the previous section. The electrospinning method presented in the study [51] was used in the second solution mixing procedure. The PVDF and MWCNT were mixed with the DMFs solutions separately and two solutions were mixed together. Then, 0.5 ml of the MWCNT/DMF solution was added to the PVDF/DMF solution and mixed on a magnetic stirrer at room temperature for 1 hour. Finally, 4 mL of acetone was added to the prepared MWCNT/PVDF solution before performing the electrospinning to enhance the evaporation.

Table 4.2. The MWCNT, PVDF and DMF's concentrations for each sensor for electrospinning fabrication process.

		1st solution		2nd solution			
Sensor	**wt.%**	**PVDF (g)**	**DMF (ml)**	**MWCNT (g)**	**DMF (ml)**	**Acetone (ml)**	**Method**
E1	0.10	3.00	12.00	0.003	13.5	4	1st
E2	2.00	3.00	12.00	0.06	13.5	4	1st
E3	2.15	2.2	6	0.05	10	4	2nd
E4	0.1	2.2	6	0.0022	10	4	2nd

The Electrospinning Device developed by the Integrated Nanosystems Development Institute (INDI), Indiana University–Purdue University Indianapolis was used to produce the MWCNT/PVDF strain film, as shown in Fig. 4.4. The device consisted of a syringe pump, a static copper collector cover by AL foil, and a high-voltage power source. The prepared MWCNT/PVDF solutions were poured into the syringes which were attached later to the syringe pump. On the device, the power supply's wire is connected to the syringe's needle while the ground wire is attached to the static collector from the back. The distance between the syringe needle's tip and the collector, the solution pumping rate, and the applied voltage are the critical parameters for achieving the desire nanofibers through the electrospinning process.

Figure 4.4. Electrospinning fabrication device. (Fabrication performed at the Integrated Nanosystems Development Institute (INDI), Indiana University–Purdue University Indianapolis (IUPUI)).

4.3 3D force fabrication

The structure configuration is a critical parameter that influences the 3D force sensor's performance. Different bio-inspired structures were proposed for the 3D force structure and analyzed for their structural sensitivity and measurement coupling [46]. The tree branches' structural configuration was selected for the 3D force structure for different reasons. The tree branch configuration attained the most negligible coupling between the strain measurement at the sensing placement areas during the X-axis loading test compared to other proposed designs and the cross design. Also, the turtle and tree branches achieved the lowest sensitivity difference of 5E-8 between the normal and lateral direction loading scenarios compared to the other design. However, the turtle design had a lower sensitivity for strains on the X-axis beams under X-direction loading. On the other hand, an average sensitivity difference of 1.67E-7 was obtained by the spider, modified turtle, and cross design. The tree branches design had the highest safety factor for all loading directions and allowed the structure configuration to withstand higher force ranges. In terms of sensor fabrication, a simple two-dimensional fabrication process can be used to fabricate the cross and tree branches design such as a conversion machine, water jet, and laser cutting process. In comparison, other designs might need advanced machine technologies such as Computer Numerical Control (CNC). Flat sensing element placements were presented for the tree branches design and the cross design, facilitating the bonding of the sensing elements to the structures' beams. It can be concluded that the tree branch configuration offered the best combination of safety factors, sensitivity, structure fabrication, sensing placements, and structural integrity as required for a 3D force sensor. As a result, the tree branch design was selected to produce the proposed 3D force sensor. The 3D force's structure was made of aluminum (Al) with a thickness of 1.6 mm and fabricated using laser-cutting technology, as shown in Figure 4.5.

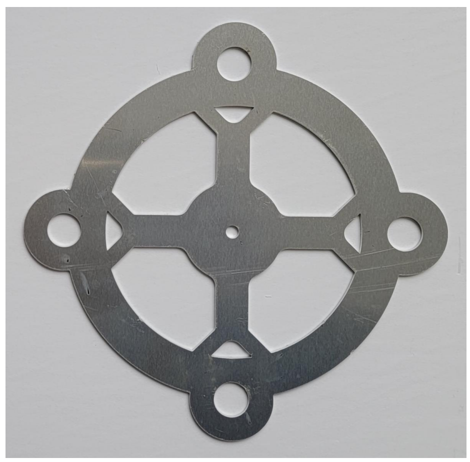

Figure 4.5. The fabricated 3D force's tree branches' structure using laser cutting technology.

The structure consisted of an inner ring, an outer ring, and four connecting beams. The inner and outer rings diameters are 45 mm and 150 mm, respectively. The rings are connected with four beams that allow a sensing element placement area of approximately 20 $\times$ 15 mm^2. Generally, the 3D forces are applied to the center of the structure. A bolt hole with a diameter of 5.5 mm was inserted in the structure's center. For mounting purposes, four bolt holes were open at the end of each beam along the outer ring's circumference. The sprayed 0.1 wt.% and 2 wt.% MWCNT/PVDF films were retrieved to quantify the strain on the 3D force's structure using their piezoelectric and piezoresistive characteristics. The sensing element installment and connections are shown in Figure 4.6.

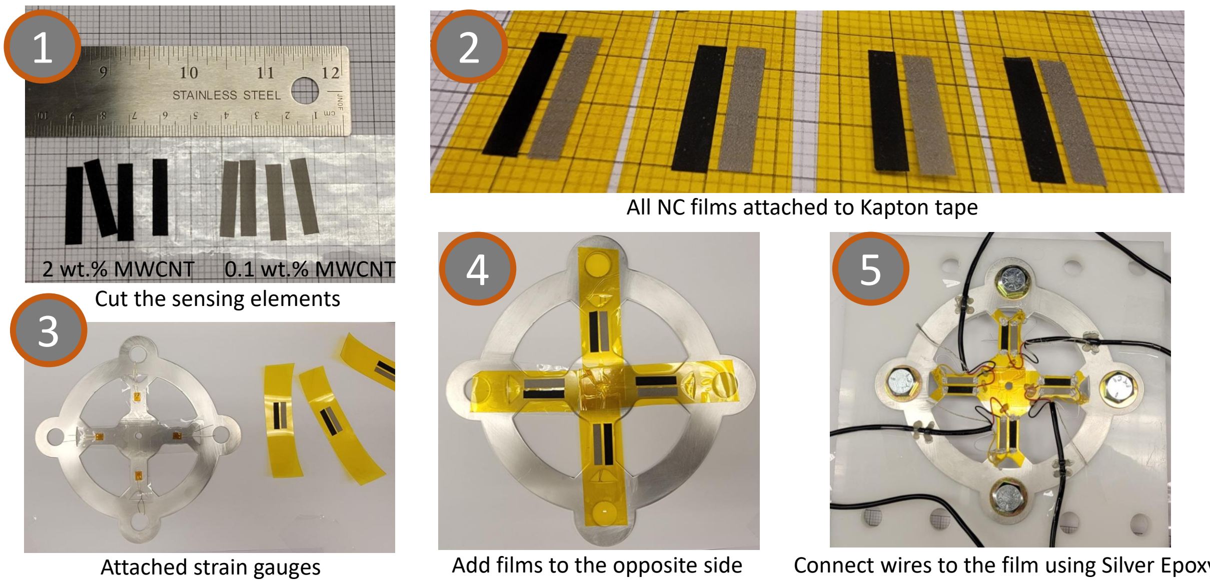

Figure 4.6. The 3D force's sensing elements' attachment and connection process.

First, four films of each concentration were cut down from the same sprayed films. All films had the same dimension of approximately 5 mm × 25 mm. Then, one of each 0.1wt.% and 2wt.% MWCNT/PVDF films were put into in four groups and attached in parallel to a single double-sided Kapton tape using the tape adhesion. On the Kapton tape, both sensing elements were separated by a distance of approximately 2 mm. Next, four commercially available strain gauges were attached to the bottom side of the 3D force sensor in the middle of each beam. The strain gauges were assumed to measure the same strain measured by the NC films, with the same magnitude and opposite phase. Later, the Kapton tapes, including the sensing elements, were attached to the centers of the four beams of the 3D force sensor. Lastly, silver epoxy was used as electrodes for the MWCNT/PVDF films and the electrical wire connections for measuring the strains.

4.4 Uni-axial stretching and electrical poling

To increase the β crystallites and to assist with converting the α phase of the PVDF to the β phase, a sequential mechanical stretching and electric poling process was selected. A film clamping system and heating control chamber with silicone heating pads was proposed for use in an existing universal tensile machine (UTM), as shown in Figure 4.7.

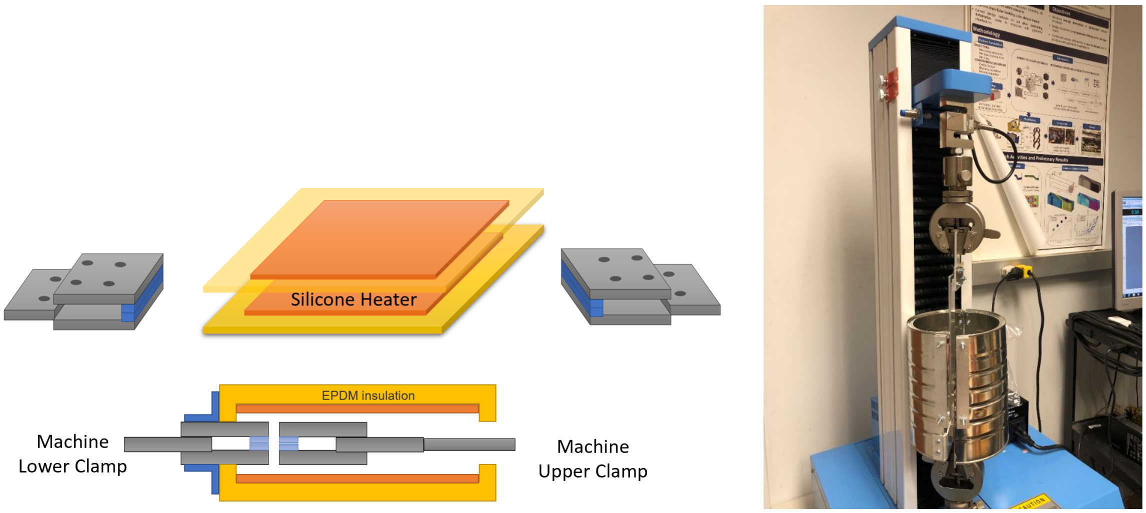

Figure 4.7. Stretching system schematic.

The stretching system consisted of film lower and upper clamps, a heating system, and a thermally insulated chamber.The lower film clamp's beam was connected to the bottom side of the chamber and attached to the lower tensile grip of the UTM. The upper film clamp's beam connected to the upper tensile grip that allowed films to be stretch upward freely. The NC film should be stretched at temperature of $80°C$ because phase transformation is less effective at temperatures higher than $80°C$ [57]. A 10 mm EPDM sheet insulation was then installed inside the chamber. Elongation and speed could be adjusted using the UTM settings. The presence of the β phase in the PVDF increases with stretching the material to about 300% elongation of the original length [97]. In the study [39], even when the applied electric potential was kept the same, a greater presence of the β phase of the film resulted in a thinner film and a subsequently greater elecrtic field during the poling process.

Corona poling and contact poling are two forms of proposed electric poling treatments. The piezoelectric properties of the resulted PVDF film are influenced by stretching ratio, poling time (min), grid voltage, poling field, and poling temperature [56]. As shown in Figure 4.8, the corona poling setup is constructed using four threaded rods with nuts to adjust the height of each part. U-shape Aluminum beams are used to hold up the structure and to from the upper and lower sides. At the top, a stack of corona needles made of Tungsten is attached to a sheet of polyethylene parallel piped to protect the structure from the high voltage potential of the chosen treatment. Next, a stainless steel grid mesh is added to transform the uniform electric field through to lower film, which attached to a copper electrode plate. The corona needle is connected to high voltage of 15 kV. A voltage divider with resistances of 15 and 60 MΩ is used to provide a potential of 3 kV to the grid mesh [39]. The corona setup should be placed on a hot plate during the treatment. Finally, plexiglass is used to contain all harmful plasma generated by the corona treatment.

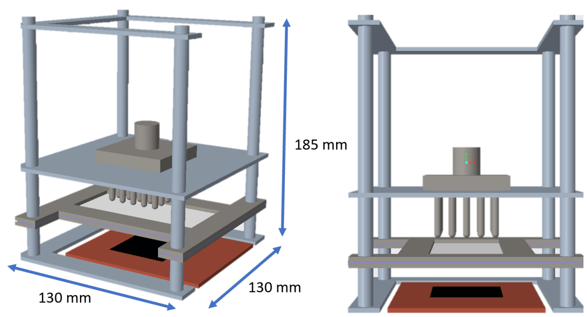

Figure 4.8. Corona poling setup.

The contact poling setup is simpler than the corona poling, as shown in Figure 4.9. First, silver strips are painted on both sides of the sample [61] or conductive tapes may be used as electrodes for better electrical contact. Then, the film is installed between the sample holders, which are normally made of non-conductive material, and then pressure is applied on the sample during the poling process. A maximum potential of 100 V is applied through the electrodes for 3 hours [61].

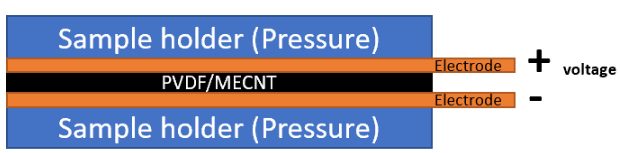

Figure 4.9. Contact poling setup.

Contact poling treatment is associated with arching phenomena which results in an uneven distribution of the electric field through the film and damages the film [39]. On the other hand, corona poling minimizes arching and generates a uniform electric field. Only a few charges will pass through the damage. The remaining charges will facilitate the electric field, that will result in an even poling process [39].

4.5 Sensor characterization

4.5.1 Morphological characterization

The electromechanical characteristics of the PNC's film is affected by the internal formation of the CNT inside the polymer matrix. As a result, the sensor film's characteristics before and after treatment needs to be analyzed using morphological techniques. These techniques are used to investigate the CNTs' alignment and dispersion during the fabrication process.

A Scanning Electron Microscope (SEM) is used to investigate the CNTs' alignment, dispersion and aggregations. The JSM-7800F Schottky Field Emission Scanning Electron Microscope is used at 5 kV, as shown in Figure 4.10. Transmission Electron Microscopy (TEM) was performed for the 4% MWCNT/PVDF at 30 kV using the same device.

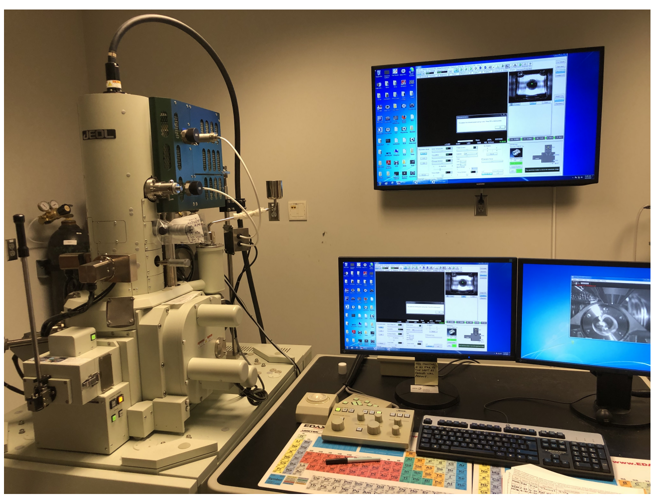

Figure 4.10. SEM device.

Fourier-Transform Infrared Spectroscopy (FTIR) is used to investigate the film polarization before and after treatment and to assist in identifying the amount of β phase improvement.The Nicolet ^{TM} iS^{TM}10 FTIR Spectrometer is used as shown in Figure 4.11. For this paper, the NC films were scanned over frequencies of 500-1700 cm $^{-1}$.

Figure 4.11. FTIR device.

4.6 Experimental setup

The fabricated MWCNT/PVDF sensors' and 3D force sensors' performance were analyzed and tested using different experimental setups. Additionally, the piezoresistive and piezoelectric strain measurements' characteristics were tested using a cantilever vibration beam setup. Finally, the 3D force sensor performance and fusion were conducted using a 3D force vibration setup. The following subsections discusses both methodologies.

4.6.1 Cantilever vibration testing setup

The cantilever vibration beam setup was constructed using B&K vibration exciter Type 4808 and Al beam, as shown in Figure 4.12. The first end of the beam was attached to a fixed end while the other end was connected to the shaker. A 0.1wt.% film and 2wt.% MWCNT/PVDF film and a strain gauge were attached close to the fixed end, where higher strain measurements were expected. Wires were connected to the NC films using silver epoxy, which acted as the sensing elements' electrodes. The beam was excited at 0.5 Hz, 1 Hz, 5 Hz, 10 Hz, 50 Hz, 100 Hz, and 1000 Hz vibration frequencies. The Fast Fourier Transform (FFT) was applied to both measurements' signals using the (signal-to-noise ratio) SNR command in MATLAB to analyze the piezoresistive and piezoelectric strain sensors' characteristics.

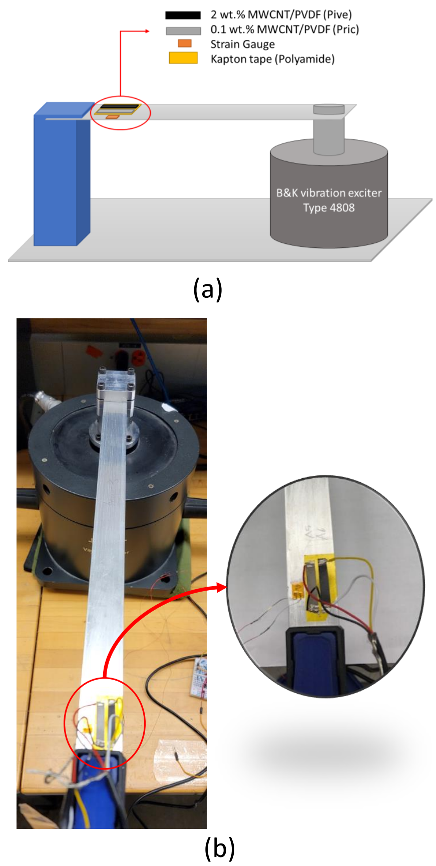

Figure 4.12. The cantilever vibration beam setup (a) setup schematic, and (b) actual experiment setup.

4.6.2 3D force sensor vibration testing setup

The 3D force sensor was tested for X-axis and Z-axis' vibration. For the dynamic loading experiment of the sensor in the Z-direction, a fixture was designed to hold the sensor above the vibration exciter, as shown in Figure 4.13. The 3D Force sensor was then excited at 2 Hz, 5 Hz, 10 Hz, 100 Hz. The fixture was made of a High-Density Polyethylene (HDPE) sheet with a thickness of 12.7 mm and four threaded rods with nuts. The four threaded rods connected the HDPE sheet and the shaker's base to make the fixture more rigid. The 3D force sensor was centered and connected to the shaker using a small threaded rod. In addition, four bolts were used to attach the sensor to the HDPE sheet.

For the X-direction dynamic loading experiment, an extra HDPE sheet was inserted perpendicular to the previous sheet, as shown in Figure 4.14. Four brackets were used to

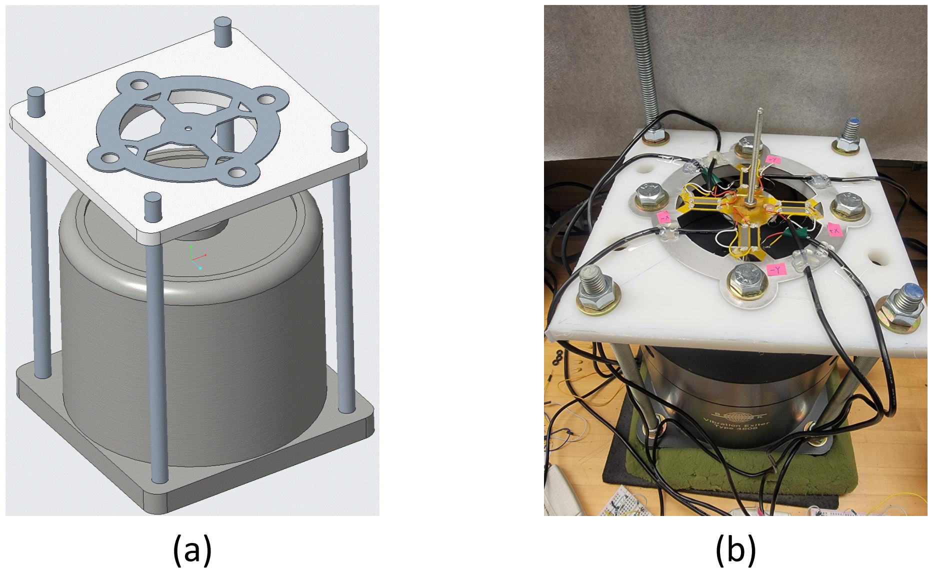

Figure 4.13. The 3D force sensor vibration setup for Z-axis (a) fixture CAD design, and (b) actual 3D force sensor attached to the fixture.

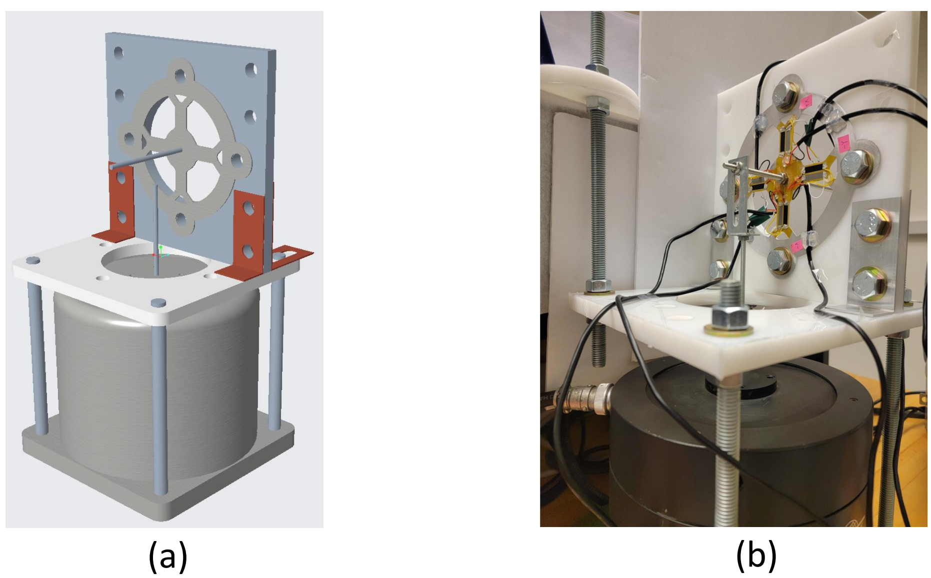

Figure 4.14. The 3D force sensor vibration setup for X-axis (a) fixture CAD design, and (b) actual 3D force sensor attached to the fixture.

hold the HDPE sheets. As a result, the 3D force sensor was perpendicular to the shaker. The 3D force sensor and the shaker were connected using threaded rods and a small bracket.

4.7 Data acquisition and signal conditioning

The MWCNT/PVDF film's resistance change represents the piezoresistive characteristic, while the film's generated charge characterizes the piezoelectric measurement. The Wheatstone bridge was used to magnify the resistance change for the piezoresistive sensing elements by utilizing quarter bridge configuration, as shown in Figure 4.15. The 3D force sensor was tested under different excitation frequencies using the Z-axis and X-axis loading fixtures. At the same time, the piezoresistive sensors, piezoelectric sensors, and strain gauges' measurement were obtained, analyzed, and implemented in the PPF based methods.

The sensing element has an internal variable resistance (R) and capacitance (C). A capacitance C1 was combined with the resistance R3 to achieve a balanced bridge while ensuring that all the bridges' resistances were equivalent. The bridge was then supplied with 2.5 V. The instrumentation amplifier INA333 from Texas Instruments was selected for the piezoresistive, piezoelectric, and reference strain gauge circuits. The INA333 is considered to be a precise and low-power amplifier for high-accuracy application [98]. The amplifiers were powered by 5 V and a reference voltage of 2.5 V was provided using the precision series voltage reference REF5025 from Texas Instruments [99]. The gain-setting resistor (RG) was used to assign the desired measurement amplification gains. For piezoelectric measurements, the 0.1 wt.% MWCNT/PVDF film was connected in parallel with a capacitor C1. A similar circuit has been used in different pressure sensing applications and proven its effectiveness [29]. A quarter Wheatstone bridge was used for the strain gauge measurement similar to the piezoresistive circuit, except no capacitance was inserted on the bridge. This is because of the the approximately purely resistive behavior of strain gauges compared to MWCNT/PVDF sensor. The outputs of the instrumentation amplifiers were sent to LABVIEW using data acquisition cards (DAQs) from National Instruments (NI). The strain gauges were calibrated using the gauge factors. Then, the calibrated strain gauges were used to calibrate both piezoresistive and piezoelectric measurements at each beam individually. Band bass filter was used to filter all measurements of the 3D force sensor. Both the PPF and the EPPF used the calibrated strain measurements from piezoresistive, piezoelectric, and strain gauges during the learning, tuning, and testing of the 3D force sensor fusion.

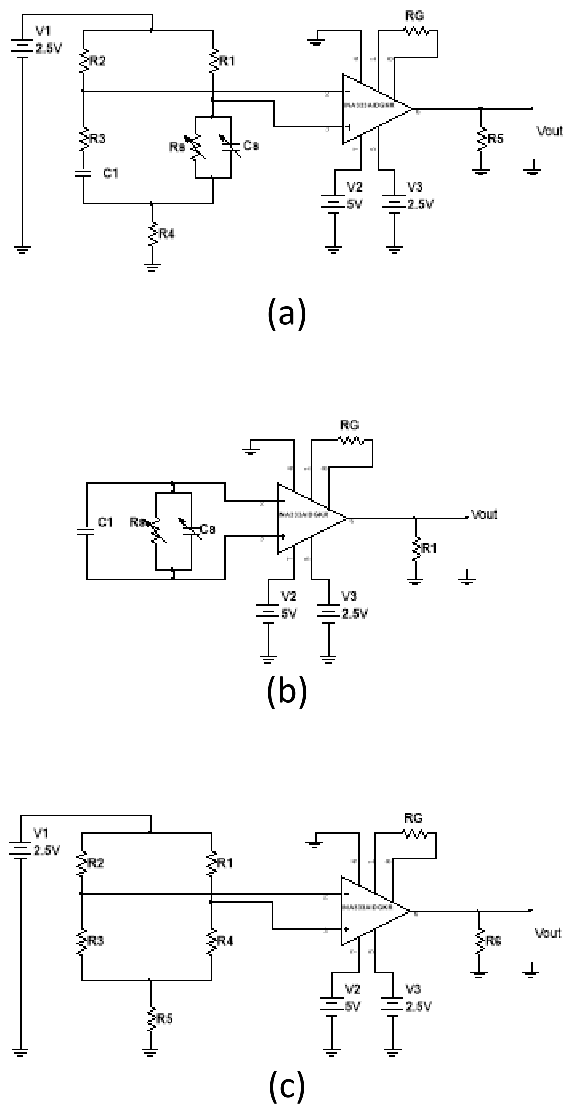

Figure 4.15. Electrical circuits for MWCNT/PVDF's (a) piezoresistive, (b) piezoelectric and (c) reference strain gauge strain sensors.

5. PIEZORESISTIVE/PIEZOELECTRIC FUSION

For the proposed MWCNT/PVDF strain sensor, the PPF method was developed and implemented to combine the measurement data through a fuzzy logic algorithm and generate a wide band strain output, as shown in Figure 5.1. In this method, the piezoresistive and piezoelectric strain data of two adjacent MWCNT/PVDF sensors are used to estimate the final fused strain. While the actual estimated strains ($\varepsilon_{act-est}$) are to be given via Kalman Filter (KF) or the equivalent circuit-based models, actual strains were used here to demonstrate the effectiveness of the proposed method. The piezoresistive and piezoelectric measurement errors (e_{Pive} and e_{Pric}) are calculated by subtracting the estimated strain and piezoresistive and piezoelectric strain data, respectively.

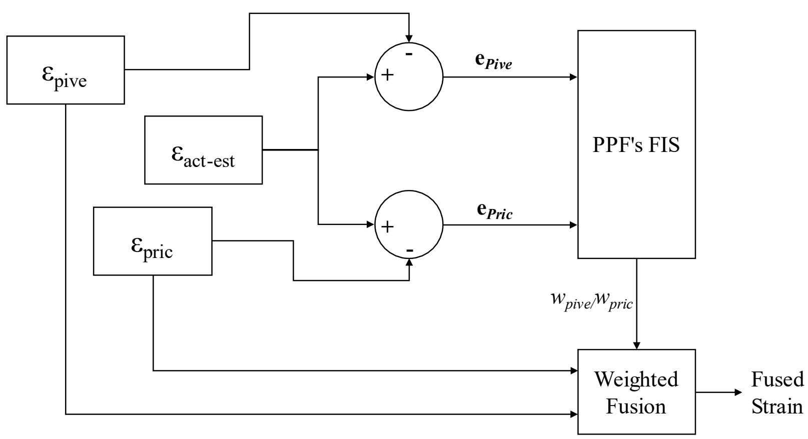

Figure 5.1. Schematic of the Piezoresistive/Piezoelectric Fusion (PPF) method.

The error measurements were normalized using the Min-Max scaling. The normalized error signals are then utilized by the Fuzzy Inference System (FIS) to define the contribution of each signal to the fused strain output as follows:

$$\varepsilon_f(k) = w_{Pive}(K)\varepsilon_{Pive}(k) + w_{Pric}(K)\varepsilon_{Pric}(k) \tag{5.1}$$

where in the final signal (ε_f), w_{Pive} and w_{Pric} are the associated weight with the piezoresistive signal ε_{Pive} and piezoelectric signal ε_{Pric}; respectively. The final fused strain will attempt to match the actual strain (ε_{act}) using the developed FISs. Equation 5.1 has two unknown weights which would lead to an infinite number of solutions for the weights. The dependent weight solutions are shown in Equations 5.2 and 5.3:

$$w_{Pive} = \frac{\varepsilon_{act} - w_{Pric} \times \varepsilon_{Pric}}{\varepsilon_{Pric}} = \frac{\varepsilon_{act} - w_{Pric} \times (\varepsilon_{act} - \mathrm{e}_{Pric})}{\varepsilon_{act} - \mathrm{e}_{Pive}} \tag{5.2}$$

$$w_{Pric} = \frac{\varepsilon_{act} - w_{Pive} \times \varepsilon_{Pive}}{\varepsilon_{Pive}} = \frac{\varepsilon_{act} - w_{Pive} \times (\varepsilon_{act} - \mathrm{e}_{Pive})}{\varepsilon_{act} - \mathrm{e}_{Pric}} \tag{5.3}$$

To simplify the fusion equation's solution, one sensor was assigned a constant weight while the other sensor's weight was computed using either Equation 5.2 or 5.3, based on both sensors' accuracy at that frequency. At low frequency strain measurements, w_{Pive} was assigned a full weight of one and w_{Pric} was computed using Equation 5.3 due to the high accuracy and sensitivity of the piezoresistive characteristic. On the other hand, the piezoelectric sensor was accurate at high frequencies. Therefore, a full weight of one was given to w_{Pric} and the w_{Pive} was computed using 5.2. However, because of the harmonic measurements and zero strain axis crossing, the w_{Pive} and w_{Pric} values would approach infinity at these points. To mitigate this, ε_{act}, ε_{Pive} and ε_{Pric} were shifted in amplitude by a constant number c, which is a real positive number and assumed to be greater than twice the maximum strain measurement's range. Then, w_{Pric} and w_{Pive} were computed using the shifted data using Equations 5.2 and 5.3. The final fused strain measurement is given by 5.4:

$$\varepsilon_f = w_{Pive} \times (\varepsilon_{Pive} + c) + w_{Pric} \times (\varepsilon_{Pric} + c) - c \tag{5.4}$$

In the fuzzy logic part of the fusion, the fusing process undergoes four consecutive stages to compute these weights. These stages are the fuzzification, rule generation, the FIS process, and defuzzification. Fuzzification is the process of converting a crisp quantitative input to a fuzzy value that is conducted based on knowledge information [100]. The normalized measurement errors are fuzzified to span a range of values between zero and one using represented membership functions. The membership functions are labeled by linguistic variables that represent the input or output information. The error membership functions are fuzzified to span values of [0, 1] which map the normalized inputs' errors. Either the piezoresistive weighting (w_{Pive}) or piezoelectric weighting (w_{Pric}) was selected to be FIS's output variables, based on the characteristic sensitivity at the specific operation frequency. The second part of the fustion process, Fuzzy Inference Systems (FIS), is the process of taking the fuzzy system's inputs into outputs, based on the predetermined fuzzy rules. These rules are based on either actual experimental data or are knowledge-based. Defuzzification is the process of converting fuzzy value to a real quantity in contrast with the fuzzification process [100]. In the PPF method, the combined fuzzy output sets are defuzzified to achieve the wpive or wpric using the Center of Area (COA) method, which is recognized as the center of gravity, for Mamdani FIS Type-1 [101], [102]. A weighted average is then used to evaluate the output at Type-1 Sugeno FIS [103].

In the study [39], the PVDF/MWNT strain sensor has been attached to a 28 cm aluminum cantilever beam. The PNC sensor was attached at distance of 5 cm from the fixed end and a vibration exciter was attached to the free end of the beam. The beam's width and thickness were 25 mm and 3 mm, respectively. Copper electrodes were attached to both ends of the film and double-sided tape was used to adhere the strain sensor to the cantilever. A commercial metal foil strain gauge was used for performance verification and comparison. A voltage divider was used to retrieve the piezoresistive measurement while a charge amplifier was used for the piezoelectric characteristic. This study retrieved the MWCNT/PVDF piezoresistive and piezoelectric strain measurements in contrast to the reference strain gauge measurements, as shown in Figure 5.2. The experimental data from Park et al. [41] study were used to generate and validate the PPF method using Fuzzy Logic and Global Optimization Toolboxes in MATLAB [104].

The actual strain was assumed to be equal to the strain gauge (reference) measurement data [39] in this study. Furthermore, the piezoresistive and piezoelectric data were used to develop and validate the proposed PPF method, using the same data at the three different frequencies. In this work, several approaches were used to achieve the PPF's FISs, which fuse both piezoresistive and piezoelectric characteristics. The FIS system contains several input and output membership functions and a set of rules that defines the input/output relationship. Designing and tuning such a FIS for the PPF method is a challenging process.

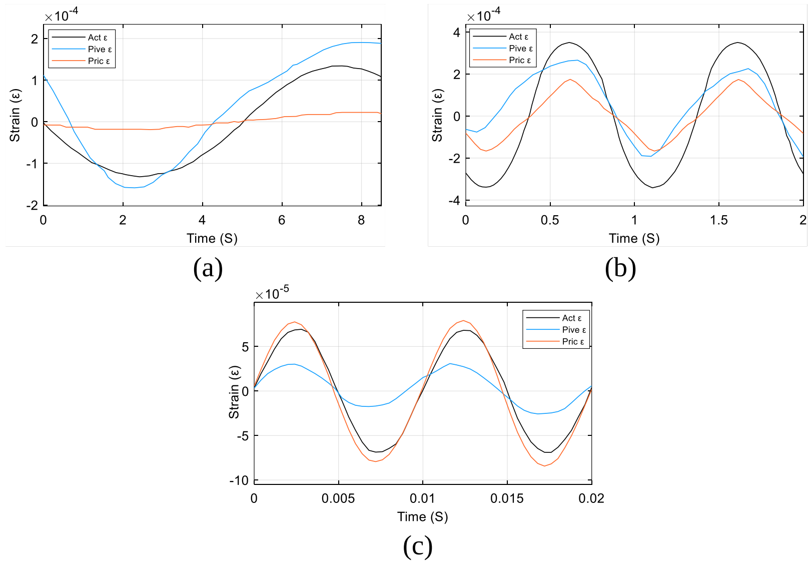

Figure 5.2. Strain measurements at a cantilever using piezoresistive sensor, piezoelectric sensor, and metal foil strain gauge (actual) under forced vibration of: (a) 0.1 Hz, (b) 1 Hz, and (c) 100 Hz [39].

As a result, data-driven based approaches were used for tuning the FIS's parameters and learning the rules using the shifted data and weight values from Equation 5.2 or 5.3 . These approaches were the optimization method, data clustering, and combination of type-2 FIS and data clustering. These approaches are discussed in the following subsections. The constant value (c) of 0.001 was used for the fusion at 0.1 Hz while a constant value of one was used at 1 Hz and 100 Hz frequencies.

5.1 Optimization-based PPF

The global optimization methods were implemented to develop the PPF's FIS at 0.1 Hz, 1 Hz, and 100 Hz strain measurements scenarios. The tuning process of the fuzzy system was conducted in two stages to improve the FIS's performance [105]. The first step was learning the rules of the fuzzy system using the given data. The second step was tuning the parameters of both input and output membership functions (MFs), using the rules which were learned in the previous phase. As shown in Figure 5.3, the optimization method adjusted the FIS's parameters given the cost of each solution which is the root mean square error (RMSE) in this study. The FIS retrieves the input training data and its output is compared with the output training data to produce the solution's cost [105].

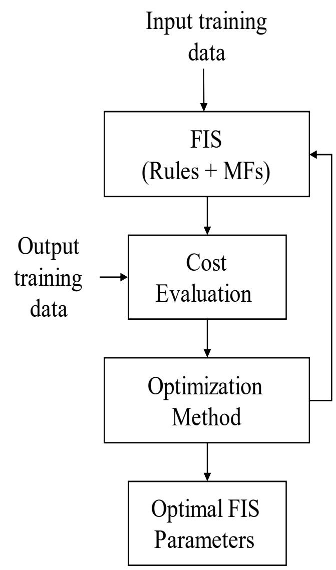

Figure 5.3. PPF's FIS tuning using data-driven optimization methods schematic.

At frequencies of 0.1 Hz and 1 Hz, which are considered low frequency strain measurements in this work, $w_{P\text{ive}}$ was assigned a full weight of one and w_{Pric} was computed using Equation 5.3 because of the highly accurate sensitivity of the piezoresistive characteristic. By contrast, the piezoelectric sensor takes more accurate strain measurements at higher frequencies, such as 100 Hz, as shown in Figure 5.2c. Therefore, a full weight of one was given to w_{Pric} and $w_{P\text{ive}}$ was computed using Equation 5.2. The normalized errors for both sensors and w_{Pric} were the inputs and output of the FISs, respectively, at the low frequencies. However, the $w_{P\text{ive}}$ was considered the output for the FIS because of the high accuracy of the piezoresistive sensor at higher frequencies. The input and output data were divided into two data groups, training data and validation data. These groups used data with odd and even indexed sample numbers, respectively. However, only training data were used to generate the PPF's FIS at different operation frequencies. Validation data were used to tune and verify the performance of the FIS. The particle swarm optimization method was utilized in the learning the rules phase under fixed input/output MFs' parameters using 20 iterations. The pattern search optimization method was used for tuning the FIS's parameters phase including the rules and the input/output MFs with 60 iterations. Three Gaussian MFs were chosen for the FIS's inputs and outputs at 0.1 Hz and 100 Hz operation frequencies, while three MFs were used at 1 Hz.

5.2 Data clustering-based PPF

Data clustering is considered the foundation for many grouping and system modeling algorithms [106]. Clustering is the process of identifying and classifying a large set of data into common groups. These groups form a compact model that captures the system model's performance accurately. The Fuzzy Logic Toolbox^{TM} in MATLAB was used to identify the input/output data's clusters using strain measurement data at 0.1 Hz, 1 Hz, and 100 Hz frequencies. Two clustering approaches were used to develop the proposed PPF's FISs: fuzzy c-means (FCM) clustering and subtractive clustering. They are discussed in the following subsections.

5.2.1 Fuzzy C-Means (FCM) clustering

FCM clustering was presented by Jim Bezdek in 1981 [107]. In this technique, multi-dimensional data points fall into a group with a certain degree of belongingness which is controlled by a membership grade. In this study, the FCM command function in MATLAB was used to perform the FCM clustering for the input/output data sets and generate the PPF's FISs [108]. The FCM clustering process begins with initially random locations of the cluster's centers and a membership grade specified for each of the data points. Each cluster's center is iteratively adjusted for data input/output set by updating the data point's cluster and membership grade. The distance between each data point and the cluster's center is the objective function which is to be minimized. The distance is weighted by the membership grade. The maximum number of iterations and the minimum improvement between two consecutive iterations in the objective function's values were 100 and 1Ö10^{-5}, respectively. The number of clusters was chosen to be six for the PPF at 0.1 Hz and 100 Hz, while five clusters were used at 1 Hz data set classification. As a result, the number of input/outputs MFs and rules in the FIS equals the number of clusters at each frequency. The generated clusters' centers and membership grades were used by the command line function genfis in MATLAB to develop a Mamdani-type FIS.

5.2.2 Subtractive clustering

Subtractive clustering was introduced by Stephen Chiu in 1994 and significantly reduced the current computational costs [109]. For any given input/output set of data, subtractive clustering is considered a quick way to estimate clusters' numbers and centers' locations. In this study, the subclust command function in MATLAB was used to perform the subtractive clustering for the data input/output sets and generate the PPF's FISs [110]. The subtractive cluster deals with each data point as a possible cluster center. Depending on the distribution density of the input/output data points, the possibility of being a cluster center is calculated. The data point with highest likelihood of being a center is selected to be the first cluster's center, whereas other number data points are removed based on the cluster influence range of the input/output clusters' centers. Then, the algorithm selects the following data point with the highest likelihood of being a cluster's center. The latter two steps are repeated until all data points fall inside the cluster influence range. In this study, a cluster influence range of one was used to produce the PPF's FISs at the three strain measurement frequencies. The generated clusters' centers were produced by the command line function genfis in MATLAB to develop a Sugeno-type FIS. One rule was generated for each cluster, and one MF for input/output variables was produced for every cluster similar to the FCM clustering.

5.2.3 Type-2 Fuzzy Inference System (FIS)-based PPF

Previous PPF methods used the traditional type-1 MF, which has a unique membership value and utilizes a linguistic set to model the degree of membership [111]. However, Type-1 MF does not include the model uncertainty in the membership's degree. On the other hand, Type-2 MF does have range of values assigned for the degree of membership. These values range from the Upper Membership Function (UMF) to the Lower Membership Function (LMF); the range in between is called the Footprint of Uncertainty (FOU). For the proposed

PPF method, the Type-2 MF was utilized because of model uncertainty that could arise during the KF model design for both piezoresistive and piezoelectric strain sensors.

Subtractive clustering was used in the input/output data set classification processes with a cluster influence range of one. In addition, the command line function genfis in MATLAB was used to develop a Sugeno-Type-1 FIS. The generated Type-1 FISs were converted to Type-2 FISs using the convertToType2 command line function [112]. The UMF of the generated type-2 FIS's parameters matched the MF of the Type-1 FIS. The produced Type-2 FIS utilizes default properties of the Karnik-Mendel (KM) reduction method to evaluate the output crisp value by finding the centroid of the Type-2 fuzzy set [112], [113].

5.3 The PPF method testing and validation model

A Simulink model was constructed to validate the PPF method using the data in the study [39]. The model follows the schematic of the PPF method in Figure 5.4 and calculates the final fused strain measurement using Equation 5.4. The errors of both the piezoresistive and piezoelectric sensors were computed and normalized. The normalized errors were fed to the fuzzy logic controller block which utilized the developed PPF's FISs for the frequencies 0.1 Hz, 1 Hz, and 100 Hz. The generated weight of $w_{P\text{ive}}$ and $w_{P\text{ric}}$ implemented in Equation 5.4 beside the piezoresistive and piezoelectric strain measurements were used to evaluate the final fused strain measurements.

The final fused strain measurement was analyzed and investigated for its Root Mean Square Error (RMSE) with respect to the actual strain measurement. Additionally, it was compared with the optimal linear smoother-based fusion technique discussed in a study by Park et al. [39]. For the subtractive clustering based PPF, the generated weights were plotted for each frequency's scenario to evaluate the PPF method for sensitivity and performance. The proposed PPF method fused both characteristics smoothly, taking advantage of all available strain measurement data, and produced a sensitive wide band PVDF/MWNT strain sensor.

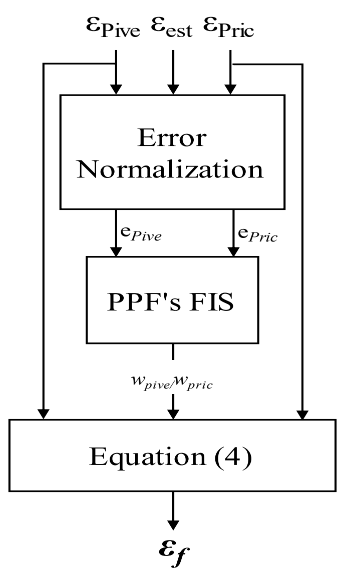

Figure 5.4. PPF's FIS testing and validating Simulink model's schematic.

6. DIRECT PIEZORESISTIVE/PIEZOELECTRIC FUSION

6.1 The direct PPF method

The direct PPF method was proposed to combine the piezoresistive and piezoelectric measurements of the MWCNT/PVDF strain sensors using a fuzzy logic-based methodology, as shown in Figure 6.1. The piezoresistive and piezoelectric measurements are used by the DPPF's FIS as input variables for the DPPF's FIS. Compared to the original PPF method in the previous section, the direct PPF method used the actual piezoresistive and piezoelectric measurements instead of their estimated errors.

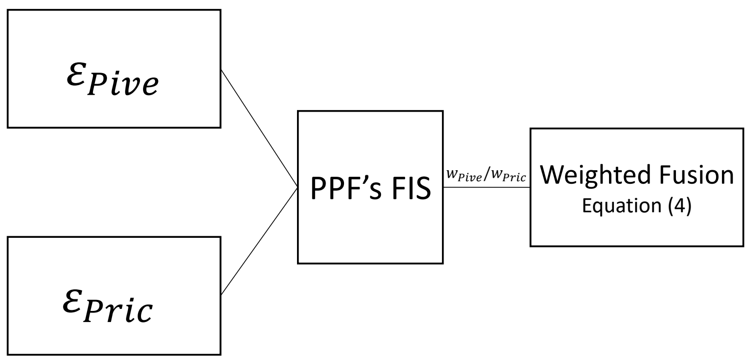

Figure 6.1. Schematic of the direct Piezoresistive/Piezoelectric Fusion (DPPF) method.

The FIS determines the piezoresistive weight (w_{Pive}) or piezoelectric weight (w_{Pric}) based on both the measurements and the FIS's structure and configuration. The final fused strain signal (ε_f) was calculated using Equation 5.1.The piezoresistive strain (ε_{Pive}) and piezoelectric strain (ε_{Pric}) contribution to the final fused strain measurement are determined by the assigned weights, which are w_{Pive} and w_{Pric}, respectively. The weights span the values from zero to one depending on the sensitivity of the piezoresistive and piezoelectric measurement at that frequency. This equation has an infinite amount of solutions due to the presence of the two unknown weighting factors in a single fusion equation. Consequently, one of sensors was assigned a total weight of one while the other sensor's weight was estimated using Equations 5.2 or 5.3 .

At low frequencies, the piezoresistive strain sensor has a higher accuracy and is more sensitive to strain measurements. On the other hand, piezoelectric sensors outperform the piezoresistive sensors when taking high-frequency strain measurements. Thus, a weight of one was assigned to the piezoresistive sensor at low frequency, while the w_{Pric} was calculated using Equation 5.3. Conversely, the piezoelectric sensor was given a whole weight of one, while the w_{Pive} was calculated using Equation 5.2. During the data preparation for the DPPF's FIS, all measurements, including the reference strain gauge measurements, were shifted by a positive constant number c to avoid getting infinity weights in the Equations 5.2 and 5.3 caused by the harmonic strain measurement and zero-crossing at no strain conditions. The shifted data were used to calculate both weights and the final fused strain was estimated using the Equation 5.4.

In the direct PPF, to assign either the piezoresistive or piezoelectric weight, the DPPF's FIS goes through three phases. These phases are the fuzzification, rule generation and FIS process, and defuzzification. First, both measurements are mapped to a range of values from the minimum to the maximum strain values using Membership Functions (MFs) representation. The MFs are described using linguistic variables implying the input's or output's characteristics. In the DPPF method, either the piezoresistive or piezoelectric's weight is selected as the FIS's output depending on the operation frequency and strain sensitivity for each measurement characteristic. The Fuzzy Inference System (FIS) converts given fuzzy inputs into outputs depending on a preassigned set of rules [114]. Then, the fuzzy output values are transferred to actual values in the defuzzification phase [114]. In the DPPF method, the intermixed output is defuzzied to produce the desired piezoresistive or piezoelectric's weights. The Center of Area (COA) method and a weighted average method are used to perform the defuzzification prosses for Mamdani and Sugeno FIS, respectively [101]–[103].

Constructing and tuning the FIS given input/output data is a complex process in the system that contains multiple input/output MFs and rules. Using the error-based PPF, several data-driven approaches were utilized to produce the DPPF's FIS using Fuzzy Logic and Global Optimization Toolboxes in MATLAB [104]. The method is based on the normalized input errors for both measurements. The reference strain gauge measurements were assumed to be the actual strain values. The subtractive clustering-based PPF systems have achieved very low RMSE compared to the optimization and Fuzzy C-means (FCM) clustering methods. As a result, the subtractive clustering technique was used to generate and tune the FIS's parameters and assign the rule set for the direct PPF's performance. All measurement data and reference strain gauges were shifted by a constant number of one at all operating frequencies. This methodology resulted in a single FIS for each operation and limited the fusion to a single operating frequency.

6.2 The Extended Piezoresistive/Piezoelectric Fusion (EPPF) method

As discussed in the previous section, the direct PPF method utilizes the piezoresistive and piezoelectric's measurements to perform the fusion. The fusion is performed at a certain frequency using both measurements and a single FIS that would result in a complex DPPF's structure in the case of the strain measurement at a range of operation frequencies. To address this issue, the EPPF method was introduced to minimize the number of FISs and reduce the direct PPF method's complications, as shown in Figure 6.2.

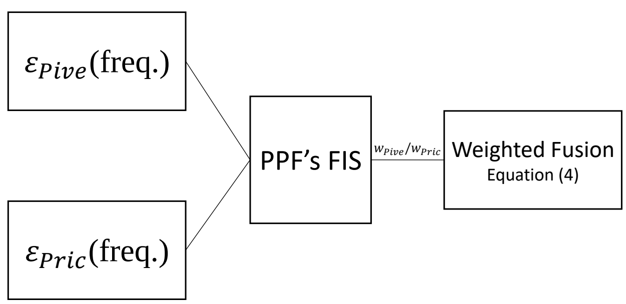

Figure 6.2. Schematic of the Extended Piezoresistive/Piezoelectric Fusion (EPPF) method.

In the EPPF method, the measurements of the piezoresistive strain (ε_{Pive}) and piezoelectric strain (ε_{Pric}) taken at different frequencies were cascaded. The cascaded signals data was used to generate and tune the EPPF's FIS, rules, input, and output MFs. In this way, the PPF method's generation approach and the fusion equation were used to produce the EPPF method. In comparison to the DPPF, the EPPF fuses both measurements at a span of frequencies using a single FIS.

7. PIEZORESISTIVE/PIEZOELECTRIC MODELING

7.1 Piezoresistive modeling

An equivalent circuit modeling apporach was used to mimic the behavior of both the piezoresistive and piezoelectric sensors and to produce similar measurements given the actual input strain. Generally, the signal of piezoresistive strain measurement was processed through the Wheatstone bridge, the differential amplifier, and the low pass filter [104]. A similar model, constructed for the piezoresistive PVDF/MWCNT sensor, was constructed using Simscape Electrical Library in Matlab, as shown in Figure 7.1. This model was used to simulate the performance of the piezoresistive sensor under excitation frequencies of 0.1 Hz, 1 Hz, 100 Hz, and 1000 Hz. The strain gauge data from [61] was used as the actual strain signal fed to the models and the model output was then compared with the piezoresistive measurement in the literature.

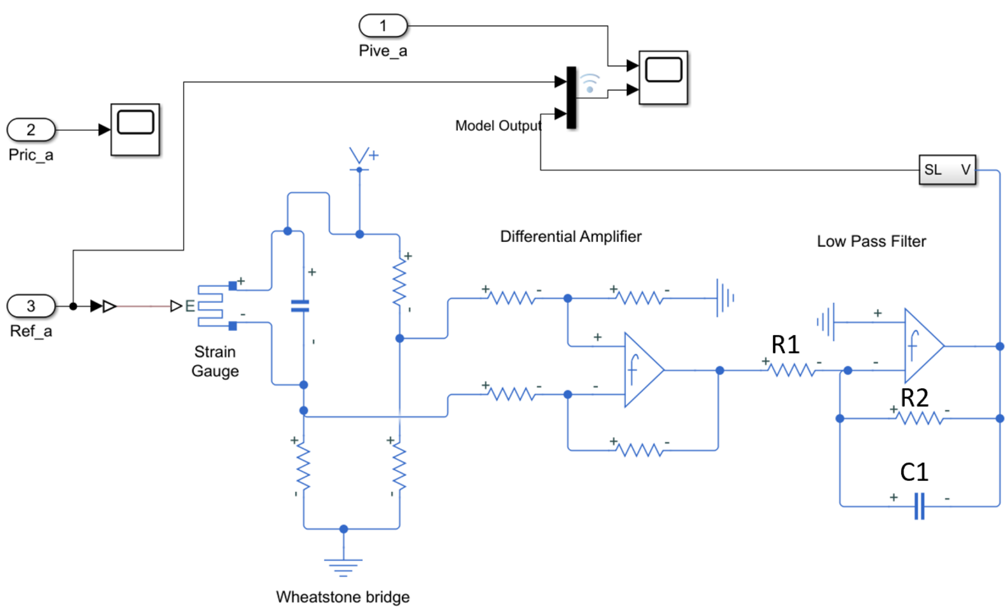

Figure 7.1. Piezoresistive model in Matlab Simulink

In the model, an in-parallel R-C circuit is used to represent the sensing element and the resistance is replaced with strain gauge element from the Simscape Electrical Library. The initial strain and gauge factor (GF) of the sensing element can be adjusted for the strain gauge element. The GF for compress-molding PVDF/MWCNT was found 2.62 [39]. Both spray coating and compress molding fabrication generates a random distribution for the CNT inside the matrix. The sensing element's resistance and capacitance were chosen to be 23.47 kΩ, and 0.74 nF from an after-poling sensor EIS analysis [61]. The rest of the Wheatstone bridge's resistances match the same resistance value of the selected sensing element for better signal amplification. A calibration factor was implemented to convert the final output volt signal into a piezoresistive strain measurement. The op-amps with gains of 1000 were used in the piezoresistive circuit model. The Wheatstone bridge's elements values during the operating frequencies were kept constant. However, the low pass parameters and calibration factors are fitted and analyzed to match the desired piezoresistive signal.

7.2 Piezoelectric modeling

Piezoelectric sensors use charge amplifiers which convert the high impedance charge into output voltage [115]. Given the actual strain ε [39], piezoelectric coefficient d_{31}, sensor length I_c and width b_c, the sensor's modulus Y_c and the sensor's capacitance C_p, the output of the film can be calculated using Equation 7.1 [115]:

$$V_c = \frac{d_{31} Y_c I_c b_c}{C_p} \varepsilon \tag{7.1}$$

This equation was used to simulate the resultant voltage caused by the applied strain measured by the PVDF/MWCNT film. The piezoelectric coefficient of the PVDF is d_{31} of 24 Pc/N [116]. In this model, the piezoelectric coefficient of the PVDF/MWCNT is assumed to be the same as PVDF because the PVDF matrix is dominant at the piezoelectric measurement. The sensor area is assumed to be 1 $\times$2 cm^2. The sensor capacitance is C_p simulated as 0.74 nF [61]. As shown in Figure 7.2, the sensing element output is connected with the connection's resistance and capacitance which are assumed to be 0.001 Ω and 1 μF, respectively. Then, the output is fed into the Charge Amplifiers, followed by a calibration factor. This model is used to simulate the performance of the piezoelectric sensor under the four excitation frequencies. In this simulation, the strain gauge data from [61] is used as the actual strain signal fed to the models and the model output is then compared with

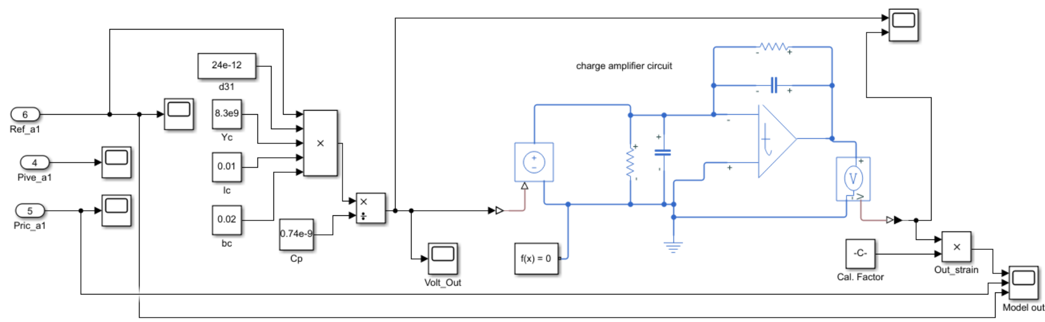

Figure 7.2. Piezoelectric model in Matlab Simulink

the piezoelectric measurement in the literature. The op-amp gain is 400 for all excitation frequencies. The calibration factor is then fitted and analyzed to match the piezoelectric signal under the four different excitation frequencies.

7.3 Actual strain estimation using nonlinear modeling

Several researchers have reported the nonlinearity in the CNT-PNC's piezoresistive and piezoelectric characteristics. The current-voltage (I-V) curve was used to assess the composite nonlinearity performance. Ounaies et al. [117] investigated the nonlinear performance of the single-walled carbon nanotube (SWCNT)/polyimide composites. The tunneling effect was responsible for the nonlinear behavior. Similarly, nonlinearity was observed for the 0.35 wt.% SWCNT/polydimethylsiloxane composite and faded at the 5wt.% composite [118]. For a similar composite, the I-V curve of a 0.2 wt.% CNT/epoxy composite was nonlinear and linear at a high concentration of the CNT [119]. The CNT/epoxy composite tunneling resistance at low CNT content and strain level higher than 0.2 % resulted in a nonlinear piezoresistive's performance [73]. In terms of a CNT/polymer's piezoelectricity, an electrospun PVDF nanofibers mat with no CNTs had achieved a linear voltage-weight relationship [120]. However, nonlinearity was apparent at the 0.3 wt.% CNTs composite. Vinogradov et al. [121] investigated the PVDF's dynamic response and reported the accelerated creep performance due to the cyclic loading at stress levels below the viscoelastic linearity limit. In these ways, researchers have remarked on the nonlinear piezoresistive and piezoelectric's performance of the CNT-PNCs.

Hammerstein-Wiener models have been used to estimate the actual strain given the input piezoresistive measurement at a low frequency or piezoelectric measurement at higher frequencies. The System Identification Toolbox in MATLAB has been used to construct the Hammerstein-Wiener models. The Hammerstein-Wiener model is used as a black-box model because it does not include the physical perceptiveness of the internal processes [122]. As shown in Figure 7.3, the dynamic systems are represented by a discrete linear block and one or two nonlinear memoryless static blocks [122].

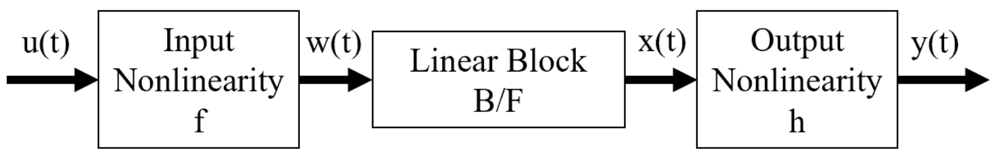

Figure 7.3. Hammerstein-Wiener model's block diagram.

The Hammerstein-Wiener (HW) model has been used for modeling different sensors and actuators to simulate the nonlinear effect either in input or output of a linear system [122]. Despite being one model, this model comes in three structure configurations, including the the Hammerstein model, the Wiener model, and the linear model. It is called the Hammerstein model if there is no output nonlinearity h block and it is named the Wiener model if it contains only the linear block and output nonlinearity h block. The nonlinear Hammerstein-Wiener (nlhw) becomes a linear transfer function if both input and output nonlinearities are removed. For a SISO system, the nlhw models are configured using the number of zeros and poles, input and output nonlinearity estimators, and input delay. In this work, several input/output nonlinearity configurations have been utilized from the system identification toolbox, such as a sigmoid network, a piecewise linear function, and a unit gain (no configuration assigned) [122].

A nonlinear function $y = F(x, \theta)$, where F is a piecewise-linear (affine) function of x, could be represented by a piecewise-linear nonlinearity estimator object [123]. The input (x) and output (y) are scalar and θ is the factor that contains the breakpoints and their values. This particular nonlinear function contained n breakpoints and linearly interpolated between these breakpoints [123]. On the other hand, a sigmoid network function is realized by the sigmoid network object and is used as a nonlinear mapping function to estimate the nonlinear Hammerstein-Weiner models [124]. The mapping function used an offset, a nonlinear function, and a linear weight to estimate the output. The nonlinear function includes sigmoid unit functions, which perform on the weighted sum of inputs [124]. To map m inputs $x(t) = [x(t_1), \cdots, x(t_m)]^T$ to a scalar output y(t), the following mathematical equation is used [124]:

$$y(t) = y_0 + (X(t) - \overline{X})^T PL + S(X(t)) \tag{7.2}$$

where X(t) is m $\times$ 1 vector of inputs with mean $\overline{X}$, and y_0 is a scalar output. Also, $P_{m\times p}$ and $L_{p\times 1}$ are the projection matrix and vector of weights, respectively. The sum of dilated and translated sigmoid functions is represented by the S(X). For the DPPF and EPPF methods, the nlhw models were used to estimate the actual strain from either piezoresistive or piezoelectric sensors. The DPPF and EPPF's performances were compared with the actual strain measurement and nlhw models.

8. RESULT AND DISCUSSION

8.1 Morphological characterization results

8.1.1 Spray-coated MWCNT/PVDF samples

The Scanning Electron Microscope (SEM) images were retrieved for the MWCNT/PVDF films with different concentrations, as shown in Figure 8.1. For the films with lower concentrations of 0 wt% and 0.1 wt%, the specimens have relatively smooth surfaces and signs of aggregation due to the low concentration of CNT. Limited aggregation also appears at the specimens with 2 wt% as the CNTs concentration increases. At the film with 4 wt% CNT, aggregation appears more obviously through the surface, but some areas are limited.

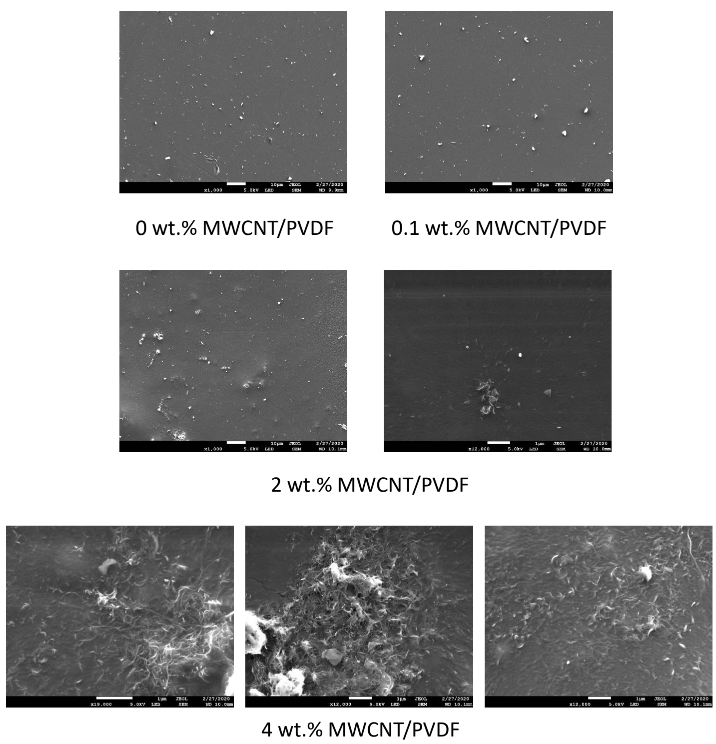

Figure 8.1. SEM micrographs of spray-coated sensor result.

The TEM micrographs were captured only for the 4 wt% films because of their small thickness compared to the other specimens, as shown in Figure 8.2. Two specimens with average thicknesses of 4 μm and 9 μm were fabricated for 4 wt% MWCNT/PVDF film with 95 rounds of spray. For the 9 μm specimen, on the micrographs, the CNTs appear in dark black while the PVDF looks light gray. The dispersion of CNTs is not uniformly distributed and there are aggregation spots through the specimens. The resulted surface appearance is affected by the fabrication methodology, which is the spray coating.. The micrograph picture of the thin film was retrieved by zooming in further, which was not close enough to compare with previous specimen. However, zooming in on the thinner film shows that both films have a relatively similar CNT distribution in their matrices.

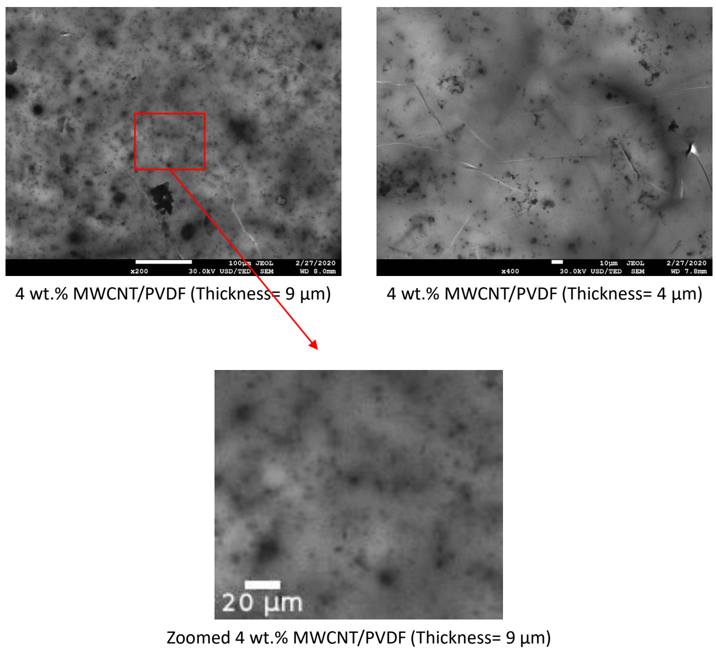

Figure 8.2. TEM micrographs results.

The absorbance charts of the fabricated films were generated using the FTIR device, as shown in Figure 8.3. Two samples were scanned for each concentration, except the thin and thick 4% films were only tested once. On the 0 % and 0.1 % films, the α phase peaks are present at at 765 cm^{-1}, 795 cm^{-1}, and 975 cm^{-1} bands. Also, intense β phase peaks were recorded at 840 cm^{-1}. A small peak is present at the band 1279 cm^{-1} for only one of the plane PVDFs because of the higher thickness of other films. The β phase peaks are high because of the very low CNT concentration. On the other hand, the β phase peaks' intensities at the 2 % and 4 % shrank significantly. In addition, no signs for the α phase are present. These values were used to evaluate the amount of α and β phases before and after mechanical stretching and electric poling treatments.

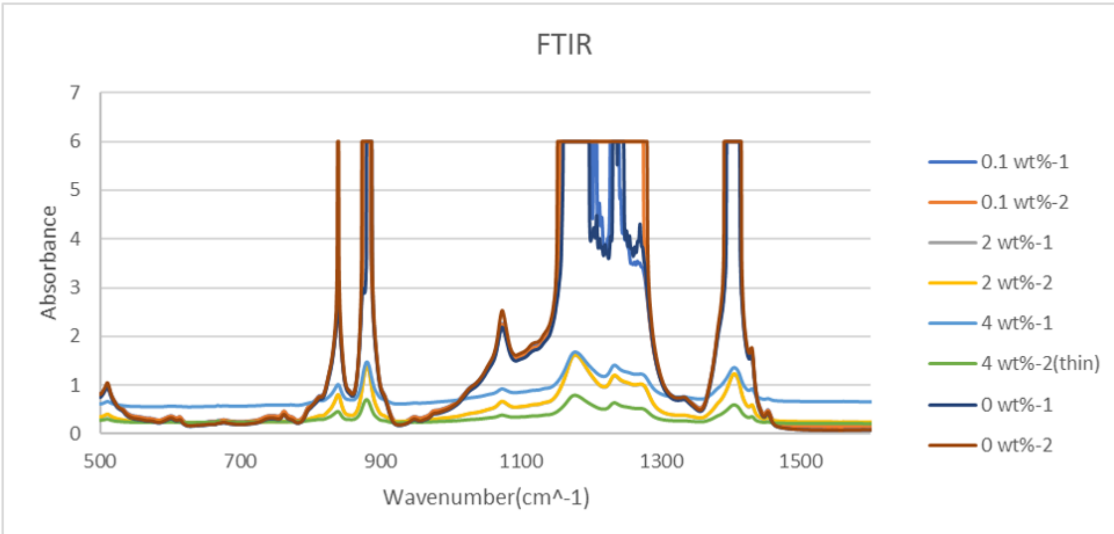

Figure 8.3. FTIR result.

8.1.2 Electrospun MWCNT/PVDF samples

In the electrospun samples, parameters were optimized and adjusted to achieve the desired nanofibers of MWCNT/PVDF nanocomposites. Several trails were utilized with different parameter settings, as shown in Table 8.1.

Table 8.1. The electrospinning's parameters used to generate the MWCNT/PVDF sensor.

Try	Sensor	CNT%	Distance (cm)	Rate (ml/hr)	Volt (Kv)
1	E1	0.1 %	12	0.15	10.8
2	E2	2 %	12	0.15	10.8
3	E2	2 %	12	2	10.8
4	E3	2.15 %	12	0.15	10.8
5	E4	0.1 %	12	0.15	10.8
6	E4	0.1 %	12	0.15	15
7	E4	0.1 %	12	0.15	20

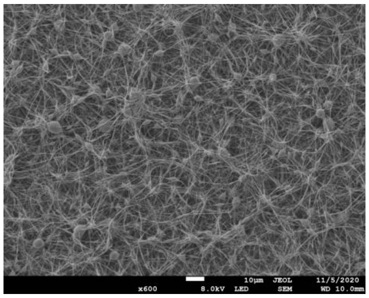

Try 1. E1 Sensor, 0.1 wt.% MWCNT/PVDF

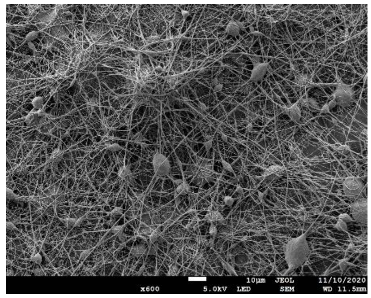

Try 2. E2 Sensor, 2 wt.% MWCNT/PVDF

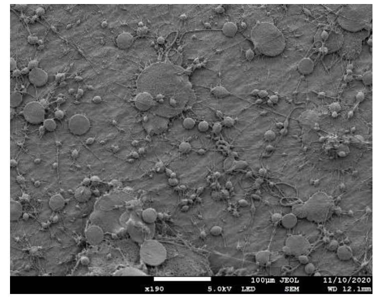

Try 3. E2 Sensor, 2 wt.% MWCNT/PVDF

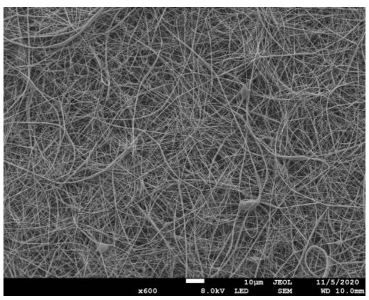

Try 4. E3 Sensor, 2.15 wt.% MWCNT/PVDF

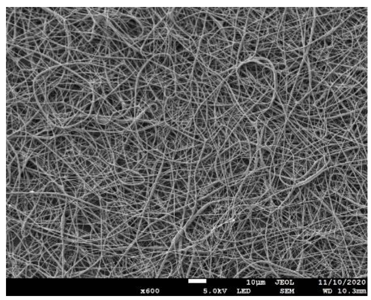

Try 5. E4 Sensor, 0.1 wt.% MWCNT/PVDF

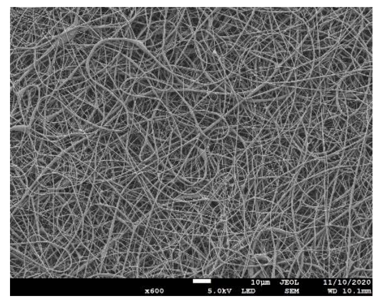

Try 6. E4 Sensor, 0.1 wt.% MWCNT/PVDF

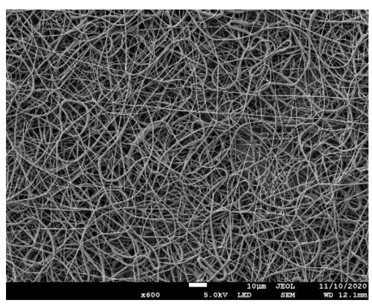

Try 7. E4 Sensor, 0.1 wt.% MWCNT/PVDF

Figure 8.4. SEM micrographs of electrospun sensor result.

The four predeveloped solutions for the electrospinning method were deposited on thin sheets of aluminum foil. A constant distance of 12 cm was adjusted between the syringe needle's tip and the collector during all trials. The pumping rate was fixed at 0.15 ml/hr except on the third trial in order to observe how the pumping rate influenced the nanofiber production.

The SEM was used to investigate the nanofibers' formation, dispersion, and aggregations, as shown in Fig. 8.4. Nanofibers were created for sensor E4 with 0.1 wt. % MWCNT/PVDF nanocomposites using the second method, based on the study [51] solution mixing process, at different applied voltages. The first method, based on spray-coating solution mixing ratios, attained higher aggregation at the first try. Elevated aggregations and poor dispersion were presented in the SEM image in the E2 sensor with 2wt.% CNT deposition. In addition, when the pumping rate was increased from 0.15 ml/hr to 2 ml/hr, spraying was observed instead of fiber generation.

8.2 Piezoresistive/Piezoelectric Fusion (PPF) results

The MWCNT/PVDF film has both piezoelectric and piezoresistive characteristics which are strongly dependent on the dynamic loading frequency. The PPF method was analyzed at excitation frequencies of 0.1 Hz, 1 Hz, and 100 Hz. For strain measurements under small operational frequencies (0.1 Hz and 1 Hz), a full weight of one was given to the piezoresistive sensor due to the high sensitivity measurement. In addition, the PPF method predicted the piezoelectric's weight in the final fused signal based on the developed FISs. By contrast, the whole piezoelectric strain measurements were used due to their high accuracy and sensitivity at a high frequency (100 Hz). The FISs were used to estimate the piezoresistive weight, which was applied in the fusion process using 5.4. The performance of the resulting FISs, which were based on an optimization method, data clustering, and fuzzy Type-2 FIS, were validated and analyzed using the fused strain's accuracy and the strain's RMSE. The generated subtractive clustering-based PPF's weights were retrieved and investigated at the three frequencies. The following sections discuss the results of proposed PPF's performance.

8.2.1 Optimization-based PPF results

The optimization based PPF's FISs were tested for the operation frequencies of 0.1 Hz, 1 Hz, and 100 Hz, as shown in Fig.8.5. For the input/output labels, the piezoresistive and piezoelectric sensors' variables were numbered as first and second, respectively. Each FIS had two input and output MFs except the FIS for the 1 Hz operation frequency which had three MFs. The input variables' values spanned values between zero and one because the measurements' errors for both sensors were normalized. The range of the MF's outputs were

Table 8.2. Optimization based PPF'S FISs rules.

Frequency	FIS's rules
0.1 Hz	1. If (en1 is mf2) and (en2 is mf2) then (w2 is mf2) (1) 2. If (en1 is mf1) and (en2 is mf1) then (w2 is mf1) (1) 3. If (en1 is mf1) and (en2 is mf2) then (w2 is mf1) (1) 4. If (en1 is mf2) and (en2 is mf1) then (w2 is mf2) (1) 5. If (en1 is mf2) then (w2 is mf2) (1)
1 Hz	1. If (en1 is mf1) then (w2 is mf3) (1) 2. If (en1 is mf2) and (en2 is mf1) then (w2 is mf2) (1) 3. If (en2 is mf3) then (w2 is mf1) (1) 4. If (en2 is mf2) then (w2 is mf1) (1) 5. If (en1 is mf3) and (en2 is mf3) then (w2 is mf1) (1) 6. If (en1 is mf1) and (en2 is mf3) then (w2 is mf1) (1) 7. If (en1 is mf1) and (en2 is mf1) then (w2 is mf3) (1) 8. If (en1 is mf2) and (en2 is mf2) then (w2 is mf2) (1) 9. If (en1 is mf2) and (en2 is mf3) then (w2 is mf1) (1) 10. If (en1 is mf3) and (en2 is mf2) then (w2 is mf1) (1) 11. If (en1 is mf2) then (w2 is mf2) (1)
100 Hz	1. If (en1 is mf1) and (en2 is mf2) then (w1 is mf1) (1) 2. If (en2 is mf2) then (w1 is mf1) (1) 3. If (en2 is mf1) then (w1 is mf2) (1) 4. If (en1 is mf2) and (en2 is mf1) then (w1 is mf2) (1) 5. If (en1 is mf2) and (en2 is mf2) then (w1 is mf1) (1)

determined based on the maximum and minimum values of the estimated piezoresistive and piezoelectric's weights from either 5.2 or 5.3 at the three operation frequencies.

The developed FIS conveyed the fuzzy system's inputs into the desired outputs based on the predetermined fuzzy rules. The final set of rules were generated from the tuning stage using the tunefis command line function, as shown in Table 8.2. These rules governed the relationship between the FIS's inputs and produced the desired outputs. The number of generated rules for the three operation frequencies 0.1 Hz, 1 Hz, 100 Hz were 5, 11, and 5, respectively. A higher number of rules was associated with the 1 Hz FIS due to the higher number of MFs need to relate to each other and the desired weight. To connect between the antecedent's conditions, the AND (&) operator, which stands for the minimum value among these conditions' values, was used. The MIN implication method was implemented to achieve the proposed FISs. In addition, the MAX method of aggregation was utilized to combine the rule's outputs into a solo fuzzy set. The Center of Area (COA) method was used to defuzzify the combined fuzzy's output sets in order to generate the appropriate sensors' weights.

The estimated fused strain was generated and compared with the actual piezoresistive and piezoelectric strain sensors at the three different frequencies, as shown in Fig.8.6. A

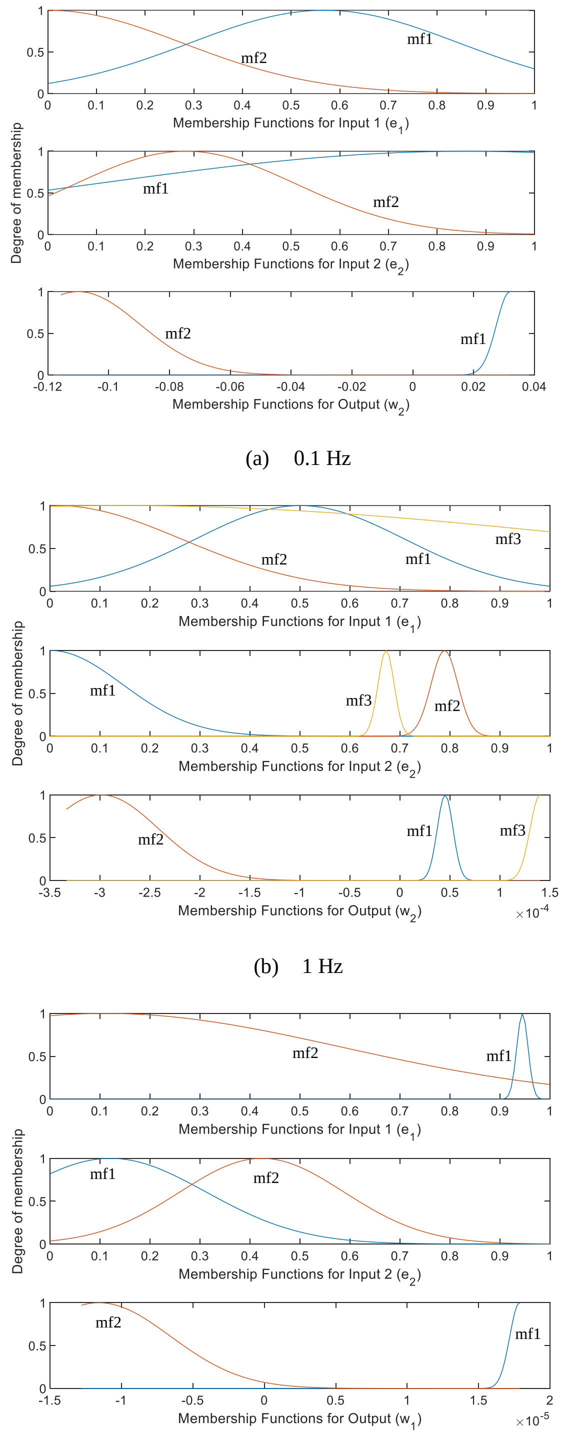

(a) 0.1 Hz

(b) 1 Hz

(c) 100 Hz

Figure 8.5. Input and output MFs of optimization based PPF's FISs.

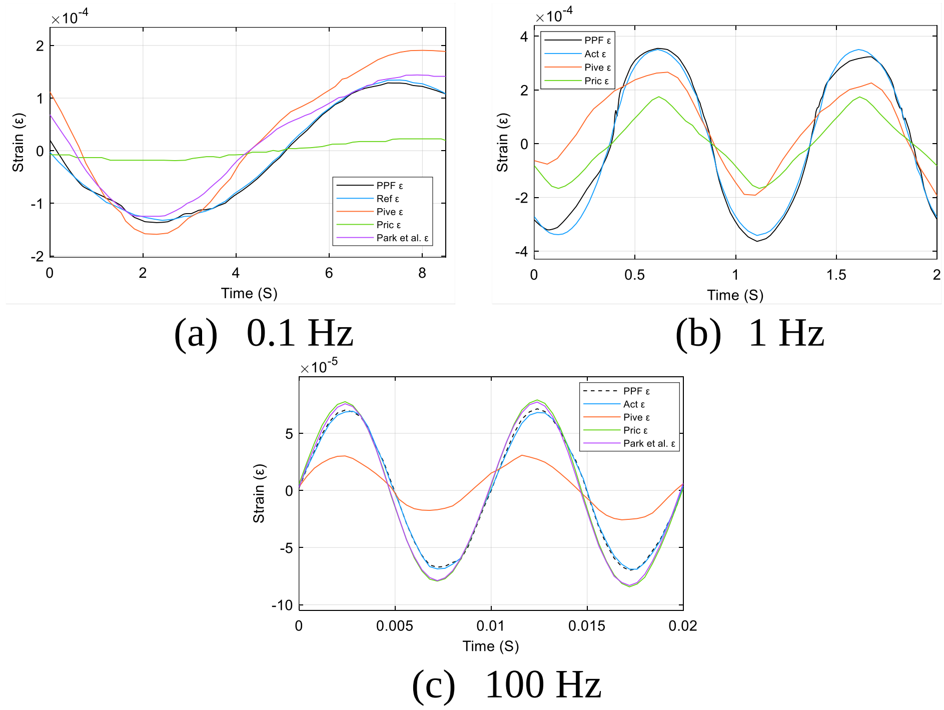

Figure 8.6. Optimization based PPF FISs' fused output strain.

good agreement between the actual strain measurements and the PPF's fused strains was observed by using the optimization based FISs. This accuracy was achieved with comparably low iteration numbers; 20 iterations were used for learning the FIS's rules and 60 iterations were used for tuning the FIS's parameters.

8.2.2 Clustering-based PPF results

The fusion FISs based on the two data clustering methods were retrieved and verified at the operating frequencies of 0.1 Hz, 1 Hz, and 100 Hz. The clustering methods used were the FCM and subtractive clustering.In the following subsections, the FISs were analyzed for their input/output MFs' parameters and generated rules and fused strain's RMSE.

Fuzzy C-Means Clustering (FCM) Results

As shown in Fig.8.7, the MFs for input/output variables were generated to fuse the piezoresistive and piezoelectric NC sensors at the three-operation frequency. The ranges of both input and output variables matched those used in the optimization-based FIS. A minimum number of MFs, which could achieve a good and accurately fused strain, was manually defined. As shown in 8.7a and 8.7c, the number of input/output MFs have been chosen to be six MFs at 0.1 Hz and 100 Hz, while a number of 20 MFs was chosen for the strain measurements fusion at 100 Hz, as shown in 8.7b. The piezoresistive and piezoelectric characteristic had relatively higher error values at the 100 Hz frequency compared to other operation frequencies as shown in 8.7b. However, minimizing the MFs would reduce the output computation complexity and decrease the fused strain accuracy. The MFs were labeled by variables representing the cluster number for input/output variables' values.

A set of rules was produced for the FCM clustering based FIS using the genfis command line function, as shown in Table 8.3. The FISs for 0.1 Hz and 100 Hz frequencies shared six generated rules, while 20 rules were assigned for the 1 Hz fusion frequency, the number of MFs and rules associated with each frequency were equal. The AND (&) operator was used to connect the antecedent's conditions and the MIN implication method was implemented to achieve the proposed FISs. The MAX method of aggregation was utilized to combine the rule's outputs into a solo fuzzy set. To generate the appropriate sensor weights for the proposed Mamdani FIS, the COA was used to defuzzify the combined fuzzy's output in a way similar to the optimization-based FISs.

Table 8.3. FCM clustering based PPF'S FISS rules.

Frequency	FIS's rules
0.1 Hz and 100 Hz	1. If (in1 is in1cluster1) and (in2 is in2cluster1) then (out1 is out1cluster1) (1) 2. If (in1 is in1cluster2) and (in2 is in2cluster2) then (out1 is out1cluster2) (1) 3. If (in1 is in1cluster3) and (in2 is in2cluster3) then (out1 is out1cluster3) (1) 4. If (in1 is in1cluster4) and (in2 is in2cluster4) then (out1 is out1cluster4) (1) 5. If (in1 is in1cluster5) and (in2 is in2cluster5) then (out1 is out1cluster5) (1) 6. If (in1 is in1cluster6) and (in2 is in2cluster6) then (out1 is out1cluster6) (1)
1 Hz	1. If (in1 is in1cluster1) and (in2 is in2cluster1) then (out1 is out1cluster1) (1) 2. If (in1 is in1cluster2) and (in2 is in2cluster2) then (out1 is out1cluster2) (1) *n*. If (in1 is in1cluster *n*) and (in2 is in2cluster *n*) then (out1 is out1cluster *n*) (1) … Where *n*= 1, 2,…, 20 … 20. If (in1 is in1cluster20) and (in2 is in2cluster20) then (out1 is out1cluster20) (1)

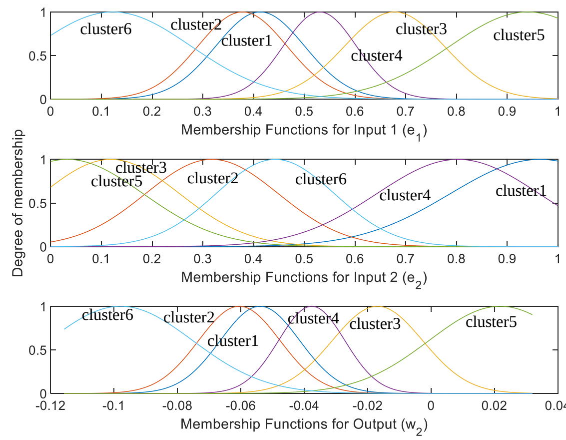

(a) 0.1 Hz

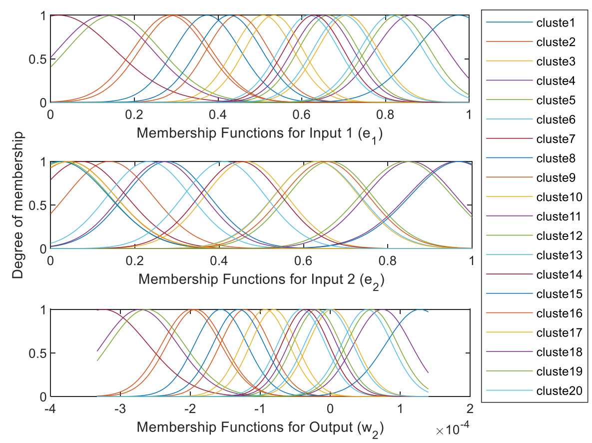

(b) 1 Hz

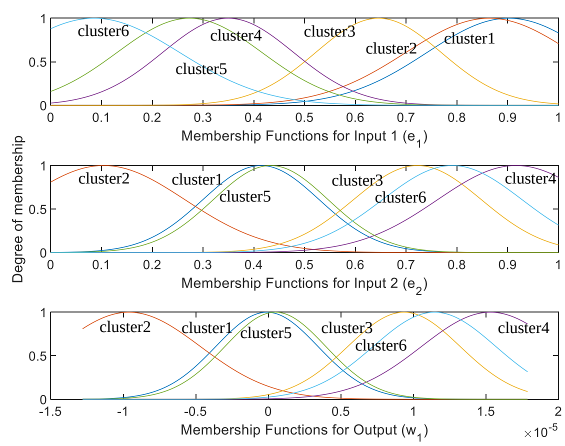

(c) 100 Hz

Figure 8.7. Input and output MFs of FCM based PPF's FISs.

Fig. 8.8, illustrates the evaluation of the the performance of the generated FISs using the FCM clustering. Compared to the piezoresistive and piezoelectric strain sensors at the three different frequencies, the PPF method agreed closely with the actual strain, which was measured using the strain gauge. The FIS at 1 Hz mismatched three out of four peaks, but was still more accurate than the piezoresistive and piezoelectric sensors. The fusion at 100 Hz achieved a higher accuracy than two other FCM based FISs. Compared to the Park et al. fusion at 0.1 Hz and 100 Hz, the PPF's fused strains matched well with the actual strain, despite the higher number of input/output MFs.

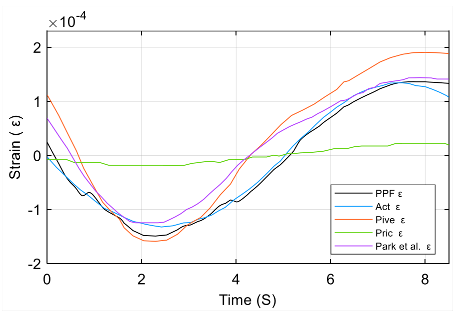

(a) 0.1 Hz

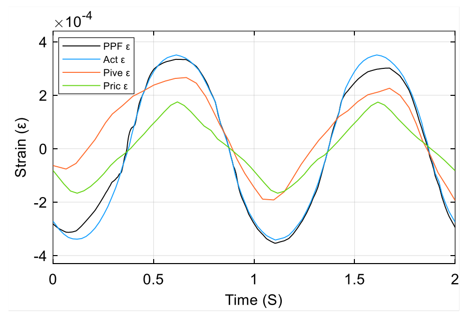

(b) 1 Hz

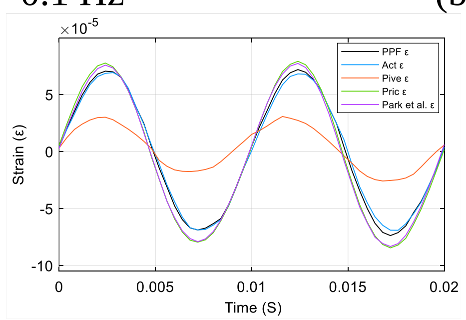

(c) 100 Hz

Figure 8.8. FCM clustering based PPF FISs' fused output strain.

Subtractive clustering results

The subtractive clustering was the second approach used that was based on data classification. A Sugeno-based FIS, which utilizes singleton output MFs, was used to develop the PPF's FIS [125]. The output MFs may be in the form of either a constant or linear function in terms of the input values. The linear function based Sugeno FIS was used for this study.

The final output weight was computed using the i rule output level z_{i} and rule firing strength w_{i}. The Z_{i} is function in two inputs values e_1 and e_2 and three constant values a_{i}, b_{i}, and c_{i}, which were generated using genfis command line function in MATLAB, as shown in 8.1:

$$z_{\mathrm{i}} = a_{\mathrm{i}}x + b_{\mathrm{i}}y + c_{\mathrm{i}} \tag{8.1}$$

In the equation above, w_{i} is evaluated from the rule antecedent using the AND method for both input errors. The weighted average was used to compute final output weigh for N number of rules. The equation is as follows 8.2:

$$\text{Final Output Weight} = \frac{\sum_{\mathrm{i}=1}^{N} w_{\mathrm{i}} z_{\mathrm{i}}}{\sum_{\mathrm{i}=1}^{N} w_{\mathrm{i}}} \tag{8.2}$$

The FISs input's MFs and output linear equations' constants were generated and tuned using the subtractive clustering technique, as shown in Fig. 8.9. Two MFs were assigned for the normalized error inputs at the three strain measurement frequencies. Each MF represented a cluster of a range of input values. The Z_{i} functions associated the piezoelectric output weight at 0.1 Hz and 1 Hz frequencies and the piezoresistive output weight at 100 Hz. The constant values of each FIS were retrieved to evaluate the final output weights using the weighting average.

A set of FISs' rules was generated from the subtractive clustering process using the genfis command line function, as shown in Table 8.4. Similar to the MFs' number, three rules were produced for the FISs at the 0.1 Hz and 100 Hz frequencies. The AND (&) operator was used to combine the fuzzified input's values for each rule. To generate the appropriate sensors' weights, the weighting average was used. The AND operator works as a product of fuzzified input values [103]. The subtractive clustering method generates an equal number of input/output MFs and rules. The differences between the developed subtractive-based FISs were the input MFs' parameters and the output linear function constants' values.

The subtractive-based PPF fusion method was tested and compared with the NC piezoresistive and piezoelectric strain signals, as shown in Fig. 8.10. A close agreement between the actual strain measurements and the PPF's fused strain measurements was achieved by comparing the subtractive clustering based FISs to the Park et al. fusions at 0.1 Hz and

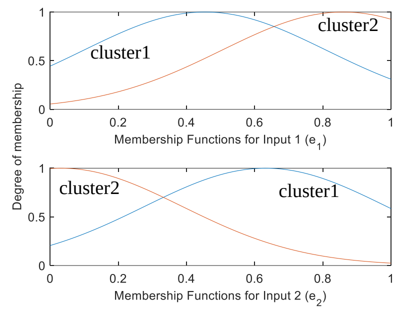

Input

out1cluster1

$$\begin{bmatrix} a_i \\ b_i \\ c_i \end{bmatrix} = \begin{bmatrix} 0.1436 \\ 0.003462 \\ -0.1167 \end{bmatrix}$$

out1cluster2

$$\begin{bmatrix} a_i \\ b_i \\ c_i \end{bmatrix} = \begin{bmatrix} 0.1463 \\ 0.003375 \\ -0.1156 \end{bmatrix}$$

Output

(a) 0.1 Hz

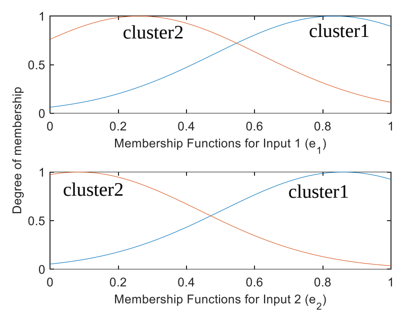

Input

out1cluster1

$$\begin{bmatrix} a_i \\ b_i \\ c_i \end{bmatrix} = \begin{bmatrix} 0.000474 \\ 1.302e-08 \\ -0.000334 \end{bmatrix}$$

out1cluster2

$$\begin{bmatrix} a_i \\ b_i \\ c_i \end{bmatrix} = \begin{bmatrix} 0.0004741 \\ 4.778e-08 \\ -0.000334 \end{bmatrix}$$

Output

(b) 1 Hz

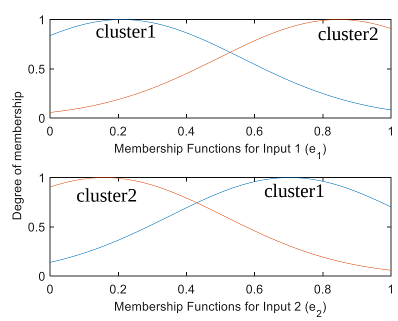

Input

out1cluster1

$$\begin{bmatrix} a_i \\ b_i \\ c_i \end{bmatrix} = \begin{bmatrix} -2.222e-10 \\ 3.067e-05 \\ -1.28e-05 \end{bmatrix}$$

out1cluster2

$$\begin{bmatrix} a_i \\ b_i \\ c_i \end{bmatrix} = \begin{bmatrix} -1.496e-10 \\ 3.067e-05 \\ -1.28e-05 \end{bmatrix}$$

Output

(c) 100 Hz

Figure 8.9. Input and output MFs of Subtractive clustering-based PPF's FISs.

Table 8.4. Subtractive clustering-based PPF'S FISS rules

Frequency	FIS's rules
0.1 Hz 1 Hz 100 Hz	1. If (in1 is in1cluster1) and (in2 is in2cluster1) then (out1 is out1cluster1) (1) 2. If (in1 is in1cluster2) and (in2 is in2cluster2) then (out1 is out1cluster2) (1)

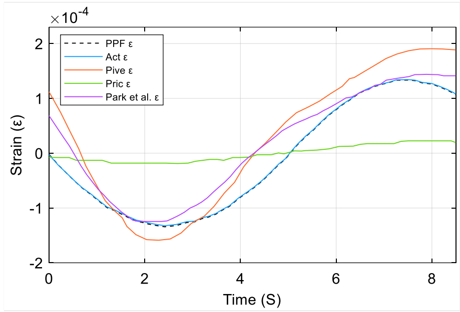

(a) 0.1 Hz

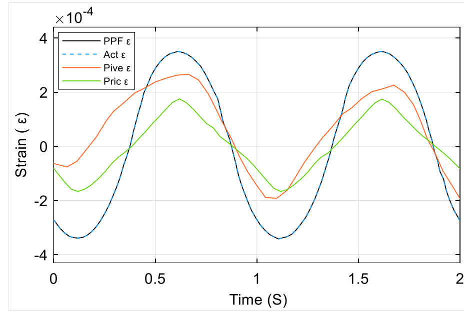

(b) 1 Hz

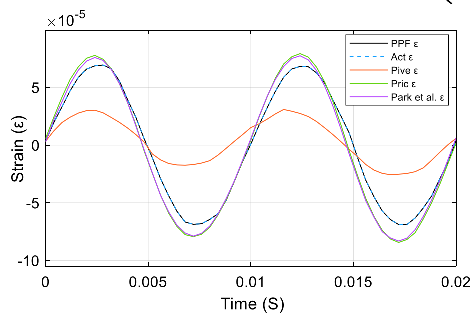

(c) 100 Hz

Figure 8.10. Subtractive clustering based PPF's FISs output fused strain.

100 Hz. A satisfactory performance was achieved using a comparably small number of MFs; only two MFs were used for the three operating frequencies compared to previous methods, which used a higher number of MFs.

The piezoresistive and piezoelectric weights were retrieved in order to analyze the developed subtractive based PPF method, as shown in Fig. 8.11. Higher piezoelectric weights were generated by the PPF method at 1 Hz than at 0.1 Hz and by the piezoresistive weights at 100 Hz, as shown in Fig. 8.11b. This variation is caused by the higher error of both piezoresistive and piezoelectric sensors with respect to the actual strain measurements. Conversely, the generated piezoresistive's weights at 100 Hz were relatively small, as shown in Fig. 8.11c. These generated weights were influenced by the approximately harmonic error shape and comparatively accurate piezoelectric strain sensor. Capturing the error signals' shapes using the fuzzy system thus had a significant impact on the PPF method.

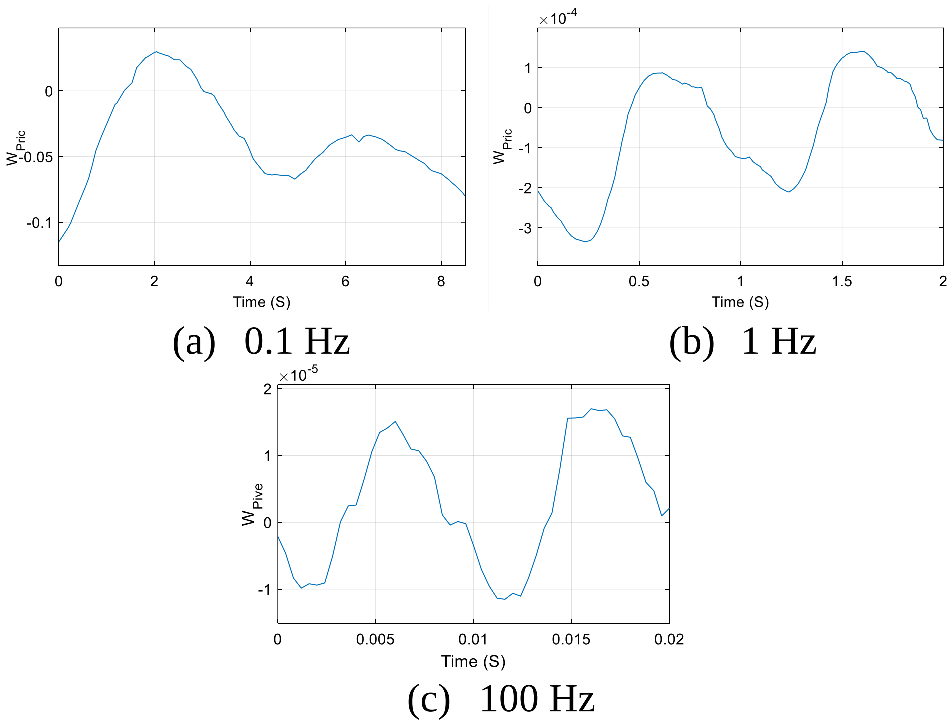

Figure 8.11. Subtractive clustering based PPF's FISs output weights.

8.2.3 Type-2 fuzzy inference system PPF results

A Type-1 fuzzy input MF was used to model the degree of membership for input values within a fuzzy set or cluster in the previous methods. However, this type of input does not incorporate the model uncertainty in the membership's degree. Consequently, the subtractive-based FISs, which were developed in the previous subsection, were converted to Type-2 FISs, as shown in Fig. 8.12. The input MFs were a type-2 fuzzy set, while the type-1 Sugeno system output MFs were kept the same. Each input membership function consists of an Upper MF (UMF) and a Lower MF (LMF), where the UMF matches the type-1 MF. The Footprint of Uncertainty (FOU) spans the region between the Upper and Lower MFs.

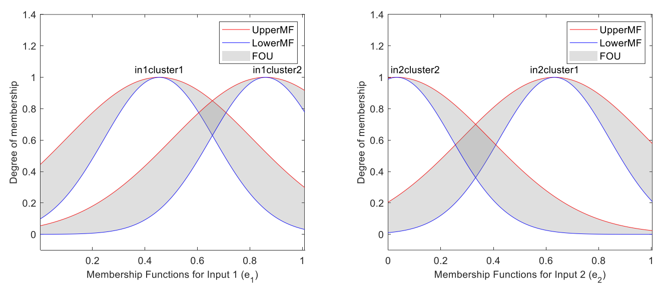

(a) 0.1 Hz

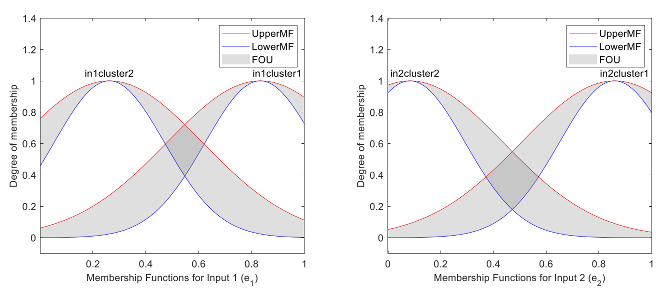

(b) 1 Hz

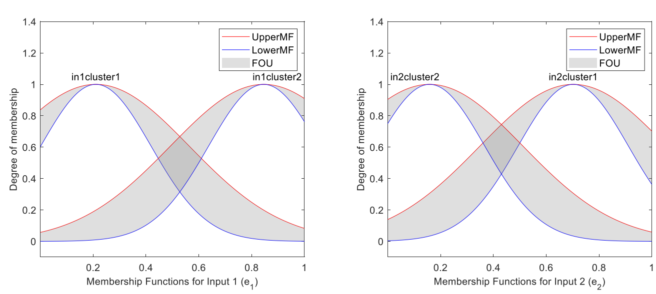

(c) 100 Hz

Figure 8.12. Input MFs of fuzzy Type-2-based PPF's FISs.

As shown in Table 8.4, the subtractive clustering-based FIS's rules were used for the Type-2 FIS's fusion. A total number of two rules were generated and this matched the number of MFs. Unlike the Type-1 Sugeno system, the degrees of membership for LMFs and UMFs were retrieved from the fuzzified inputs' values. As a result, each MF had two fuzzy values. The AND (&) operator was used to combine the fuzzified input's values for each rule resulting in a range of rule firing strengths [126]. To evaluate the output CRISP value, the aggregated Type-2 fuzzy set converted to the Type-1 fuzzy set, which called the centroid of the Type-2 fuzzy set. The KM reduction method was used to iteratively evaluate the centroid [113].

The fuzzy type-2 PPF fusion method was tested and compared with the piezoresistive and piezoelectric strain sensors, as shown in Fig. 8.13. Similar to the result achieved from the subtractive-based fusion method, there was a high agreement between the actual strain measurements and the PPF's fused strains when compared to the Park et al. fusion method at 0.1 Hz and 100 Hz. This performance was accomplished using only two MFs for the three operation frequencies.

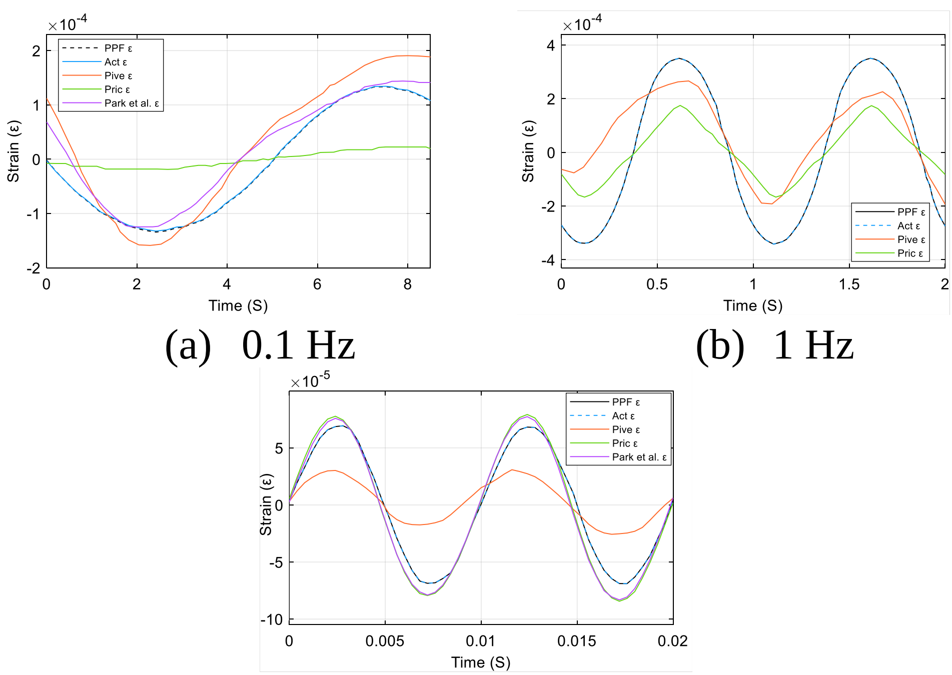

(a) 0.1 Hz (b) 1 Hz

(c) 100 Hz

Figure 8.13. Fuzzy type-2 based PPF's FISs output fused strain.

The RMSE of the developed PPF's FISs were computed, analyzed, and compared with the Park et al. fusion method, as shown in Fig. 8.14. Using the optimization methods, the smallest PPF fused strain's RMSE was recorded as 1.596E-06 at 100 Hz. The maximum RMSE of 2.475E-05 accrued at the 1 Hz strain fusion. The fused strain using the proposed PPF method minimized the RMSE significantly compared to the Park et al. fusion method. The fusion at 1 Hz was not provided in the study [39], so it was not compared with the current fusion method. For the FCM-based PPF, the smallest RMSE of 4.43E-06 was calculated at 100 Hz using the PPF method. Compared to the Park et al. fusion method, the proposed PPF method obtained more accurately fused strain measurements. The smallest RMSEs of 5.18E-09 and 3.77E-11 were found at 1 Hz and 100 Hz; respectively, using the subtractive clustering-based PPF method. At 1 Hz, the RMSE was found to be to be 2.628E-05, approximately similar to the RMSE of the optimization-based FIS. Both the FCM and the optimization-based FISs were based on Mamdani FIS, which does not overcome the Sugeno FIS in the nonlinear dynamic application. On the contrary, the PPF successfully estimated the fused strain at 1 Hz and 100 Hz, using the subtractive-clustering and fuzzy Type-2-based methods. An average RMSE of 2.64E-09 was estimated at these frequencies. In addition, at the low frequency strain measurement fusion of 0.1 Hz, both the cluster-based PPF fusions minimized the RMSE compared to the Park et al. fusion. Combining the subtractive clustering with a type-2 FIS resulted in reducing the RMSE by approximately 4%. This improvement was gained by the model uncertainty feature of the fuzzy type-2 PPF. The developed PPF's FISs, based on the type-2 fuzzy method, successfully fused the piezoresistive and piezoelectric measurements and produced accurately fused strain measurements.

The results of this study indicate that a real time wide band nanocomposite strain sensor can be achieved using the proposed PPF method. The subtractive-based PPF utilized the smallest number of MFs, two MFs, in the three operation frequencies to perform the fusion which minimized the computation time required for real time fusion of strain measurements. Similarly, the optimization-based PPF fused both the MWCNT/PVDF measurement's characteristics and had the same number of MFs at 0.1 Hz and 100 Hz with relatively higher RMSEs. The fuzzy Type-2 system and subtractive-based PPF had the same number of MFs, two, and approximately similar RMSEs. The FCM clustering-based PPF contained

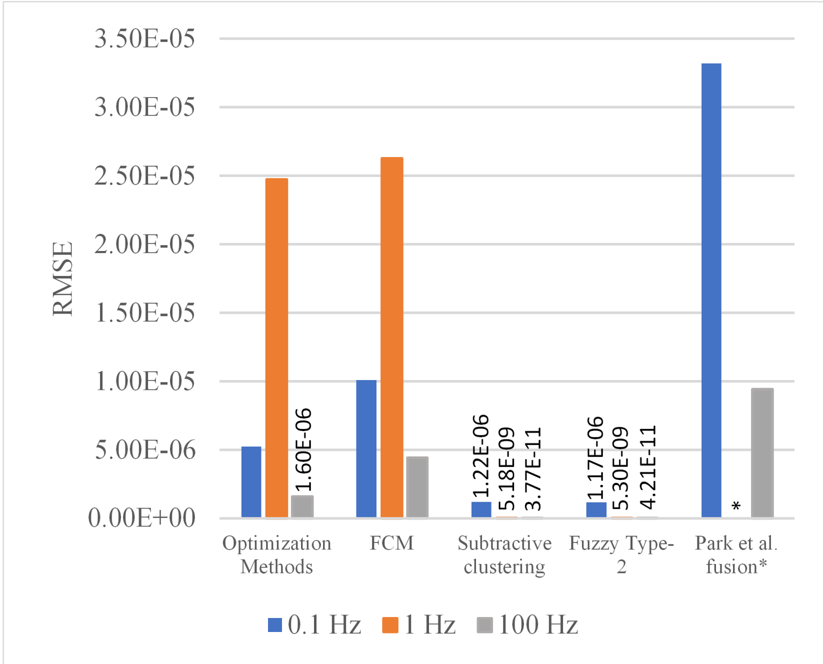

* Fusion at 1 Hz is not provided in the study Park at el. [41].

Figure 8.14. Fused strain's RMSE using PPF's FISs at different frequencies and compared with Park et al. fusion's [39] RMSE.

the highest number of MFs, 20 and 6 MFs, compared to the other derived FISs. The PPF successfully fused the piezoresistive and piezoelectric characteristics at their optimal performance and sensitivity. In the current study, the estimates of the actual strain measurements were assumed to be available.

8.3 Cantilever vibration results

The piezoresistive and piezoelectric measurements were investigated using a cantilever beam under different vibration frequencies, as shown in Fig. 4.12. This experiment was conducted to identify the operating frequencies for each characteristic. Also, these limitations were used to assign weight during the DPPF and EPPF generating processes. Testing was completed under vibrations of 0.5 Hz, 1 Hz, 5 Hz, 10 Hz, 50 Hz, 100 Hz, and 1000 Hz. The FFT results were retrieved for the piezoresistive and piezoelectric measurements at these frequencies, as shown in Fig. 8.15 and Fig. 8.16. The piezoresistive signals were more sensitive at frequencies 0.5 Hz, 1 Hz, and 5 Hz compared to the piezoelectric measurements. At the 10 Hz excitation, the piezoelectric measurement achieved a slightly higher SNR of 15.99 dB than the piezoresistive signal's SNR of 13.43 dB. The piezoelectric measurement became more apparent and was not affected by the electric hum, which had a fundamental frequency of 60 Hz. On the other hand, the piezoresistive signal's magnitude was lower, yet it was not affected by the noise.

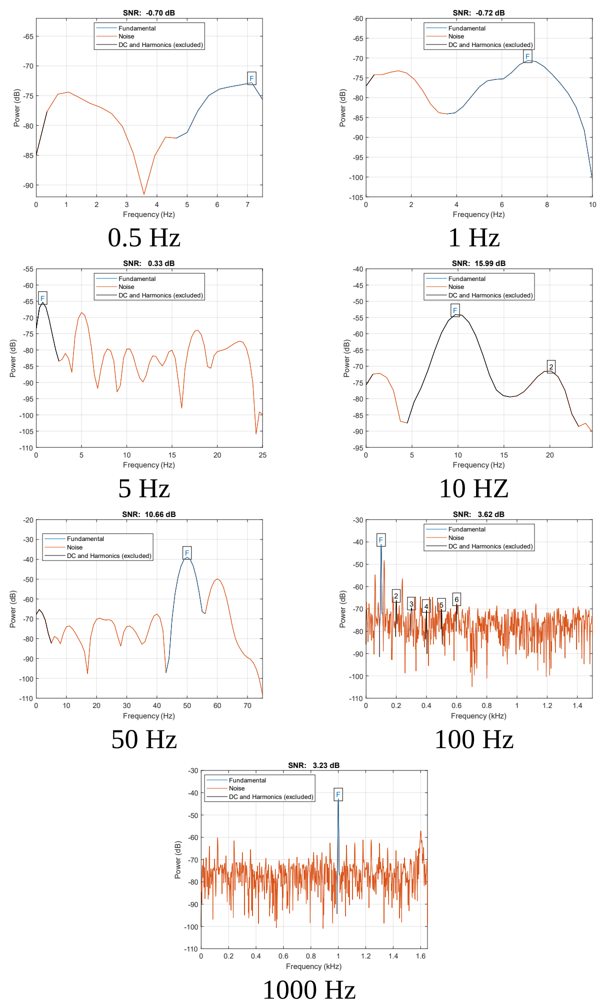

Figure 8.15. The piezoelectric measurements' FFT at the cantilever testing setup.

At 100 Hz, the piezoresistive sensor presented high-frequency noises compared to the piezoelectric sensor. In addition, the piezoelectric sensor was accurate at 1000 Hz, while the piezoresistive sensor underwent large low-frequency noises. As a result, the piezoresistive sensor illustrated good signal characteristics at frequencies below 50 Hz, while the piezoelectric sensor's measurements were less sensitive to noises.

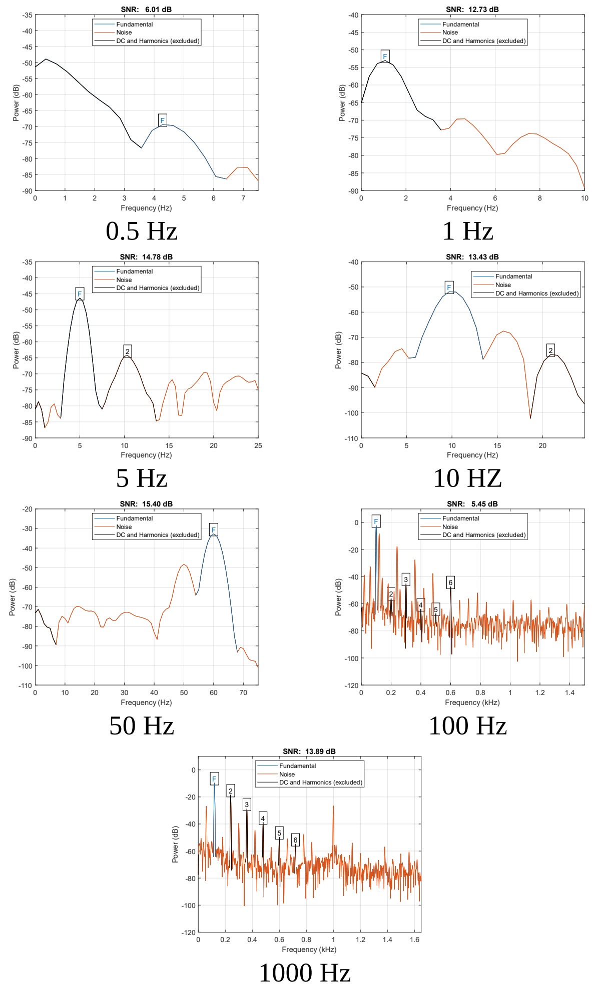

Figure 8.16. The piezoresistive measurements' FFT at the cantilever testing setup.

8.4 Direct Piezoresistive/Piezoelectric Fusion (PPF) results

The piezoresistive and piezoelectric characteristics of the MWCNT/PVDF strain sensor were influenced by the operating frequency. The piezoresistive sensing element was more sensitive at low frequencies, while the piezoelectric sensor had was more accurate at higher frequencies [39]. As a result, the DPPF and EPPF were proposed to fuse both measurements at specific frequencies and a range of frequencies, respectively. The performances of both characteristics were investigated using a vibrating cantilever at different frequencies. In addition, a 3D force sensor was fabricated and assembled. The piezoresistive and piezoelectric measurements were taken at the elastic beams of the 3D force structure and were fused using the DPPF and EPPF methods. The subtractive clustering technique was used to generate and tune the proposed methods.

8.4.1 3D force sensor vibration results and the DPPF

The 3D force sensor was fabricated and tested for the fusion of strain measurements and characteristics. The cantilever experiment proved the sensitivity of the piezoresistive sensor at lower frequencies. In addition, the piezoelectric sensor showed good sensitivity at frequencies above 50 Hz. As a result, the piezoresistive and piezoelectric measurements were assumed to be accurate at lower and higher frequencies, respectively. However, each type of sensor showed a lower content signal at the other sensor type's accurate measurement frequency. The DPPF utilized the piezoresistive and piezoelectric's measurements to achieve an accurate strain measurement.

The 3D force sensor was tested at 2 Hz, 5 Hz, 10 Hz, and 100 Hz under Z-axis and X-axis loading scenarios. At the three lower frequencies, the piezoresistive sensor was assigned the total weight of one, while piezoelectric sensors' weights were computed using Equation 5.3. At 100 Hz, the piezoelectric sensors' weights were computed using Equation 5.2 and the weight of one that had been appointed for the piezoresistive sensors. The input MFs, the output MF's linear equation constant, and the rules were generated and tuned using the piezoresistive measurement, piezoelectric measurement, and the computed desired weight. For each FIS, a set of rules was generated to relate the FIS's input and output MFs, as shown in Table 8.5. Each resultant input membership function consisted of multiple data sets or clusters, where the number of MFs equaled the number of clusters and rules. The same rules table was generated for each FIS except number of rules (n), which depended on the MF's number.

Table 8.5. The DPPF'S FISs rules

FIS's rules
1. If (in1 is in1cluster1) and (in2 is in2cluster1) then (out1 is out1cluster1)
2. If (in1 is in1cluster2) and (in2 is in2cluster2) then (out1 is out1cluster2)
……
n. If (in1 is in1cluster n) and (in2 is in2cluster n) then (out1 is out1cluster n)

Z-axis loading scenario

The resultant FISs' input MFs for the operating frequencies were retrieved from the Z-axis loading test, as shown in Fig. 8.17. The 3D force sensor consisted of four beams in the ± X-direction and the ± Y-direction. At each frequency, two input variables were assigned for each beam's DPPF's FIS. These input variables were the piezoresistive and piezoelectric strain measurements. The input MFs' range spanned the values from the minimum to maximum piezoresistive and piezoelectric strain measurement data. At the same time, the degrees of membership spanned the values from zero to one. The number of MFs at each beam and frequency was determined by the number of clusters assigned to represent the relationship between the strain measurements and desired weight by the subtractive clustering method. The cluster influence range was the spatial parameter that decided if an input/output data point was considered part of a specific center group. It was a scalar number ranging from zero to one. In this manner, the number of MFs assigned by the cluster influence range was defined for each test. For each scenario, the cluster influence range was adjusted manually to achieve the best estimate of the actual strain with a minimum number of MFs. At least three MFs were utilized by two beams at the excitation of 2 Hz and 5 Hz, as shown in Fig. 8.17a, b. At the frequency of 2 Hz, because of the lower cluster influence range, as shown in Fig. 8.17a. Only four MFs were utilized for the DPPF's FISs at the four beams under 10 Hz excitation in the Z-direction, as shown in Fig. 8.17c. Similarly, the input MFs at the beams, which vibrated at 100 Hz, used four MFs of the FIS's input variables except at the +Y beam. The four MFs were achieved using a cluster influence range of one.

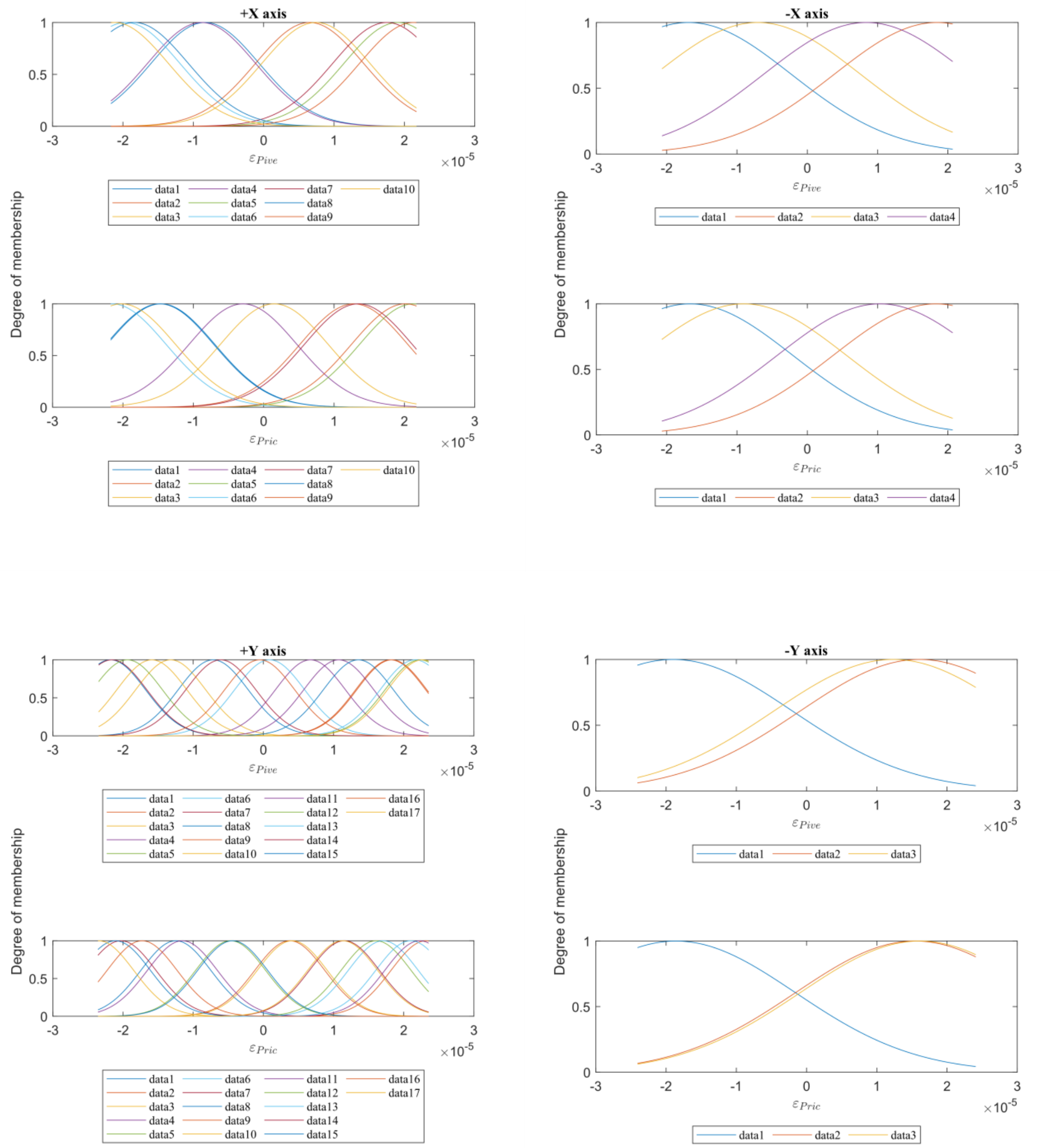

(a) 2 Hz

Figure 8.17. Input MFs of Subtractive clustering based DPPF's FISs.

Figure 8.17 continued

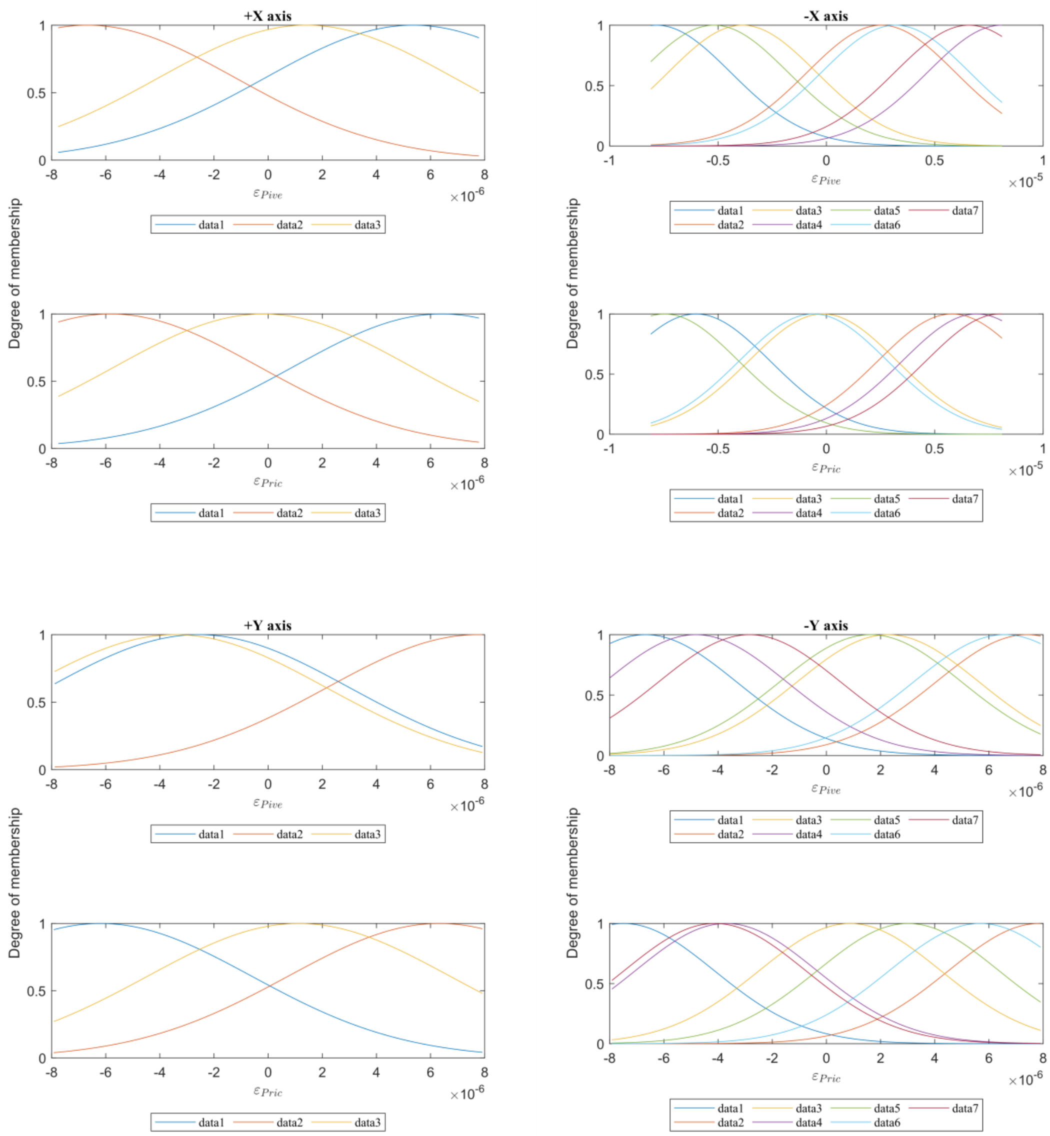

(b) 5 Hz

Figure 8.17 continued

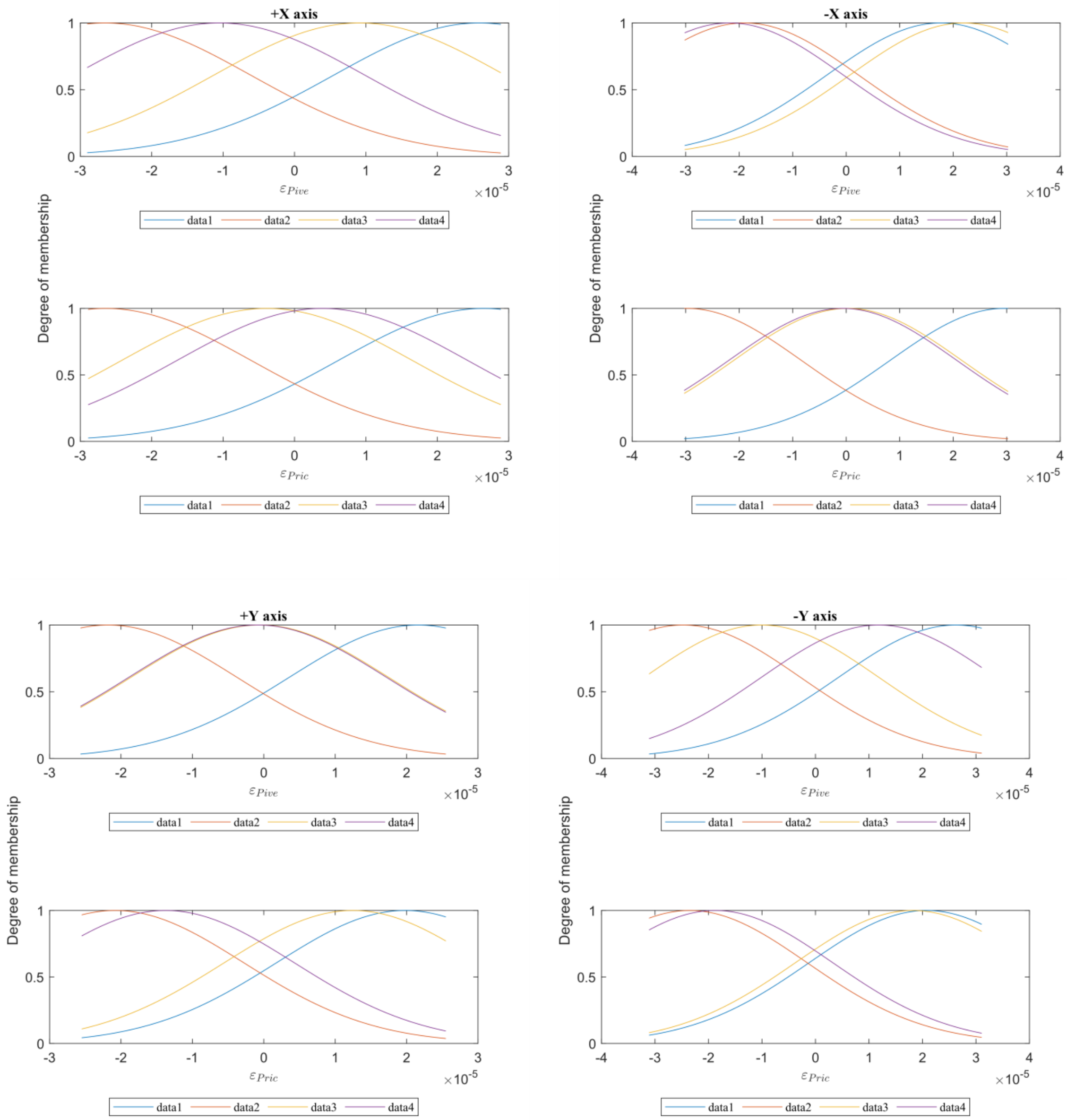

(c) 10 Hz

Figure 8.17 continued

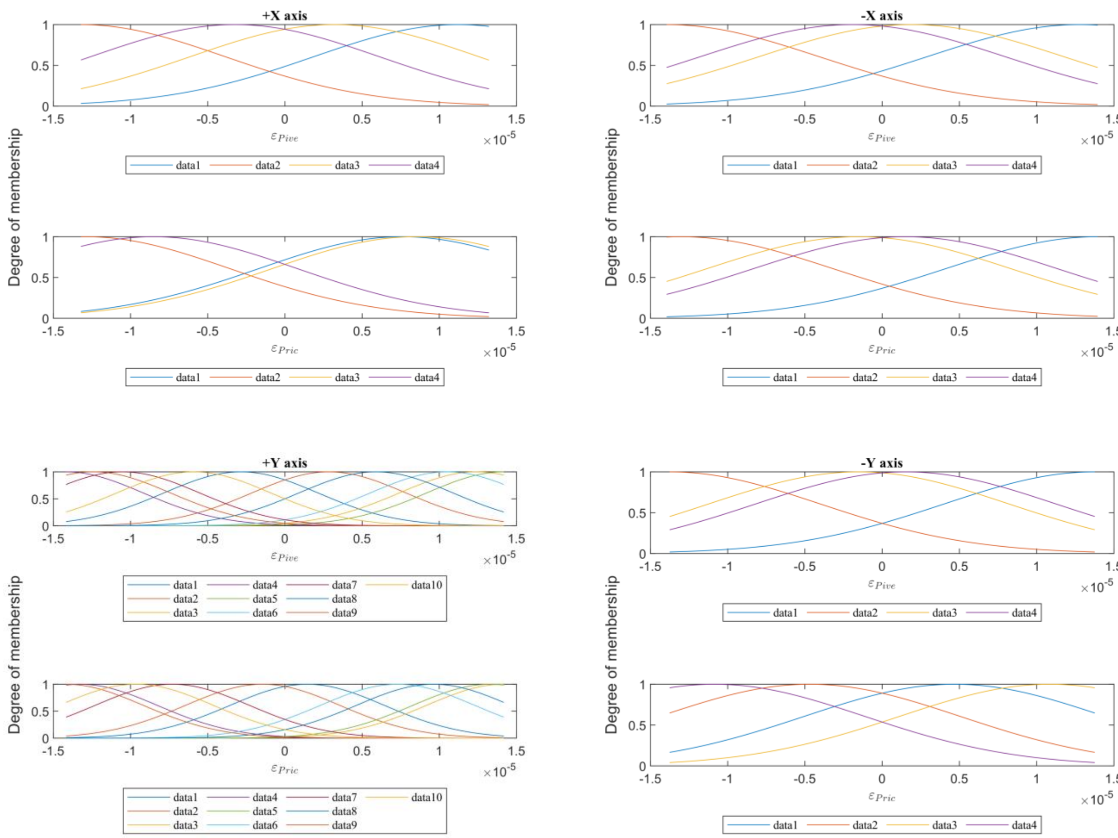

(d) 100 Hz

The rule output level's Z_i coefficients were generated, and only one of the output MFs of the -X beam under 2 Hz excitation were plotted, as shown in Fig. 8.18. The rest of the output MFs at each beam and frequency followed the same process. Table A.1 located in the Appendix illustrates the MFs' rule output level's coefficients. The number of outputs for each MF equals the number of clusters, input MFs, and assigned rules for each MF. As a result, four output clusters were generated for the -X beam under the vibration of 2 Hz. In equation 8.1, piezoresistive and piezoelectric strain measurements and coefficients assigned by the subtractive clustering method were used to calculate the rule's output level Z_i. In addition, the number of rules was four (n=4), as shown in Table 8.5.

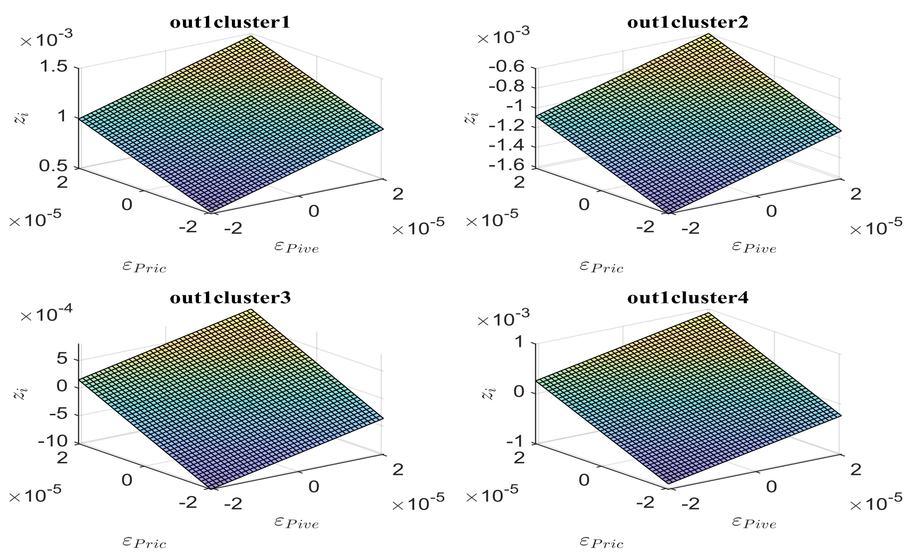

Figure 8.18. -X beam output MFs under 2 Hz excitation for PPF's FISs.

The proposed Simulink model was used to test and validate the resultant DPPF's FISs. The FISs used the piezoresistive and piezoelectric strain measurements as inputs and the outputs were based on the appropriate operating frequency. The DPPF's fused strains were calculated using Equation 5.4 and the FIS's output weight. The DPPF's fused strains were retrieved and compared with the measurements' characteristics, measurements from reference strain gauges, and the nlhw model's estimated measurements, as shown in Fig. 8.19. The DPPF's fused strains agreed closely with the reference strain gauges when the 3D force sensor was excited at the Z-axis. At 10 Hz, the nlhw model's strain estimate was more

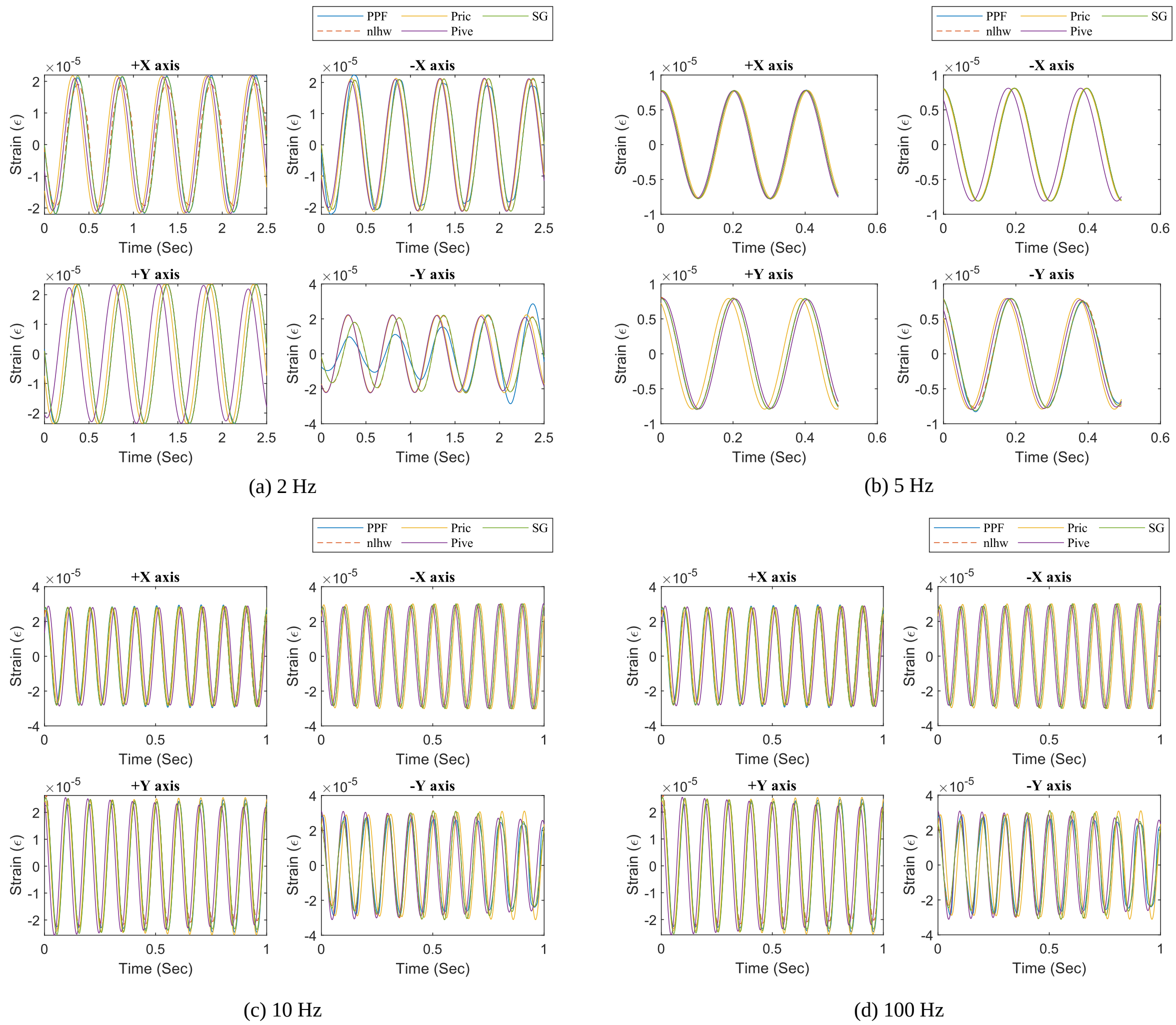

(a) 2 Hz (b) 5 Hz

(c) 10 Hz (d) 100 Hz

Figure 8.19. Z-axis loading results of the DPPF.

accurate than the DPPF's fused strains at the -X beam (2 Hz), the +Y beam (2 Hz), and the -Y beam (10 Hz). However, the DPPF method did successfully fuse both measurements and therefore achieved more accurate results.

In this work, different nlhw models were used to estimate the actual strain from either the piezoresistive or the piezoelectric sensors at three lower frequencies and 100 Hz, respectively. MATLAB's system identification toolbox was used to produce the best fit actual strain estimate. Different nlhw model structures were generated for the strain measurements at the Z-axis loading test's 3D force sensor beams. These estimators had different zeros and

Table 8.6. The nlhw models used at Z-loading strain estimation.

Test	Zeros	Poles	Model	Nonlinearity
Z 2HZ	3	4	Hammerstein-Wiener	pwlinear
Z 5HZ	2	3	linear	-
Z 10HZ	3	4	Hammerstein-Wiener	pwlinear
Z 100HZ	2	3	Wiener	pwlinear

poles, different model structures, and different nonlinear functions, as shown in Table 8.6. A similar Hammerstein-Wiener model structure was used at 2 Hz and at 10 Hz to achieve the best fit actual strain estimates from the piezoresistive measurements. At the 5 Hz strain estimate, a linear model was used with two zeros and three poles. At 100 Hz, the actual strain estimate was provided using the Wiener model. The piecewise linear function nonlinearity estimator was implemented at 2 Hz, 5 Hz, 10 Hz, and 100 Hz.

The DPPF's FISs generated the desired piezoelectric and piezoresistive weights at the lower and higher frequencies, respectively. The FIS's output weights were recorded for each beam and at each frequency to analyze the DPPF's performance, as shown in Fig. 8.20. The total weight of one was assigned for piezoresistive and piezoelectric strain signals at 2 Hz, 5 Hz, 10 Hz, and 100 Hz, respectively. Relatively higher piezoelectric weights were assigned at 2 Hz and 10 Hz for the fused strain due to the presence of error at these frequencies. Conversely, the generated weights at 5 Hz and 100 Hz were relatively less, due to the accuracy of piezoresistive and piezoelectric sensors at these frequencies, respectively.

X-axis loading scenario

The DPPF's FISs for the X-axis scenario were produced using the same methodology utilized for the Z-axis scenario. The developed FISs' input MFs for the operating frequencies were retrieved at the X-axis loading test, as shown in Fig. 8.21. Multiple FISs attained four MFs as their input variables, where the cluster influence ranges were assigned to be one. On the other hand, the highest number of inputs MFs was achieved at the +X-axis and +Y-axis FISs under an excitation of 2 Hz, as shown in Fig. 8.21a. The cluster influence ranges for the FIS's piezoresistive and piezoelectric inputs' MFs at +Y beam (2 Hz) were

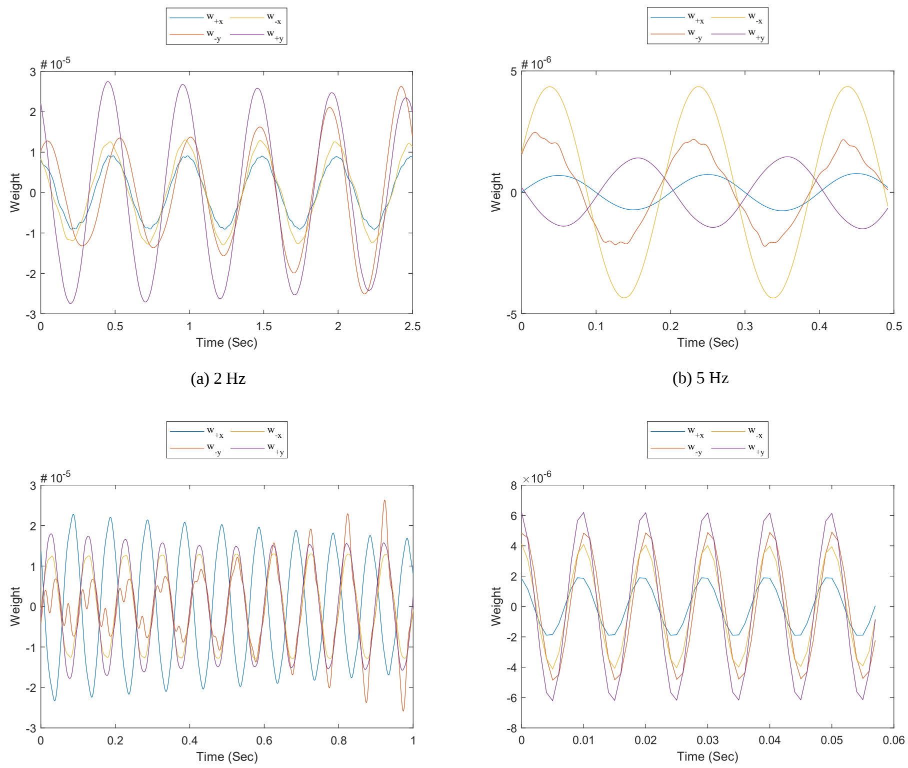

(a) 2 Hz (b) 5 Hz

(c) 10 Hz (d) 100 Hz

Figure 8.20. The DPPF's generated weights for piezoelectric and piezoresistive sensors at the Z-axis loading test.

0.4 and 0.3, respectively, which resulted in 21 MFs. The output MFs and rule output levels were generated using the same procedure that was used for the Z-axis loading fusion. Refer to Table A.2 in the Appendix for the MFs' rule output level's coefficients. Each beam's FIS used the same set of rules in Table 8.5. However, the number of rules (n) used matched the same number of input/outputs MFs.

Using the Simulink model, the generated DPPF's FISs were tested and analyzed in the X-axis loading scenario. The generated DPPF's fused strain, strain measurements, reference strain gauge measurements, and nlhw models' estimations, were obtained and presented, as shown in Fig. 8.22. The DPPF method merged both measurements and achieved accurately fused strain measurements. On the other hand, the nlhw models provided good actual strain estimates at most frequencies. Under the Z-axis loading test at 2 Hz, phase shifts were

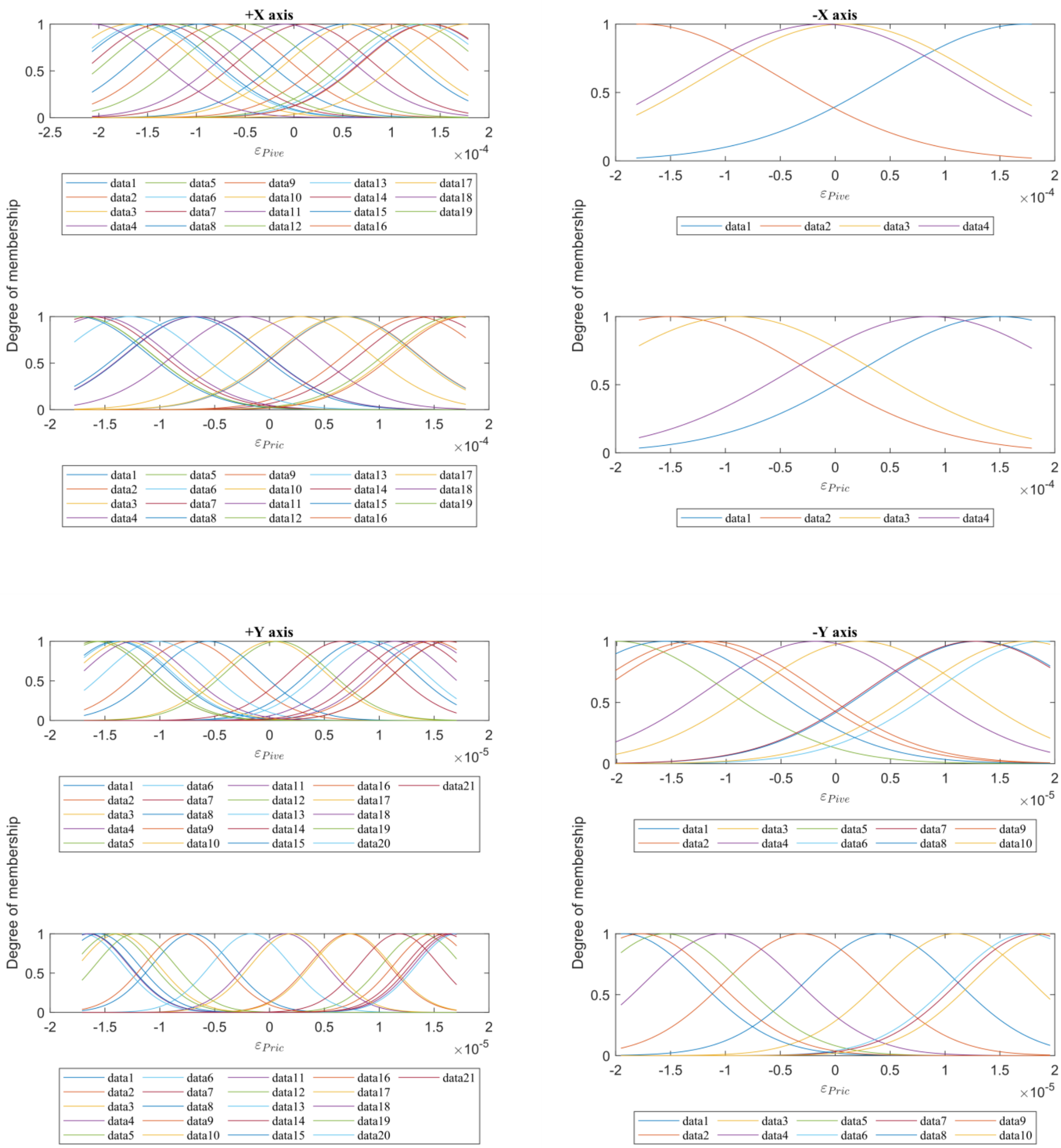

(a) 2 Hz

Figure 8.21. Input MFs of subtractive clustering based DPPF's FISs for X loading test.

Figure 8.21 continued

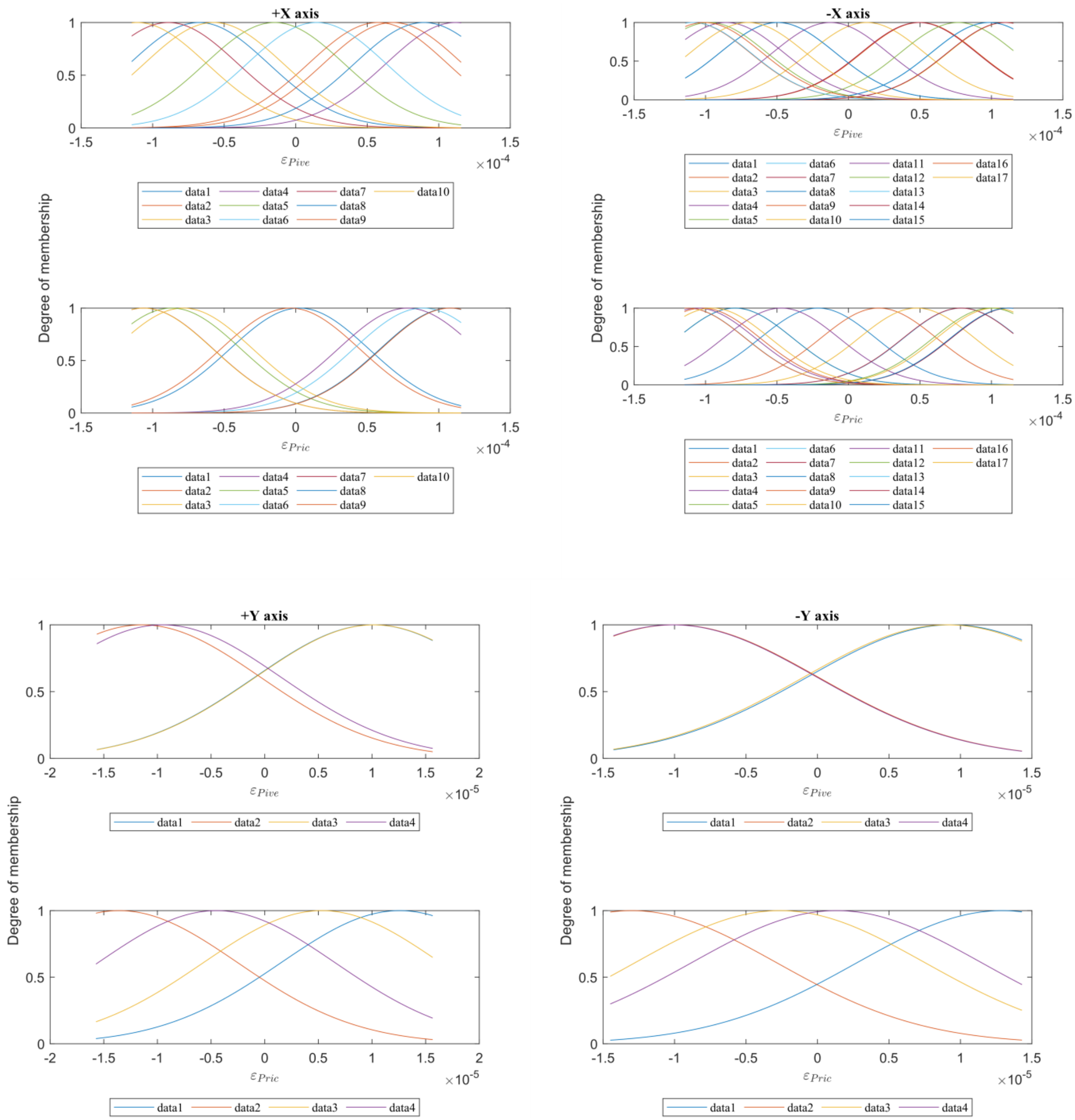

(b) 5 Hz

Figure 8.21 continued

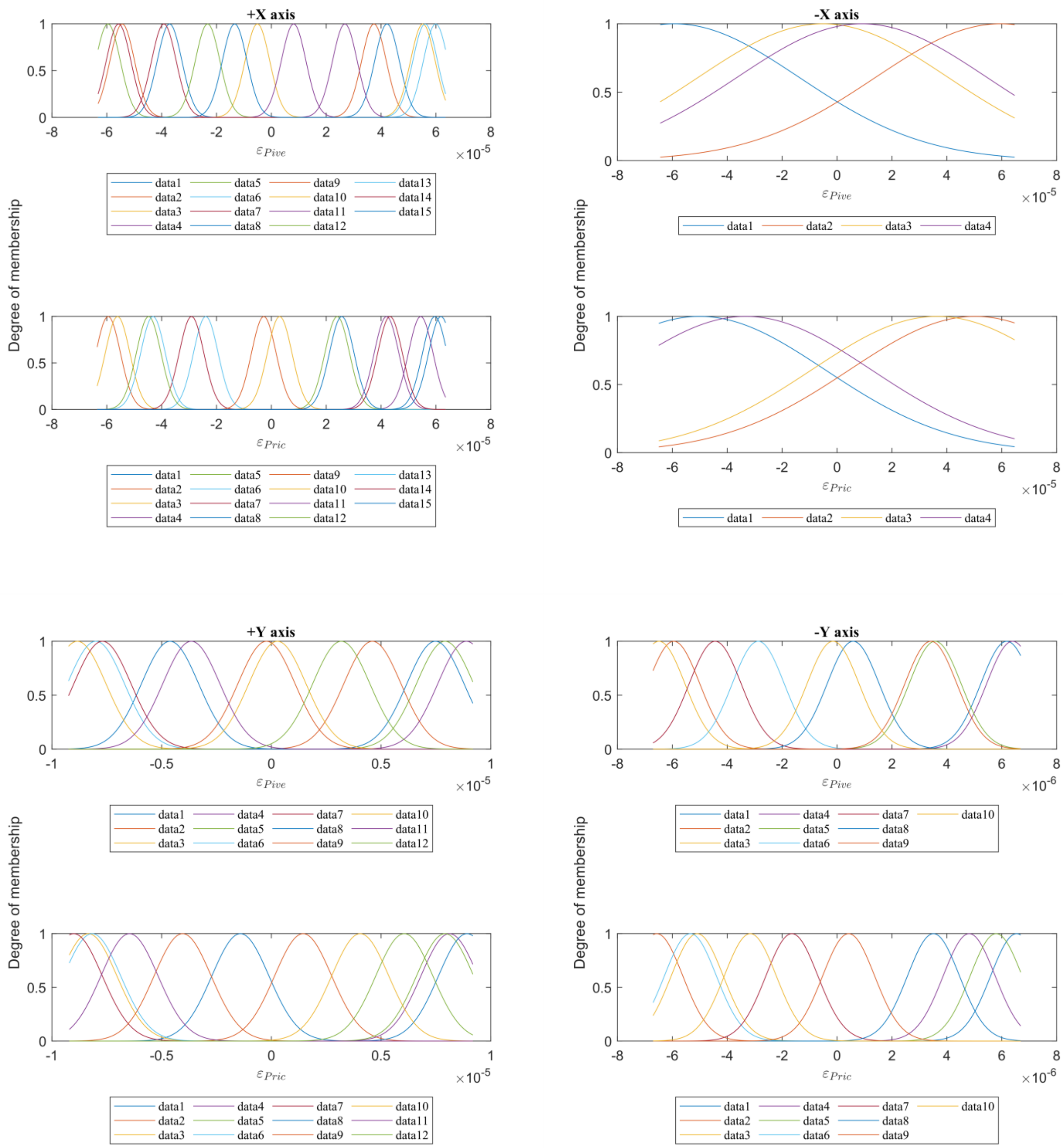

(c) 10 Hz

Figure 8.21 continued

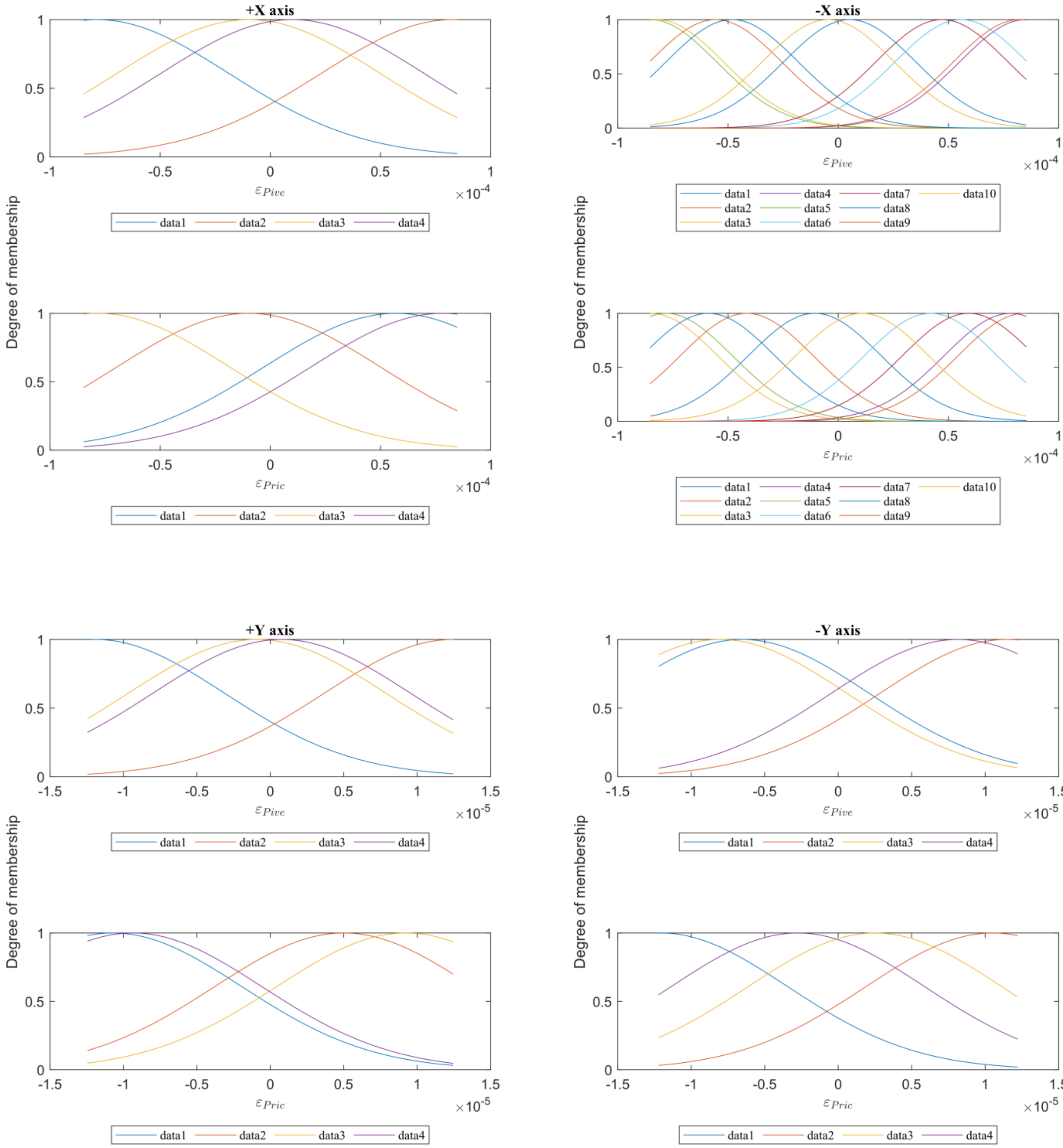

(d) 100 Hz

observed in both the piezoresistive and piezoelectric strain measurements compared to the strain gauges' measurement, as shown in Fig. 8.22a. These differences resulted from the variations in capacitance, C1, used for the piezoresistive and piezoelectric circuits in both loading experiments. The sets of n rules used by each beam's FIS matched the same number of input/outputs MFs.

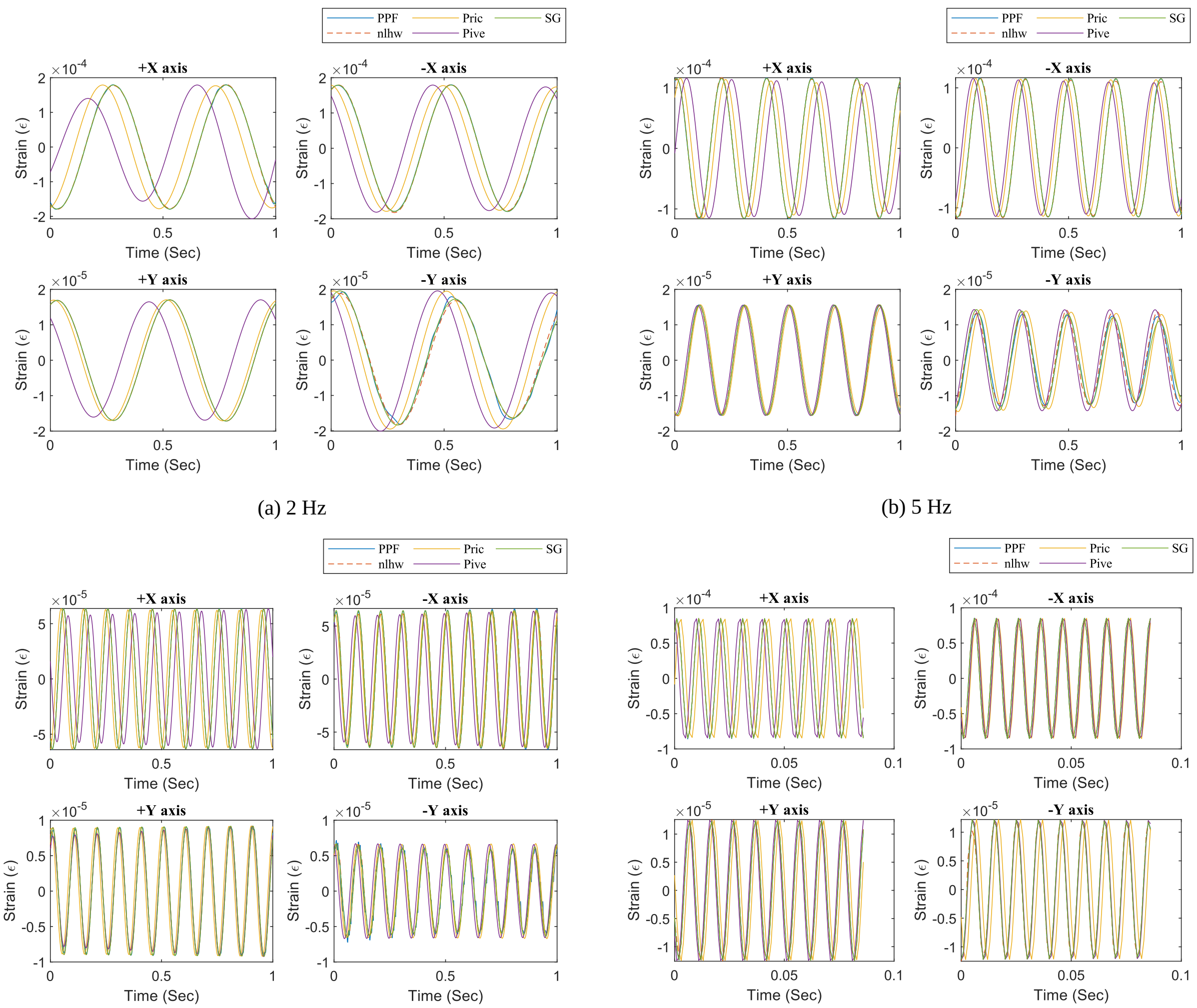

(a) 2 Hz

(b) 5 Hz

(c) 10 Hz

(d) 100 Hz

Figure 8.22. X-axis loading results of the DPPF.

As shown in Fig.8.22, the nlhw models produced perfect estimates for the strain measurements at the 3D force sensor's beams in the X-axis vibration experiment. The parameters used to generate these models are shown in Table 8.7. A Wiener model structure was used for the three highest frequencies, which achieved the best fit of actual strain estimates. The Wiener models utilized the piecewise linear function nonlinearity estimator for the structure output's nonlinear blocks. A linear model was used for strain estimate at an excitation of 5 Hz with the highest number of zeros and poles of four and five, respectively. The same Wiener model structure was used for both the Z-axis and X-axis loading test under 100 Hz for the 3D force sensor's beams.

Table 8.7. The nlhw models used at X-loading strain estimation

Test	Zeros	Poles	Model	Nonlinearity
X2HZ	4	5	linear	-
X5HZ	3	4	Wiener	pwlinear
X10HZ	3	4	Wiener	pwlinear
X100HZ	2	3	Wiener	pwlinear

The desired piezoelectric and piezoresistive weights were generated by the DPPF's FISs at the lower and higher frequencies, respectively. The output weights were retrieved to investigate the DPPF's performance for the fusion of every beam strain, as shown in Fig. 8.23. Similar to the Z-axis loading characteristics' fusion, the piezoresistive strain signals at excitations of 2 Hz, 5 Hz, and 10 Hz were given a weight of one. On the other hand, the piezoelectric measurements were accorded the total weights at 100 Hz vibration. The designed FIS produced higher weights at the 2 Hz and 5 Hz frequencies due to the more significant inherited phase shift of the piezoresistive and piezoelectric strain measurement at the elastic structure's beams. Conversely, lower weights were assigned at the Y-axis beams because of the loading in the X direction and minimum strain measurements at the Y-axis beam's sensing placements.

3D force sensor vibration and the EPPF

The strain measurements were fused using a single FIS for a specific operating frequency. This method restricted the DPPF method from performing at a single frequency or local fusion. As a result, the EPPF was introduced to perform the fusion at a wide range of frequencies. The piezoresistive measurements was more reliable at the 2 Hz, 5 Hz, and 10

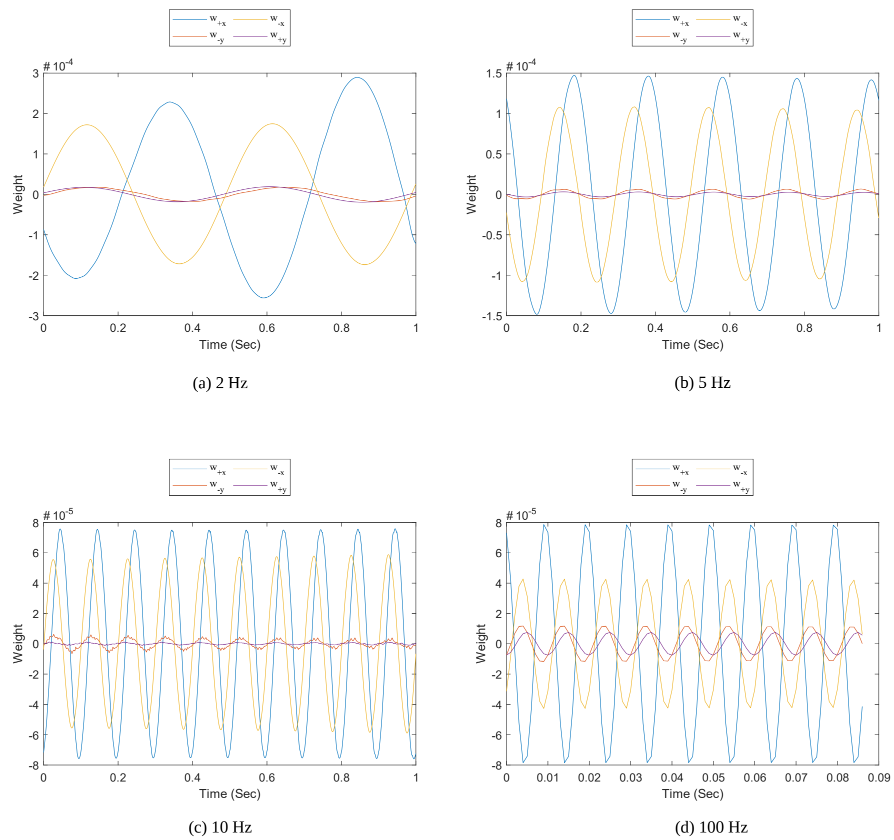

(a) 2 Hz (b) 5 Hz

(c) 10 Hz (d) 100 Hz

Figure 8.23. The DPPF's generated weights for piezoelectric and piezoresistive sensors at the X-axis loading test.

Hz frequencies than were the piezoelectric measurements. The EPPF's FIS fused the strain measurement at these frequencies. The whole piezoresistive strain value was considered in equation 5.4, while the FIS generated the needed weight to achieve accurately fused strain results. The EPPF was produced and tested only for the +X and +Y beams. Each beam was treated as a separate system of a singly supported beam. The previous piezoresistive, piezoelectric, and strain gauge measurement data obtained from the two-directional loading and three frequencies were cascaded for each beam separately. In this way, a single signal contained the three frequencies for each measurement at every loading scenario. These measurements were used to generate the EPPFs' FISs from which their input MFs were retrieved, as shown in Fig. 8.24. A single FIS was generated for each set of directional loading experimental data. The +X beam's FISs had higher numbers of MFs compared to the +Y beam's FISs. Six input MFs were generated for the +Y beam from the Z-axis loading condition data and four input MFs were generated for the +Y beam under the X-axis loading condition data. The output MFs and rule output levels were generated using the same method that was used in the Z-axis loading fusion. Refer to Table A.3 in the Appendix for the MFs' rule output level's coefficients.

The EPPF's MFs were investigated due to the notable difference in MF numbers between +X and +Y beams. The clustering tool in MATLAB was used to identify and analyze the number of MFs in each of the four cases. The relationship and the cluster numbers were generated using the piezoresistive strain measurement, piezoelectric strain measurement, and the desired piezoelectric weight, as shown in Fig. 8.25. Only the cluster influence range was used to produce the EPPF's FISs, while other clustering parameters were kept at the default values. At the +X beam's FISs, three approximately concentric ellipses were used to represent the relationship between the piezoresistive strain, piezoelectric strain, and the piezoelectric sensor's weight. Each elliptical function corresponds to a particular frequency's desired piezoelectric weights. This correspondence required a higher number of clusters, leading to a more significant number of MFs required for more accurately fused strain values. Conversely, the interaction of two or more of these ellipses for the +Y beam minimized the number of clusters needed to perform the fusion, because one cluster or MF could be utilized for multiple frequencies fusion. As shown in Fig. 8.25d, the smallest number of three MFs was assigned based on the given data due to the relatively smaller areas and high interfaces of these functions.

The generated EPPF's FISs were tested and analyzed in the 3D force sensor using the cascaded data and the Simulink validation model. The EPPF's fused strain was then compared with the piezoresistive and piezoelectric measurements, nlhw models estimates, and strain gauge measurements, as shown in Fig. 8.26. The EPPF's fused strains tracked well with the measurements from the reference strain gauges for the two beams in the Z-axis and X-axis loading experiments. Even though the original data was cascaded from the previous experiments, there were smooth transitions between the strain measurements through the different frequencies compared to the nlhw models.

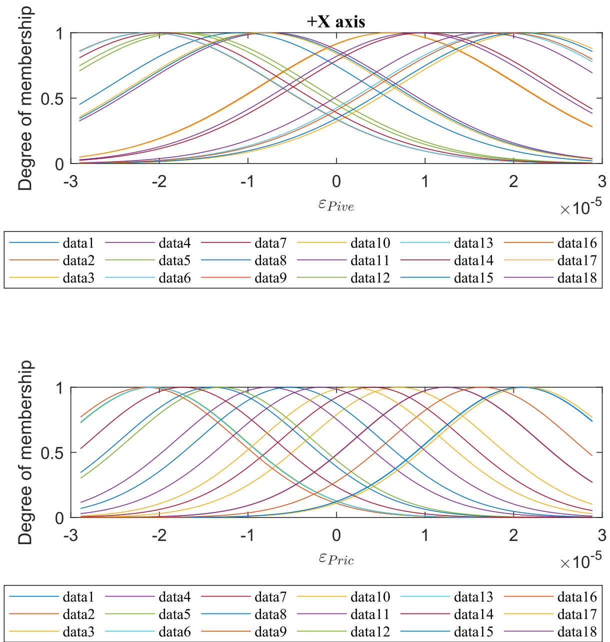

(a) Z-axis loading (+X beam)

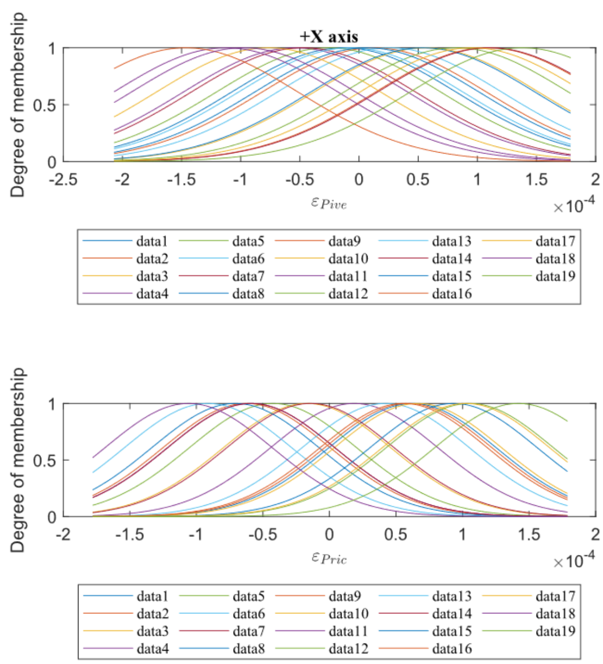

(b) X-axis loading (+X beam)

Figure 8.24. Input MFs of the EPPF's FISs for the +X and +Y beams.

Figure 8.24 continued

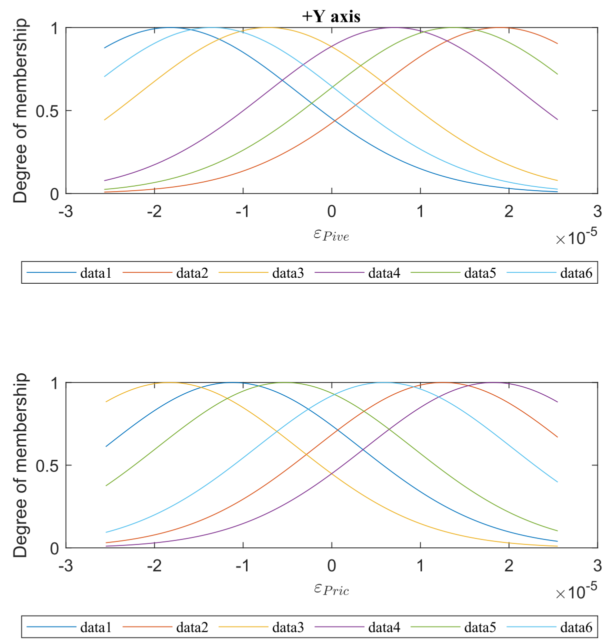

(c) Z-axis loading (+Y beam)

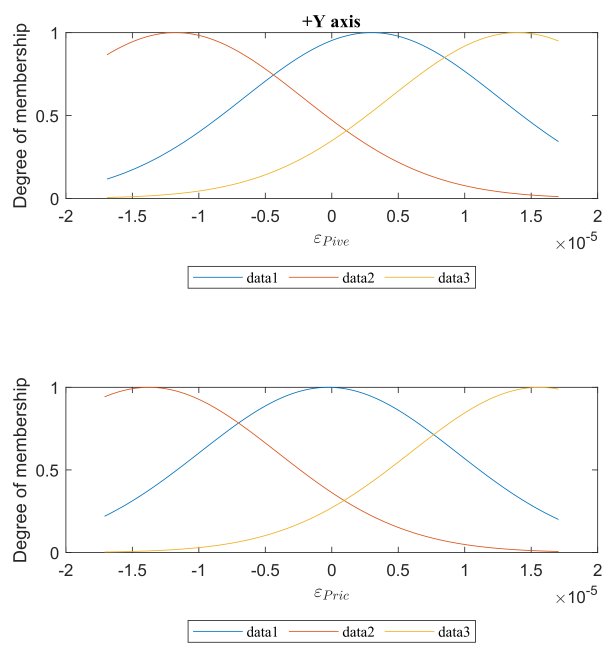

(d) X-axis loading (+Y beam)

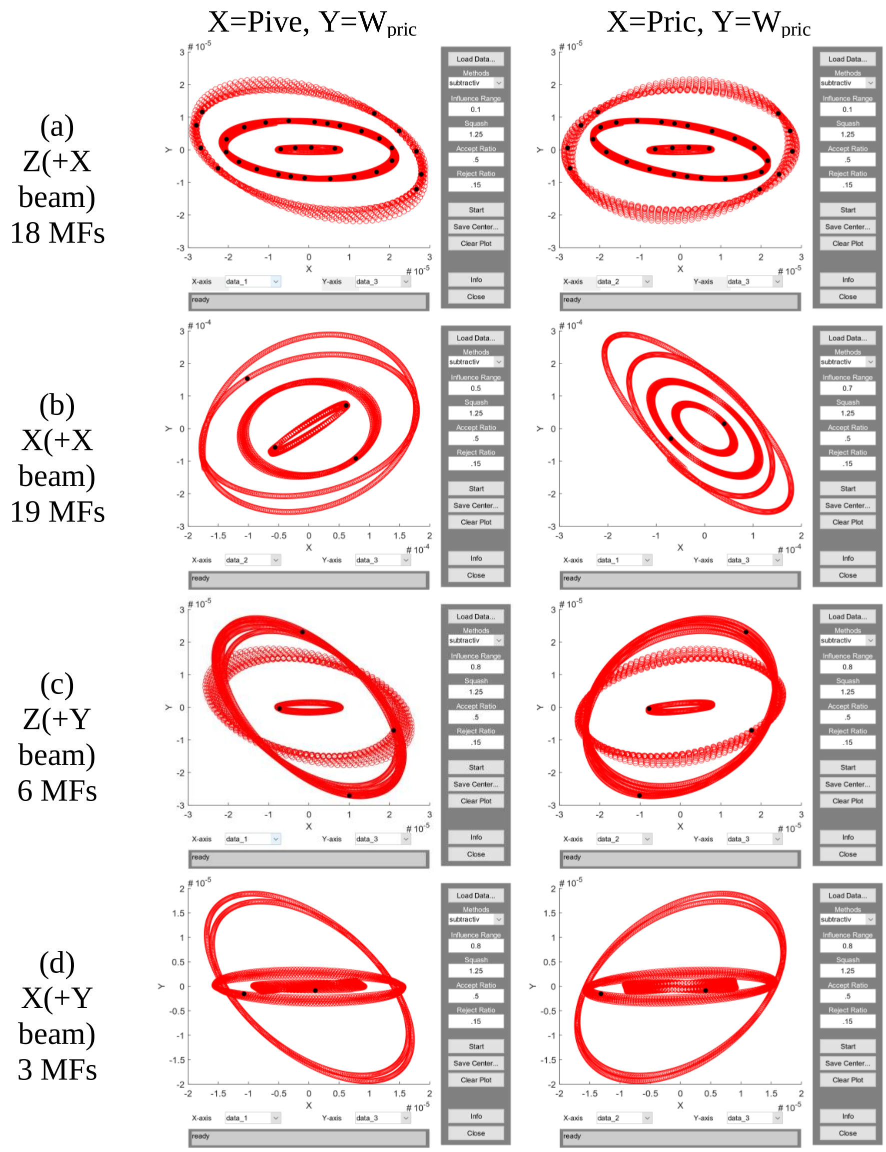

Figure 8.25. EPPF number of MFs and clusters investigation.

The nlhw model produced good estimates for the actual strains using the piezoresistive measurements at each beam. The best actual strain estimates were reached using the nlhw model parameter shown in Table 8.8. The Hammerstein model was chosen for the estimate for all tests except the the X-axis loading of +Y beam, which instead used a linear model with 19 zeros and 20 poles. The input sigmoid network function was used for the Hammerstein model, which utilized 18 zeros and 19 poles.

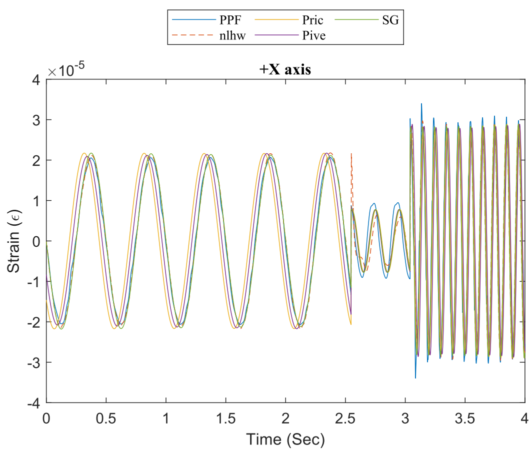

(a) Z axis loading (+ X beam)

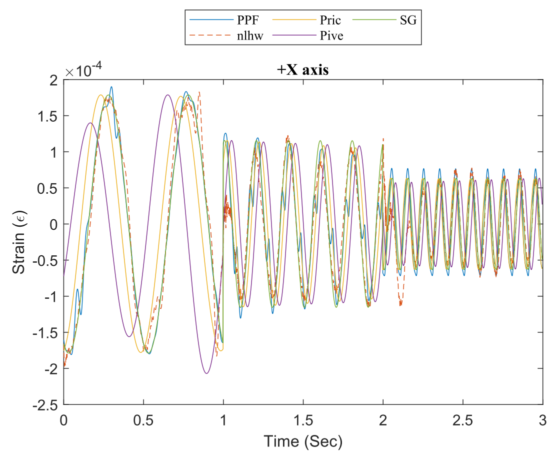

(b) X axis loading (+ X beam)

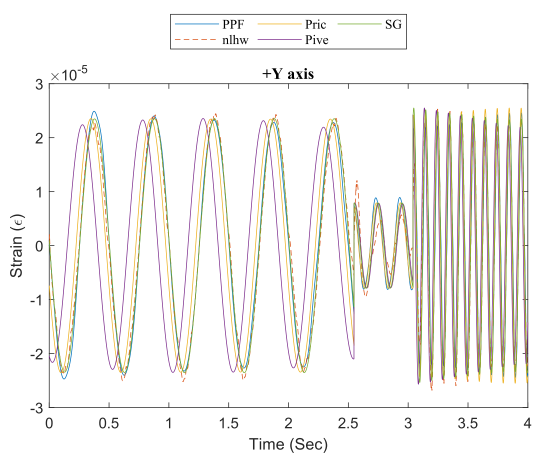

(c) Z axis loading (+ Y beam)

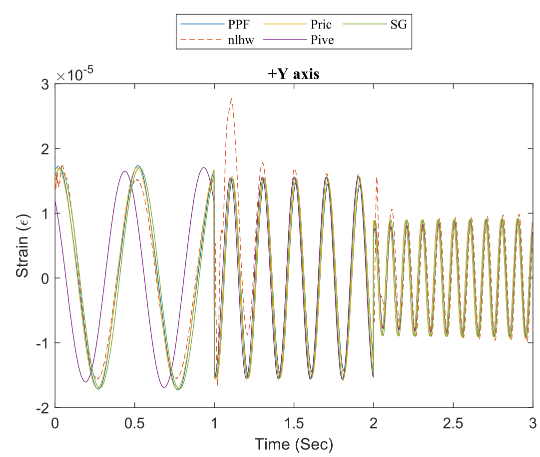

(d) X axis loading (+ Y beam)

Figure 8.26. The EPPF results at the +X and +Y beams.

Table 8.8. The nlhw models used at Z and X-loading strain estimation using the cascaded data.

Test	Zeros	Poles	Model	Nonlinearity
+X beam (z)	18	19	Hammerstein	sigmoidnet
+X beam (x)	18	19	Hammerstein	sigmoidnet
+Y beam (z)	18	19	Hammerstein	sigmoidnet
+Y beam (x)	19	20	linear	-

The EPPF's FISs produced the desired piezoelectric weights for the accompanying measurements taken at different frequencies. The output weights were retrieved to analyze the EPPF's performance for +X beam's strain fusion and +Y beam's strain fusion, as shown in Fig. 8.27. The EPPF's generated weights were classified into three groups of different weight values. For the +X beam, three distinct weight values in both loading tests resulted in the higher MFs. By contrast, two similar weight groups with very close magnitudes were observed in the +Y beam's tests, as shown in Fig 8.27c, d. Consequently, only a small number of MFs were needed, as shown in Fig 8.25c, d.

The DPPF and EPPF methods' RMSE compared to nlhw models

The RMSE was used to assess the proposed fusion method's performance and to compare the results of the method with the actual estimate of the nonlinear models. For the DPPF method, the RMSE of the fused strain was calculated for the Z-axis and X-axis loading scenarios under the excitation frequencies of 2 Hz, 5 Hz, 10 Hz, and 100 Hz, as shown in Fig. 8.28. The DPPF method achieved the smallest RMSE under most of the loading directions and frequencies compared to the nlhw models. However, higher RMSEs were associated with -Y beams at 2 Hz and 10 HZ excitations of Z-axis loading experiments. This is because an issue with the -Y-axis strain gauge circuit, which had a circuit element failure or external noise, affecting the actual strain measurement. When an actual strain measurement was used to generate and tune the fusion FISs, the cumulative DPPF fused strains' RMSEs at all frequencies were lower than the nlhw models' RMSE by 34 %, 33 %, and 13 % at the +X-axis, -X-axis, and +Y-axis beams, respectively. On the other hand, the nlhw models estimated the strain at a 60.8 % lower cumulative RMSE compared to the proposed fusion

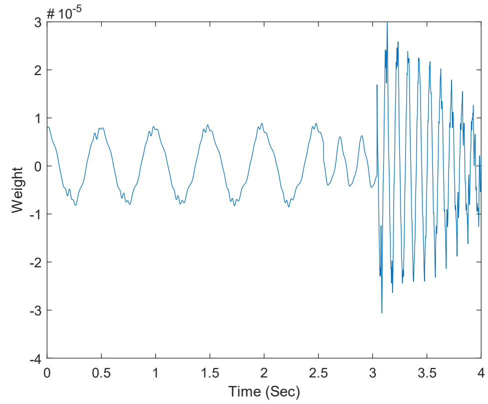

(a) Z axis loading (+ X beam)

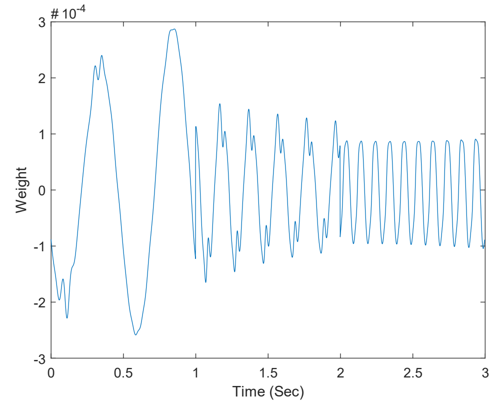

(b) X axis loading (+ X beam)

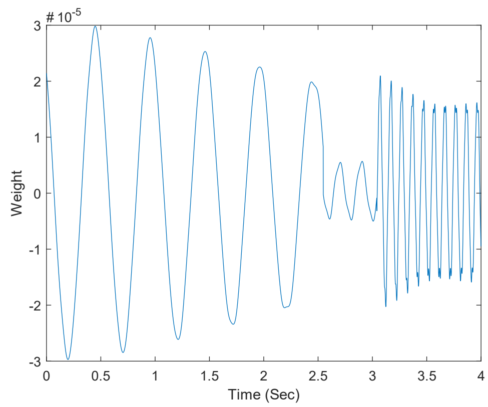

(c) Z axis loading (+ Y beam)

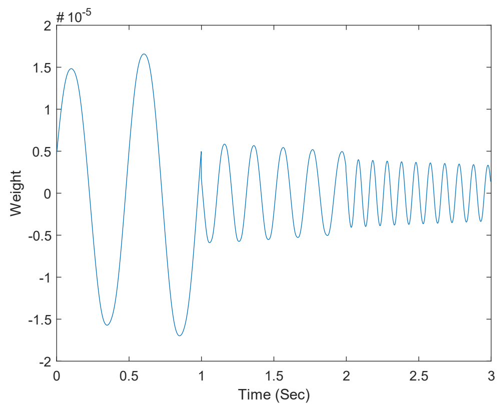

(d) X axis loading (+ Y beam)

Figure 8.27. The generated EPPF's piezoelectric weight for +X and +Y beams.

method because of the influence of the noise strain gauge at that beam. Relatively smaller RMSEs were perceived in the Z-axis loading test under the excitations of 2 Hz and 100 Hz. The DPPF achieved the smallest RMSE of 1E-10 at the +Y-axis beam under the vibration of 100 Hz.

Similarly, the EPPF method was analyzed and compared with nlhw models' strain estimate using the RMSE for the +X-axis beam and + Y-axis beam under the two loading experiments, as shown in Fig. 8.29. The EPPF fused strains' RMSE was lower during these

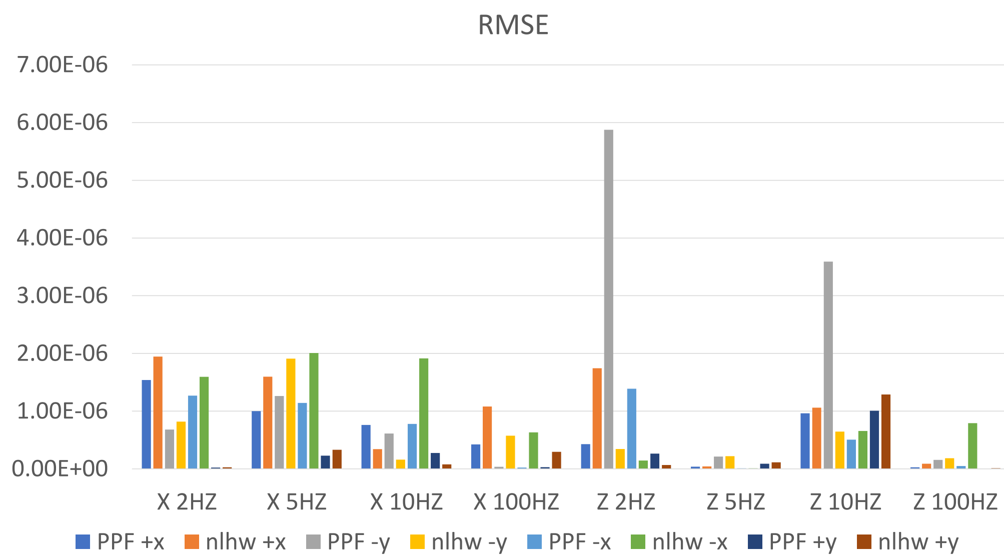

Figure 8.28. The PPF and nlhw's models' RMSE.

testing scenarios except for the X-axis loading test of the +X-axis beam. This was due to the higher number of MFs needed to achieve more accurate fusion at that condition. The EPPF fused strain measurement achieved approximately 15 % less accumulative RMSE compared to the nonlinear model. Relatively higher RMSEs were observed in the +X-axis beam under X-direction vibration due to the need for higher-order nlhw models and EPPF's MFs.

These results prove the capability of the proposed DPPF and EPPF to fuse the MWCNT/PVDF strain sensors' piezoresistive and piezoelectric measurements. The fused strains successfully matched the actual strains with minimal RMSEs at the 3D force sensor's structure using both the piezoresistive and piezoelectric characteristics. In the DPPF method, a single FIS merged the measurements based on their sensitivity at a specific operating frequency, while single FISs were used to perform the fusion at a range of operating frequencies using the EPPF method.

8.4.2 The Direct PPF method and [39] fusion method

The Direct PPF's (DPPF) performance was tested and compared with the proposed fusion method in [39]. The experimental data from the reference [39] were used to generate and validate the Direct PPF method. The proposed method was implemented to develop

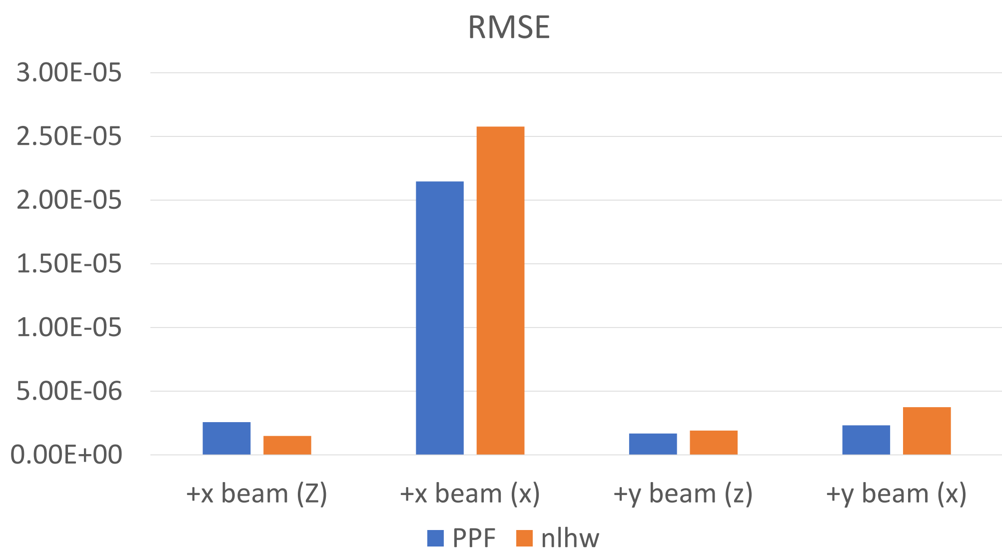

Figure 8.29. The EPPF and nlhw's models' RMSE.

the PPF's FISs at 0.1 Hz, 1 Hz, and 100 Hz. At the 0.1 Hz and 1 Hz frequencies, the piezoresistive sensor was assigned the total weight of one, while the piezoelectric sensor's weights were computed using Equation 5.3. At 100 Hz, the piezoelectric sensor's weights were computed using Equation 5.2 and the weight of one was assigned to the piezoresistive sensors. The input MFs, output MF's linear equation's constants, and rules were generated and tuned using the piezoresistive measurement, the piezoelectric measurement, and the computed desired weight. For each FIS, a set of rules was generated to relate the FIS's input and output MFs, as shown in Table 8.5. Each resulting input membership function consisted of multiple data sets or clusters, where the number of MFs equaled the number of clusters and rules. The same rules table was generated for each FIS except for the number of rules (n), which depended on the MF's number.The developed FISs' input MFs for the three operating frequencies were retrieved, as shown in Fig. 8.30.

The PPF's FISs at the 0.1 Hz and the 100 Hz frequencies required two MFs to fuse the piezoresistive and piezoelectric measurements, where the cluster influence range of one was assigned at each operating frequency, as shown in Fig. 8.30a,c. On the other hand, the PPF's inputs cluster influence range for the 1 Hz frequency was 0.5, resulting in five inputs MFs for piezoresistive and piezoelectric strains input variables, as shown in Fig. 8.30b. The

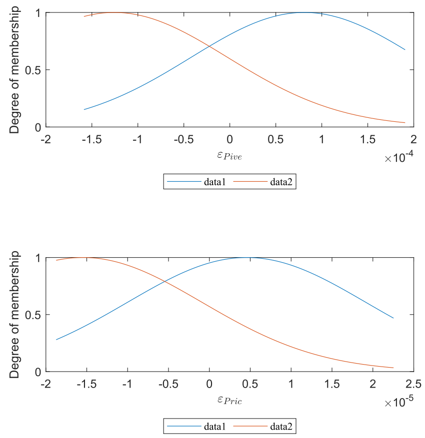

(a) 0.1 Hz

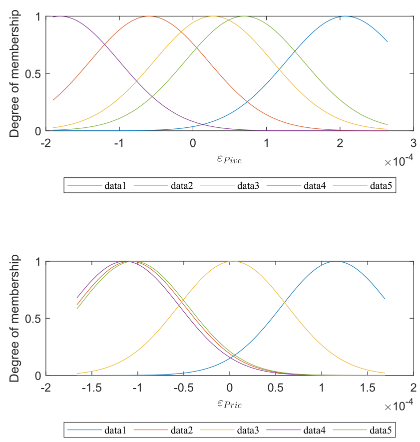

(b) 1 Hz

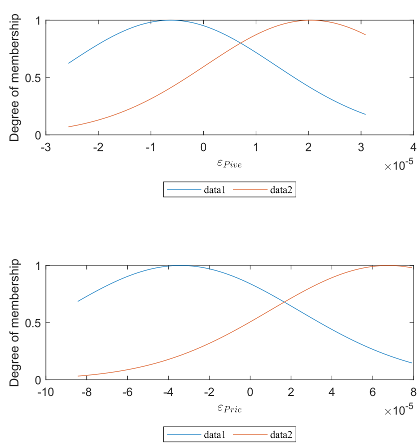

(c) 100 Hz

Figure 8.30. Input MFs of the PPF's FISs at 0.1, 1, and 100 Hz frequencies

output MFs and rule output levels were generated using the same procedure that was used for the 3D force sensor fusion. The rest of the output MFs at each beam and frequency followed the same process. Refer to Table A.4 in the Appendix for the MFs' rule output level's coefficients.

The direct FISs had the piezoresistive and piezoelectric strain measurement as inputs and either the piezoresistive or piezoelectric characteristic output, depending on the operating frequency. The PPF's fused strains were calculated using Equation 5.4 and the FIS's output weight. The PPF's fused strains were retrieved and compared with the measurements' characteristics, reference strain gauge measurements, and the [39] fused strain, as shown in Fig. 8.31. The PPF's fused strains agreed closely with the reference strain gauges compared to the [39] fused strain.

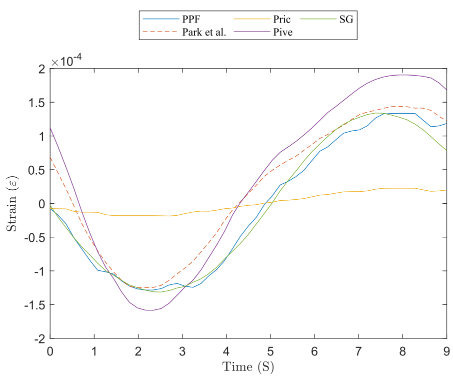

(a) 0.1 Hz

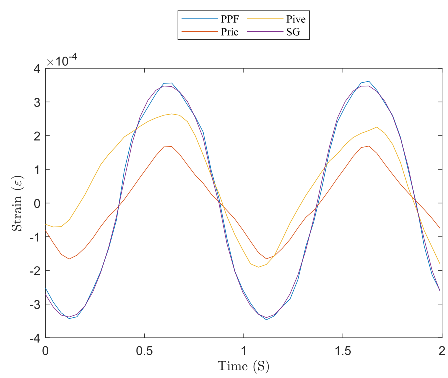

(b) 1 Hz

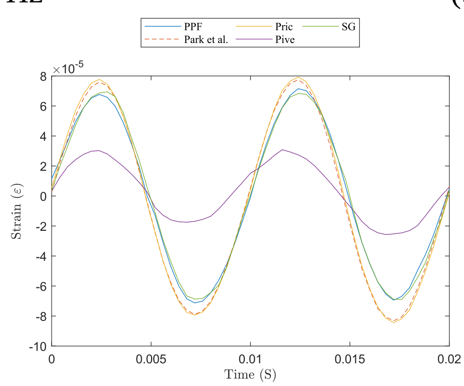

(c) 100 Hz

Figure 8.31. The Direct PPF results compared to the [39] fusion method at 0.1, 1, and 100 Hz.

The PPF's FISs generated the desired piezoelectric and piezoresistive weights at the three operating frequencies. The FIS's output weights were recorded to analyze the PPF's performance, as shown in Fig. 8.32. Relatively higher piezoelectric weights were assigned at 1 Hz for the fused strain because of the higher number of piezoresistive and piezoelectric sensor errors at this frequency. Conversely, the generated weights at 0.1 Hz and 100 Hz were relatively lower due to the high accuracy of piezoresistive and piezoelectric sensors at these frequencies, respectively.

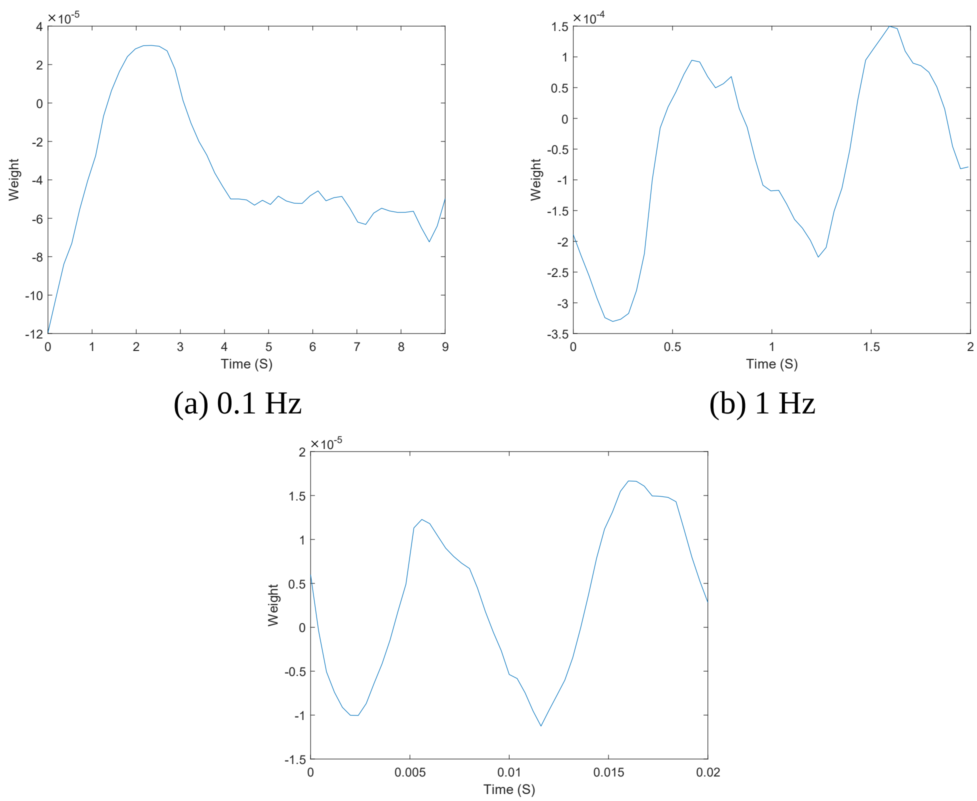

(a) 0.1 Hz (b) 1 Hz

(c) 100 Hz

Figure 8.32. The PPF's FISs output weights at 0.1, 1, and 100 Hz.

The direct PPF method was analyzed and compared with the reference [39] fusion method using the RMSE at 0.1 Hz, 1 Hz, and 100 Hz., as shown in Fig. 8.33. The direct PPF fused strain's RMSE was lower compared to the [39] fused strain values at 0.1 Hz and 100 HZ. The piezoresistive and piezoelectric measurements at 1 Hz were not fused in the study [39], while a similar RMSE of 1.1E-5 was achieved by the PPF method at 0.1 Hz and 2 Hz.

The developed direct PPF's FISs, based on the subtractive clustering method, successfully fused the piezoresistive and piezoelectric measurements and produced accurately fused strain measurements with minimum RMSE values.

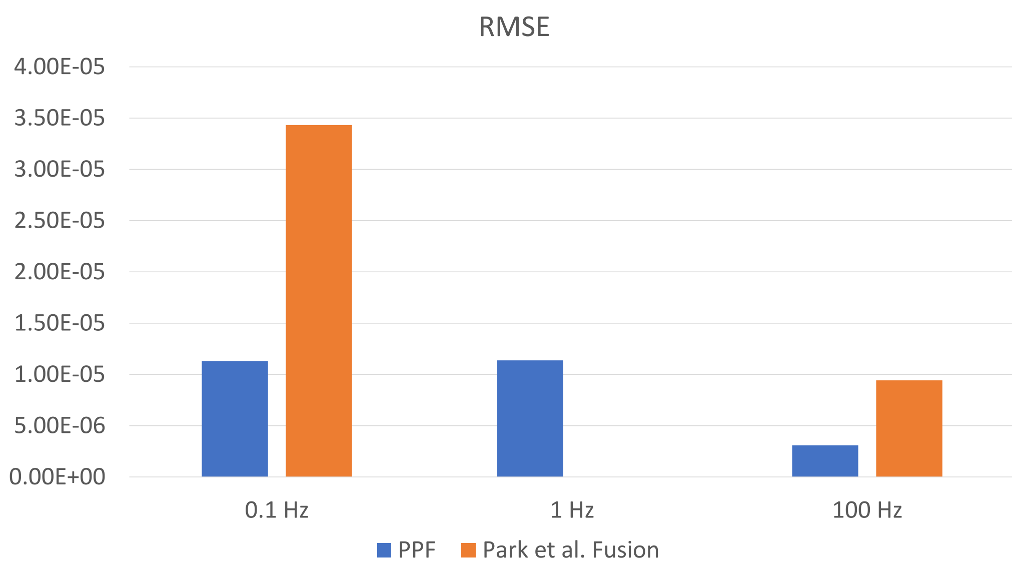

Figure 8.33. The Direct PPF's RMSE compared to the [39] fusion method.

8.4.3 The DPPF method for Triangle and Square waves

The DPPF method was tested and validated for different strain signal types using presumed generated data. Triangle and Square signal waves were assigned for the piezoresistive sensor, the piezoelectric sensor, and the strain gauges, as shown in Fig. 8.34. For these tests, the actual strain signals with a magnitude of one were measured by the strain gauges at an excitation of 1 Hz. The piezoresistive strain measurements were assumed to be more accurate at this frequency. As a result, a magnitude of 0.8 was assigned for piezoresistive strain measurements for both tests. At the same time, the piezoelectric strain measurements were less accurate, with an assigned magnitude of 0.2.

The DPPF's FISs were produced and the developed FISs' input MFs for both tests were retrieved as shown in Fig. 8.35. The cluster influence ranges were assigned to be one for FISs' inputs and outputs. The piezoresistive signals were given the total weight of one, while the piezoelectric sensors' weights were computed using Equation 5.3. A total number of two MFs

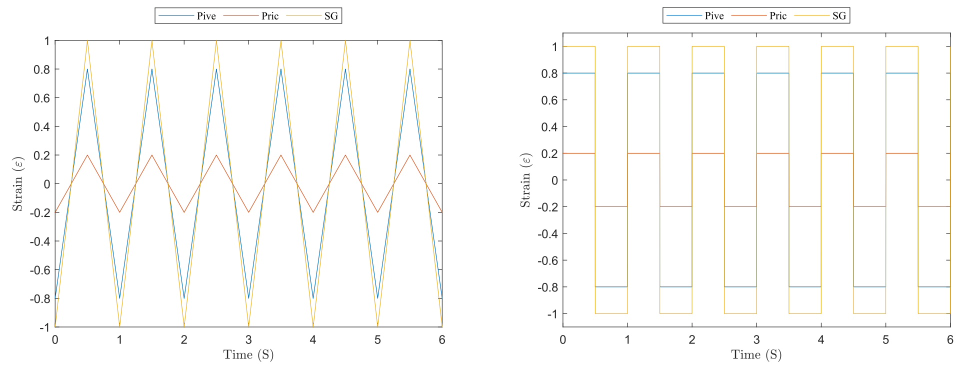

(a) Triangle wave signal (b) Square wave

Figure 8.34. Original signals at (a) Triangle wave signal and (b) Square wave tests at 1 Hz.

for the input variables were generated using the DPPF method, where the cluster influence ranges were assigned to be one for both the input and output variables. Each FIS applied the same set of two rules from Table 8.5. The outputs MFs for each test were generated using the same process discussed in the previous sections. Refer to Table A.5 in the Appendix for the MFs' rule output level's coefficients. For the Square wave signal test, a zero-order Sugeno system was utilized, where the coefficients $a_{\mathrm{i}} = b_{\mathrm{i}} = 0$ at the output level (Z_{i}) in Equation 8.1. On the other hand, the b_{i} coefficient became a zero in the Triangle wave test's output MFs, which resulted in a linear equation for the Z_{i} in terms of only the piezoresistive signal. However, the piezoelectric signals still contributed to firing strength (W) in the FIS.

Using the Simulink model, the generated DPPF's FISs were test and analyzed in both scenarios. The generated DPPF's fused strain, strain measurements, and reference strain gauges were retrieved, as shown in Fig. 8.36. The DPPF method had merged both measurements and achieved accurately fused strain measurements using the Triangle wave and Square wave signals. The RMSEs were calculated for both tests. A very low RMSE of 1.7E-15 was noted for the Square wave fusion. The DPPF's RMSE for the Square strain measurement fusion test was 0.0017.

The DPPF's FISs produced the desired piezoelectric weights for the proposed Triangle and Square strain measurements tests. The output weights were retrieved for the DPPF's performance analysis at both fusion tests, as shown in Fig. 8.37. The generated weights

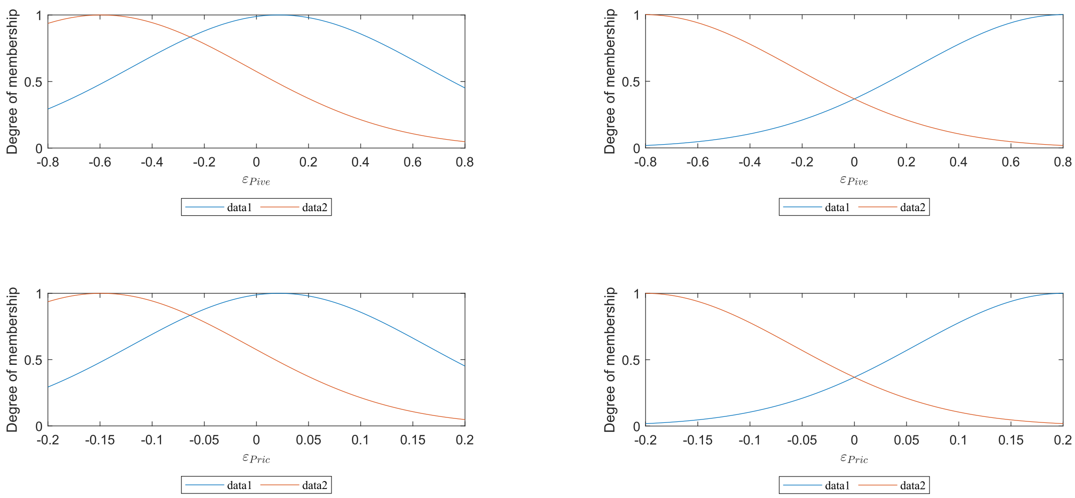

(a) Triangle wave signal (b) Square wave

Figure 8.35. Input MFs at (a) Triangle wave signal and (b) Square wave fusion tests.

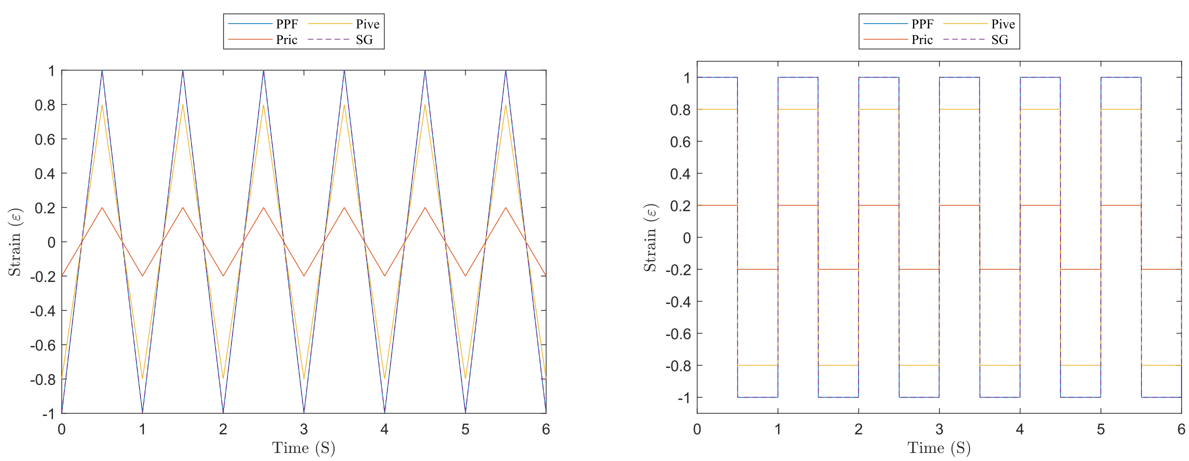

(a) Triangle wave signal (b) Square wave signal

Figure 8.36. The DPPF results at (a) Triangle wave signal and (b) Square wave tests at 1 Hz.

inherited the original signal shape and similar weights' ranges were observed in both tests because of the similarities in the original signals' magnitudes. Thus, the DPPF has proven its effectiveness for fusing piezoresistive and piezoelectric measurements with different types of signals.

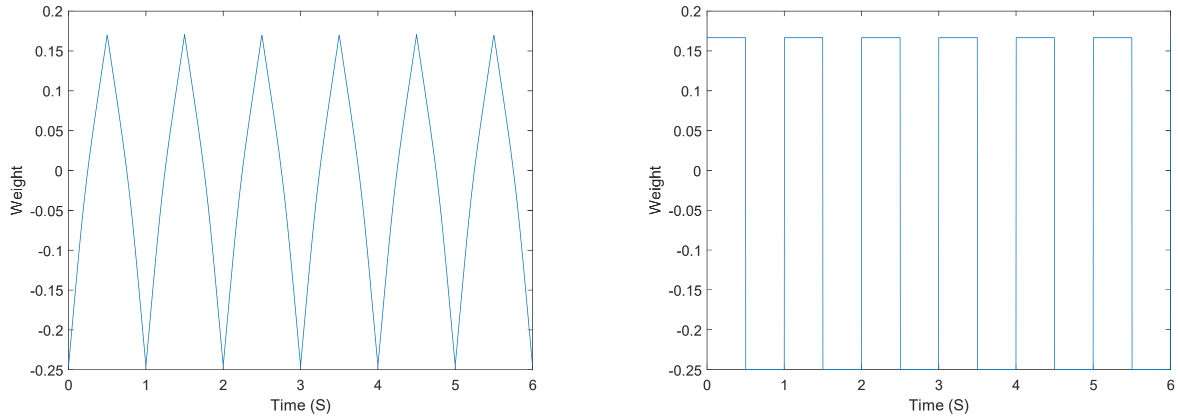

(a) Triangle wave signal (b) Square wave

Figure 8.37. The DPPF FISs' generated piezoelectric weights at (a) Triangle wave signal and (b) Square fusion tests.

8.5 Piezoresistive/Piezoelectric modeling results

The PVDF/MWCNT strain sensor's piezoresistive and piezoelectric characteristics were modeled and analyzed using Matlab Simulink. The circuit elements' values were fitted with output piezoresistive and piezoelectric measurements given the actual strains, taken from a strain gauge, of the experimental data found in the literature [39]. In addition, a preliminary robustness analysis of these models is presented in the following subsection.

8.5.1 Piezoresistive modeling results

The piezoresistive model was constructed using R-C circuits implemented in three circuit stages: 1) Wheatstone bridge, 2) differential amplifier, and 3) low pass filter. The model was tested at the frequencies of 0.1 Hz, 1 Hz, 100 Hz, and 1000 Hz, as shown in Figure 8.38. At

0.1 Hz, the model captured both peaks while mismatching the strain measurements between peaks. That is, the piezoresistive measurement at that frequency in the reference data was not uniform. At 0.1 Hz, the model attained more accuracy and better tracking after the first peak. There was a phase shift of + 0.0005 sec, between the piezoresistive model output and piezoresistive signal [39] at 100 Hz, which was corrected. The piezoresistive model carried out measurements with high accuracy. The piezoresistive strain sensor, as documented in the literature [39], was not measuring at 1000 Hz; however, a similar model output was achieved with an overshoot at the beginning of the measurement.

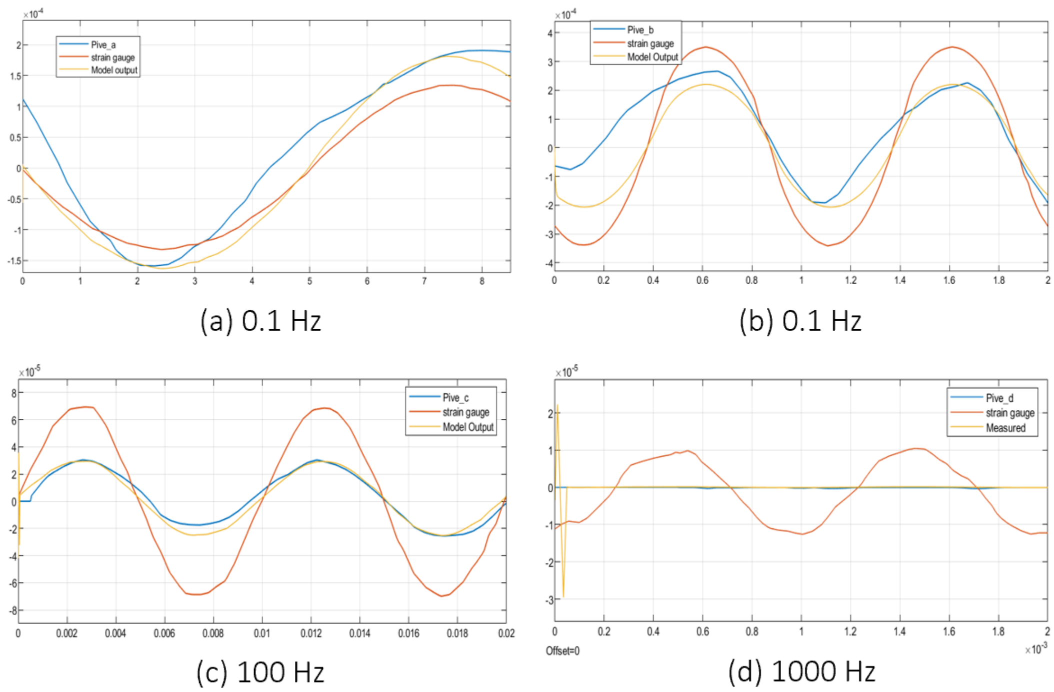

Figure 8.38. Piezoresistive model output under different excitation frequencies

The low pass filter and the calibration factor (CF) were fitted to match the piezoresistive measurements, as shown in Figure 8.39. Logarithmic Scala was used for the frequency axes to show the relationships between the frequencies and the models' parameters. The CF of -0.0025 was fitted for the piezoresistive measurement model at 0.1 Hz, while a similar CF of -0.002237 was indicated for the model under other excitation frequencies. The resistance (R2) of the model was 2.9070×10^{3} Ohm and constant among the tested frequencies. The capacitance C1 of 1×10^{-6}F and 1×10^{-12}F were fitted for the two smallest and largest frequencies, respectively. The resistance (R1) increased when the excitation frequency increased. An average resistance of 31.7 Ω was indicated by the model at the frequencies of 0.1 Hz, 1 Hz, and 100 Hz. On the other hand, the piezoresistive model, which operates at 1000 Hz, has a renaissance of 3 kΩ. The increase in the R1 at 1000 Hz might be because 1000 Hz is significantly larger than the other frequencies used in the modeling process.

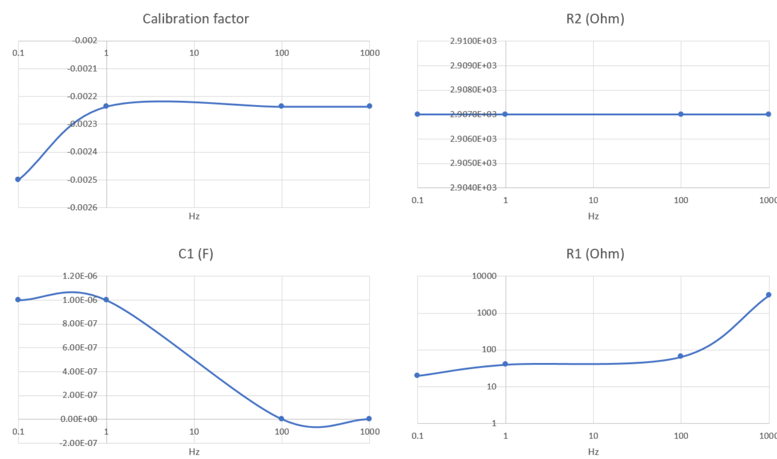

Figure 8.39. Piezoresistive model parameters fitted under different excitation frequencies

A preliminary robustness analysis of the piezoresistive model was conducted under different excitation strain frequencies, as shown in Figure 8.40. A Band-Limited White Noise block in Matlab Simulink was used to test the model for robustness. Noises of varying powers were randomly introduced and the time for which the noise was introduced matched the simulation's sample time. The preliminary results from the piezoresistive model showed good robustness and the model still tracked the strain measurements.

8.5.2 Piezoelectric modeling results

The piezoelectric model was constructed and a charge amplifier was used. The model was tested at the frequencies of 0.1 Hz, 1 Hz, 100 Hz, and 1000 Hz, as shown in Figure 8.41. At 0.1 Hz, the piezoelectric signal [39] was almost zero; however, there were small peaks which were captured by the piezoelectric model. The model tracked the piezoelectric signal [39] changes at 0.1 Hz with an acceptable degree of accuracy. However, the model did not

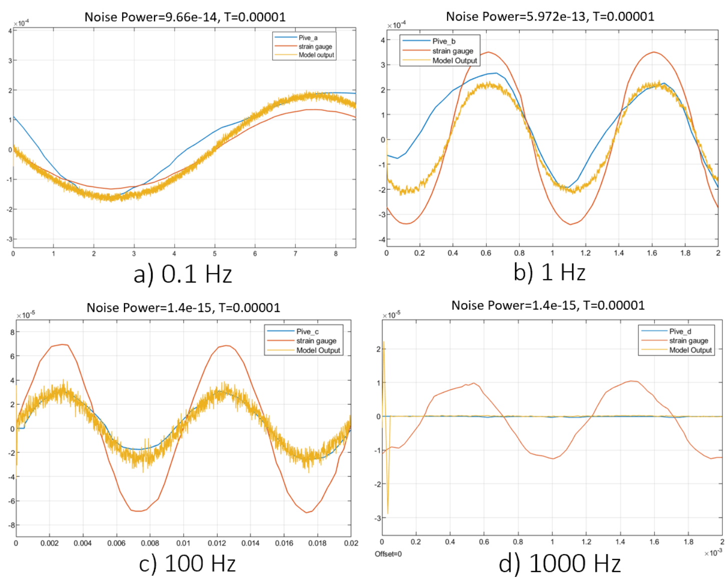

Figure 8.40. Piezoresistive model output under different excitation frequencies and noises.

capture the strain peaks because the piezoelectric signal [39] did not have uniform peaks. In the simulation, the model and the piezoelectric signal matched closely at 100 Hz and they also closely agreed at 1000 Hz.

The model's calibration factor (CF) was fitted under four frequencies, as shown in Figure 8.42. Relatively close CFs were fitted at 0.1 Hz and 1 Hz with an average of $3{\times}10^{-6}$. The highest CF value was recorded at 100 Hz with CF a of $1.65{\times}10^{-5}$. The CF decreased at 1000 Hz to $1.2{\times}10^{-5}$. The PVDF/MWCNT's frequency response might have influenced the fitted CF parameter and further harmonic analysis will be conducted in the future to confirm this relationship.

A preliminary robustness analysis of the piezoelectric model was conducted under different excitation strain frequencies, as shown in Figure 8.43. Similar to the piezoresistive model analysis, a Band-Limited White Noise block in Matlab simulink was used test the model for robustness. Different noise's power were introduced randomly and the noise sample's times were matched to the simulations' sample time. Preliminary results show good robustness for the piezoelectric model and that the model still tracked the strain's measurements.

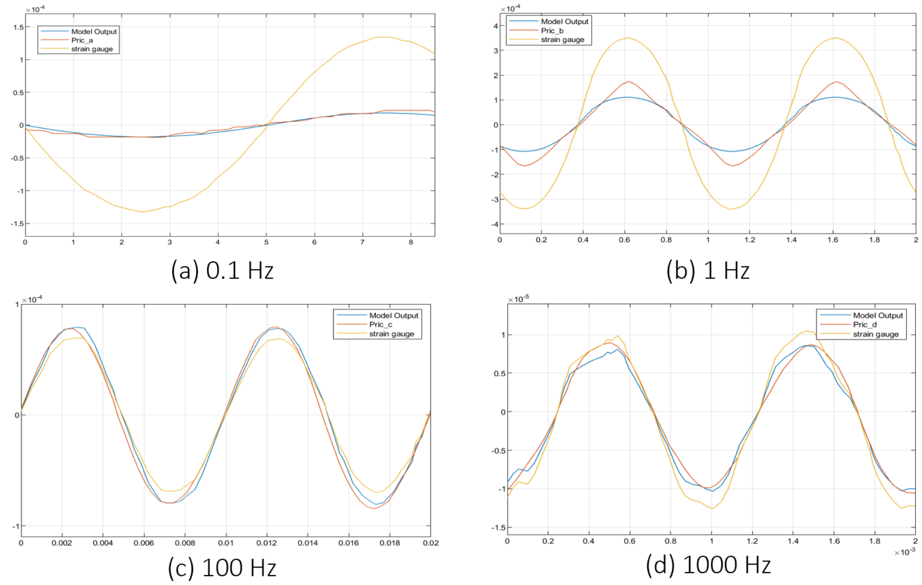

Figure 8.41. Piezoelectric model output under different excitation frequencies.

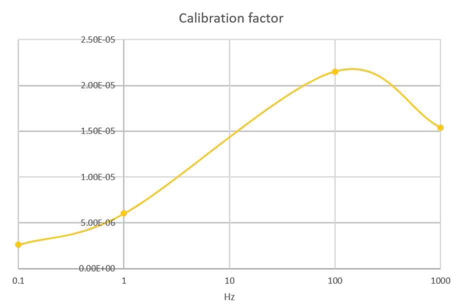

Figure 8.42. Piezoelectric model's calibration factor fitted under different excitation frequencies.

8.6 3D force sensor simulation results

The 3D force sensor captured the three-dimensional force components which were compared to the 3D force/torque used to quantify the 3D force and torque components. The current study focuses on designing a 3D force measurement and did not take torque or moments into consideration. The elastic structures of the five selected configurations were simulated using ANSYS Workbench [96]. The structure's total deformations, equivalent stresses, and normal elastic strains at sensor placements were retrieved after the simulations were conducted. The total deformations, equivalent stresses, and safety factors for each of

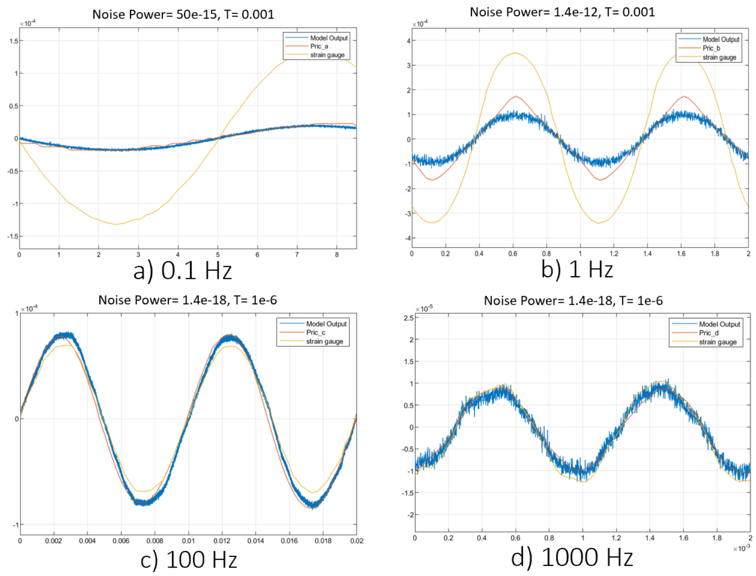

Figure 8.43. Piezoelectric model output under different excitation frequencies and noises.

the bioinspired 3D force sensors on the lateral (X-axis) and perpendicular (Y-axis) force scenarios were investigated. Forces were applied gradually up to the maximum values of 60 N and 100 N in the direction of X and Y axes, respectively.

The lowest and highest deformation values that measured on the 3D sensors‘ elastic structures, were DFx= 59.58 $\times 10^{-6}$ mm and DFy= 3.7792$\times 10^{-3}$ mm in the tree branches and cross designs, respectively, as shown in Figure 8.44. The implemented branches increased the stiffness about four times on the X-axis and 32 times on the Y-axis; this decreased the structure's flexibility in both directions. The smallest deformation deference between the force scenarios was found in the tree branch structure with 54.05 $\times 10^{-6}$ mm difference, this structure was the most isotropic structure among all of the structures. To investigate the safety of these designs, maximum equivalent stresses were obtained on each structure, as shown in Figure 8.45 . The safety factor was defined as the ratio between the yield stress of the material to the maximum equivalent stress on each 3D force sensor's structure. All designs were safe under these force ranges and could be overloaded with a minimum of three times the assigned force ranges of Fx = 60 N and Fy = 100 N. The smallest safety factors were observed for the cross design under Y-axis loading conditions which was expected because of the low stiffness in that direction. Similarly, the spider design had the smallest safety factor in X-direction compared to the other designs. The tree branch design was observed to be the safest structure compared to all the other designs, This safety was achieved because the split branch design was used on each beam instead of the cross design.

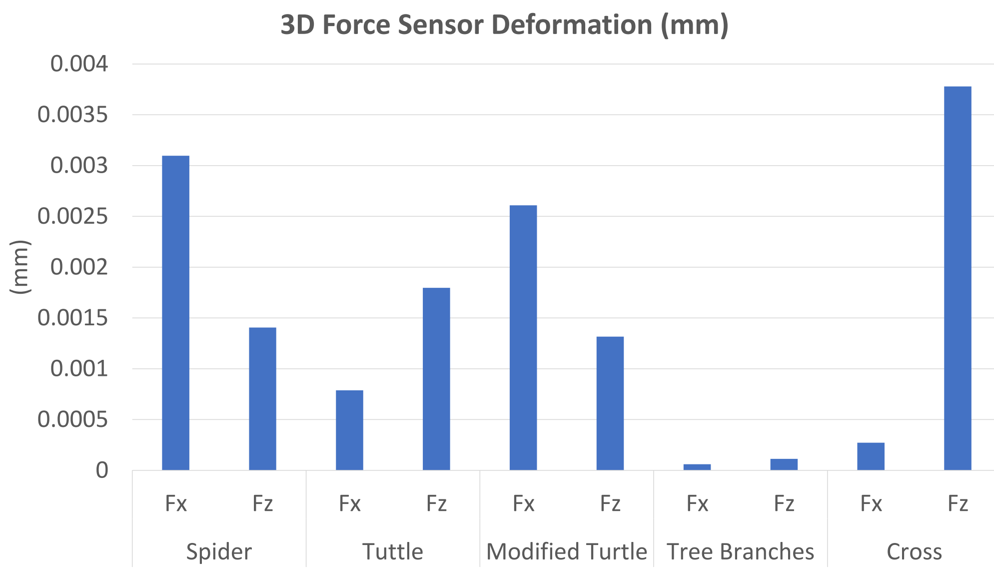

Figure 8.44. Maximum total deformation of the proposed designs.

In terms of measuring strain at the assigned sensing placements, the average normal elastic strain was used to analyze the strain measurements. The sensors' normal elastic strains were acquired from the surface splits or selected sensing elements' placements on the bio-inspired 3D force sensors. In the case of applying 60 N in the X-direction, the average normal elastic strain values and their contours were retrieved at each of the assigned sensing elements' placements for each design, as shown in Figure 8.46.

The positive value of average normal elastic strain at any sensing element indicated that surface was mostly in tension and a negative value of average normal elastic strain at any sensing element indicated that the surface was mostly in compression. The turtle, tree branches, and cross designs showed a perfect decoupling of sensing elements along the Z-axis from the applied force on X direction. The spider and modified turtle exhibited higher sensitivity of 3×10^{-8} and 2×10^{-8} (mm/mm)/N on the Z-axis sensing elements, respectively. The 3D force sensors indicated symmetrical average normal elastic strain responses while forces were applied in the X-direction.

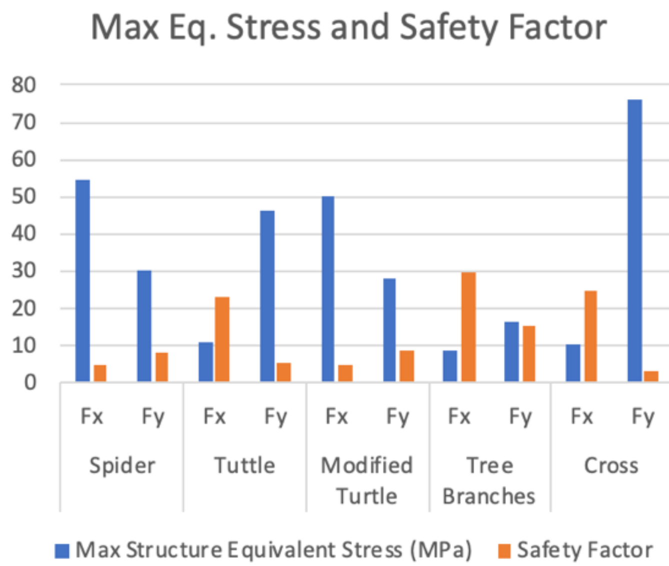

Figure 8.45. Maximum total deformation of the proposed designs.

In terms of sensing element placements, it is desirable to have the elements attached to the areas which are subject to either tension or compression strains. As shown in the Figure 8.46 contour plots, this was achieved in the turtle, tree branch, and cross designs. The turtle design exhibited distinct and significant stress distribution in Z-direction under X-direction loading. On the other hand, the modified turtle design's sensor placements were based on the stress variations along the beams.

In the case of applying 100 N along the Y-direction (normal), the average normal elastic strains and their strain mapping were retrieved at each assigned sensing element's placement, as shown in Figure 8.47. The sensing elements underwent a compressive normal elastic strain in all models except for the spider model's and tree branch model's 3D sensors. For each 3D force sensor, the assigned sensing elements were exposed to the same amount and sign of the average normal strain; this was due to the symmetrical structures and sensing elements' distributions. The implemented branches inverted the compression on the sensing elements' areas in the cross design into tension in the tree branches design, as shown in Figure 8.47 d, e.

As shown in Figure 8.47, the contour plots for the average normal elastic strain were utilized to assist with the sensor placements. The tree branches design exhibited the most

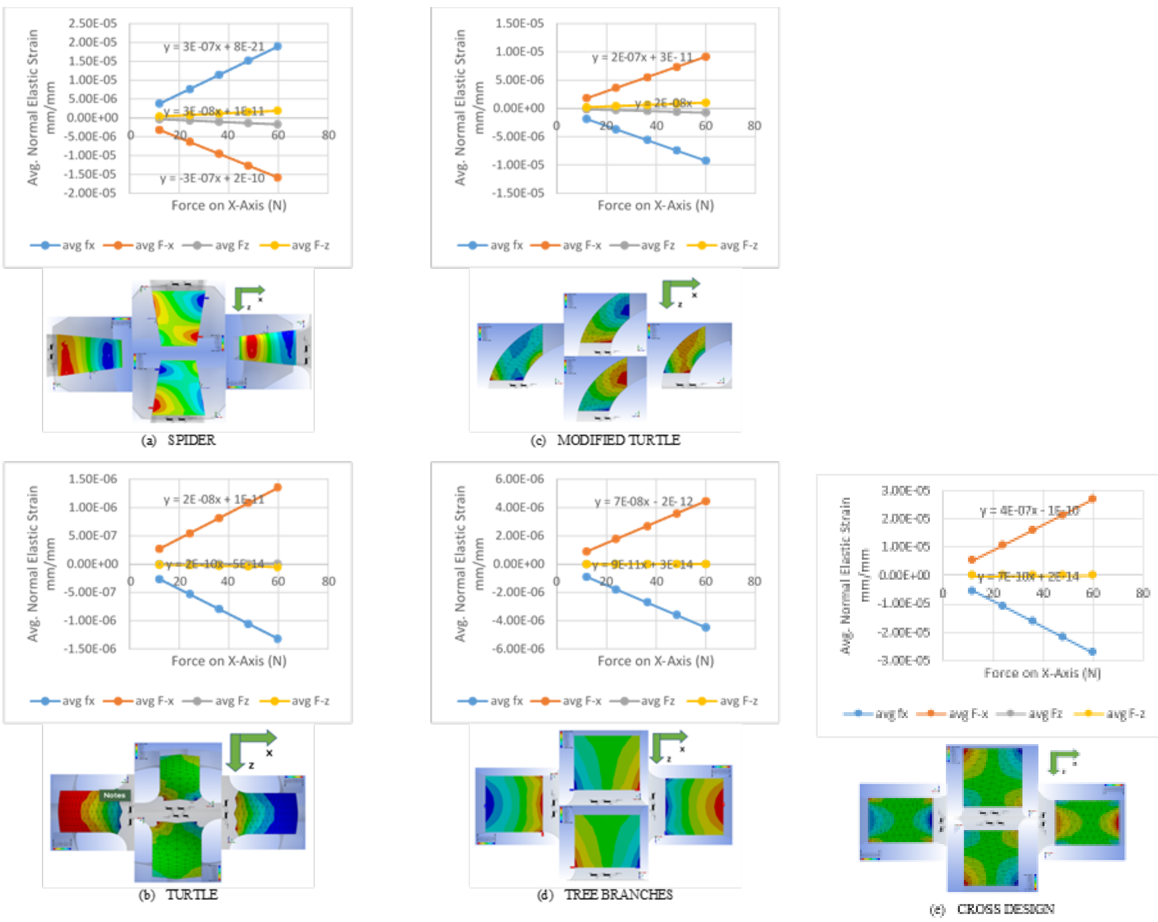

Figure 8.46. Bio-inspired 3D force sensor average normal elastic strain and its contours at sensing elements placements under FX= 60 N for: (a) Spider, (b) Turtle, (c) Modified turtle, (d) Tree branches, (e) Cross designs.

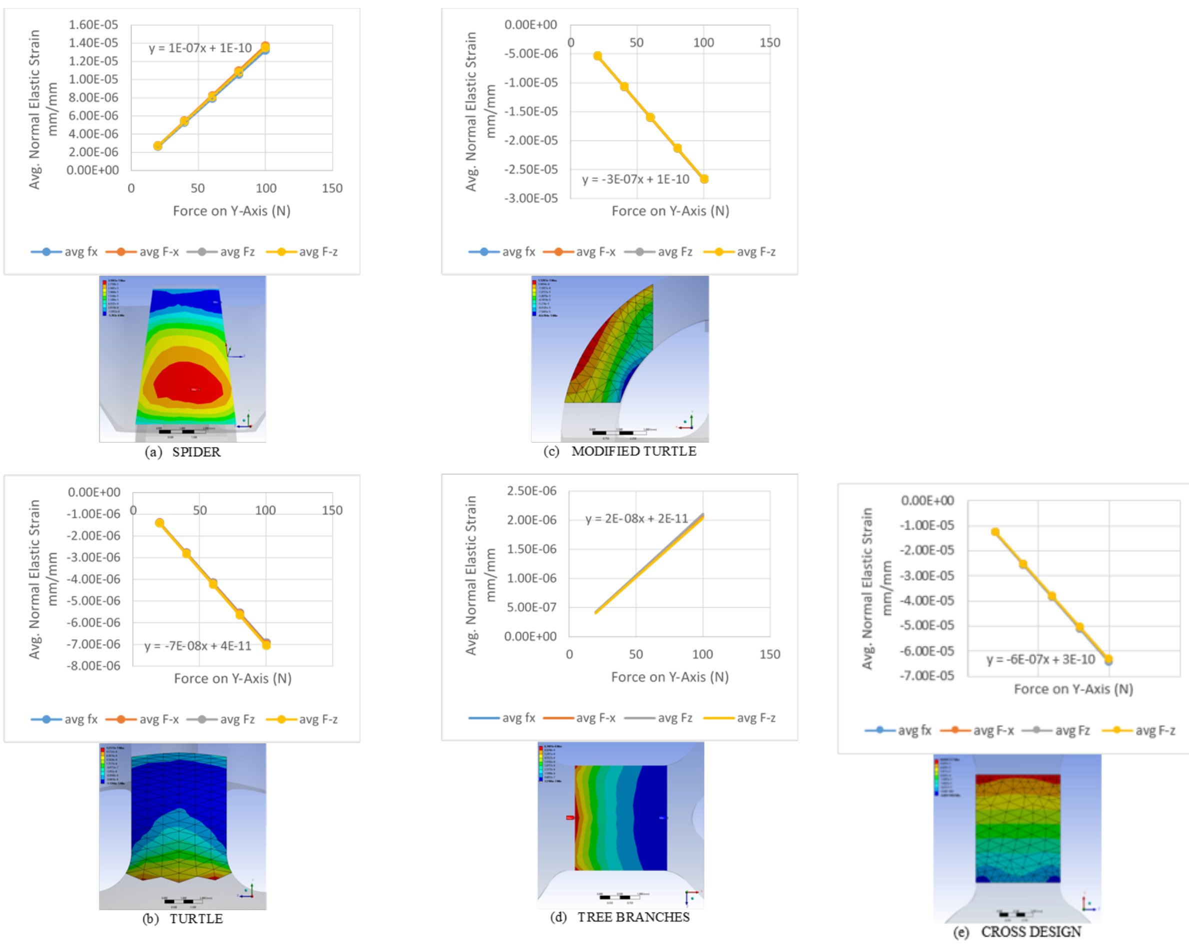

Figure 8.47. Bio-inspired 3D force sensor average normal elastic strain and its contours at sensing elements placements under fy= 100 N (Normal) for: (a) Spider, (b) Turtle, (c) Modified turtle, (d) Tree branches, (e) Cross designs.

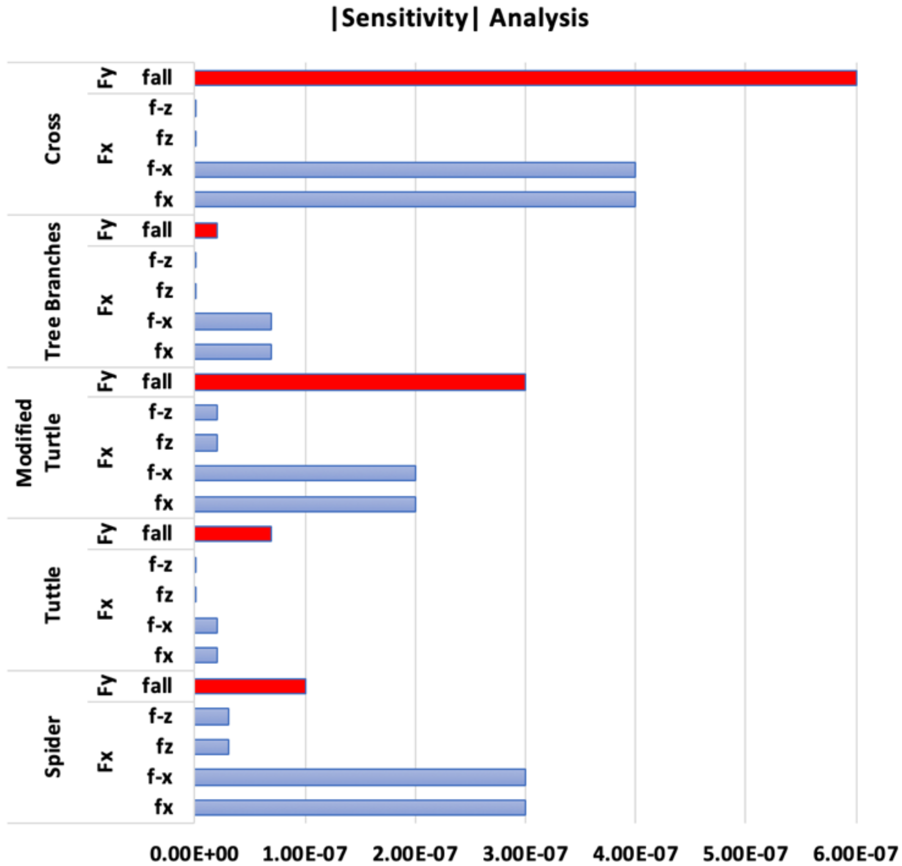

Figure 8.48. The bio-inspired 3D force sensor sensitivity analysis.

homogeneous strain distribution, compared to other designs. The modified turtles design's sensor indicated good strain distribution, but the outer side placement of the sensing element experienced a strain sign variation which should be avoided. Similarly, for more accurate results, the upper side placement of the sensing element in the spider design should be avoided. On the other hand, the cross and the turtle sensing element placements indicated variations in strain distribution along the sensing element.

The absolute average strain sensitivities of the 3D force sensors were obtained from the responses from each force condition, as shown in Fig. 8.48. The absolute sensitivity at the sensing elements' areas of the cross design achieved the highest sensitivity compared to the other designs when Fy (normal) was applied. In addition, the minimum sensitivity accrued along X-axis was recorded when the force Fx was applied along the X-axis in the turtle design.

The sensing elements on the Z-axis indicated almost zero cross-coupling in the case of Fx in the cross, tree branches, and turtle designs. On the other hand, the spider and modified turtle designs were sensitive in the Z-direction when Fx was applied. In the tree branches design, the branches decreased the strain sensitivity to both force conditions, because of the increased stiffness which then decreased the structural flexibility. However, there was a smaller sensitivity difference between the two force conditions in comparison to the cross design. Similarly, the turtle design had approximately the same sensitivity difference except it was more sensitive to the loading in the Y-direction, Fy, because of the implemented turtle shell structure. It is clear that the modified turtle design significantly improved the sensing sensitivity for the case of the Fy loading condition, but that resulted in coupling the sensing elements on the Z-axis for the force applied on the X-axis. In addition, the spider design was more sensitive to both loading conditions than the turtle design; however, coupling was present.

The tree branches' structural configuration was selected for the 3D force structure for different reasons. The tree branch configuration attained the most negligible coupling between the strain measurements at the sensing placement areas for the X-axis loading test compared to other proposed designs and the cross design. Also, the turtle and tree branches achieved the lowest sensitivity difference of 5E-8 between the normal and lateral direction loading scenarios compared to the other design. However, the turtle design had a lower sensitivity for strain on the X-axis beams under the same direction of loading. On the other hand, an average sensitivity difference of 1.67E-7 was obtained by the spider, modified turtle, and cross design. The tree branches design had the highest safety factor for all loading directions and allowed the structure's configuration to withstand higher force ranges. In terms of sensor fabrication, a simple two-dimension fabrication process can be utilized to fabricate the cross and tree branches design, such as a conversion machine, water jet, and laser cutting process. In comparison, other designs might need advanced machine technologies such as computer numerical control (CNC). Flat sensing element placements were presented for the tree branches and cross design, facilitating bonding the sensing elements to the structures' beams. Consequently, it can be concluded that the tree branch configuration offered the best combination of factor of safety, sensitivity, structure fabrication, sensing placements, and structural integrity as required for a 3D force sensor.

9. CONCLUSIONS AND FUTURE WORK

9.1 Conclusions

The *in situ* MWCNT/PVDF nanocomposite strain sensor has the potential to capture both low and high-frequency dynamic strain measurements using both piezoresistive and piezoelectric measurements, respectively. However, the strain sensor's band frequencies are limited to either piezoresistive or piezoelectric, depending on the design or measurements criteria. In this study, a novel PPF method is proposed to effectively combine piezoresistive and piezoelectric characteristics to capture wide frequency MWCNT/PVDF strain measurements in real-time. The proposed piezoresistive/piezoelectric fusion (PPF), based on a fuzzy logic inference engine and error measurements, was introduced to combine piezoresistive and piezoelectric sensor data.

Different techniques and methods were used to generate the PPF's FISs, including the optimization method, data clustering, and a fuzzy Type-2 system using MATLAB. The FCM clustering, subtractive clustering, and Type-2 FISs were investigated and compared with another fusion method already documented in the literature. At a low-frequency (0.1 Hz and 1 Hz) strain measurement, the piezoresistive sensor was assigned a full weight while the PPF's FISs estimated the necessary piezoelectric contribution weight. Both weights as well as the piezoresistive and piezoelectric strain measurements, were used to enhance the frequency range and increase the measurements' accuracy using the developed fusion equation. The subtractive cluster and Type-2 FIS-based PPF fused both measurements while attaining a high accuracy and relatively small RMSEs. However, Type-2 FIS-based PPF reduced the subtractive clustering's RMSE by approximately 4% at the frequency 0.1 Hz by including the footprint of uncertainty. Both methods fused the measurement using Sugeno FIS using only two MFs for input/output variables. With the maximum number of MFs of three, the optimization-based FIS utilized the particle swarm optimization and pattern search algorithms to learn and tune the FIS's parameters, respectively. Additionally, the optimization-based FISs's RMSE was approximately 60.47 % less than the FCM-based FISs among the three frequencies. Sugeno-based PPF indicated a high accuracy compared to the Mamdani FIS because of the Sugeno's ability to work with dynamic nonlinear systems efficiently. The developed PPF was verified with experimental data at the different dynamic frequencies presented in [39]. The results correlated very well with the actual strain measurements and significantly reduced the measurement error of both characteristics. The proposed fusion approach thus has the potential for other measurement methods influenced by input frequency or a similar environment.

In this study, a number of bio-inspired structures were investigated for three-dimensional force sensing. These structures included a spider, turtle, modified turtle, and tree branch. Finite Element Analysis of these structures was performed to determine the optimal sensitivity, the safety factor, and structural integrity of each model. The FEA results were compared with the traditional cross-shape design used for 3D force sensors. It was observed that the tree branch configuration provided the smallest coupling between the forces in the Y-direction, as did the cross-shape and turtle configurations. While the cross-shape retained a high sensitivity, it exhibited the smallest factor of safety in the Y-direction. The tree branch configuration, on the other hand, showed the highest safety factor in this direction. Overall, it can be concluded that the tree branch configuration offered the best combination of safety factor, sensitivity, sensing placements, and structural integrity as is required for a 3D force sensor.

The *in situ* 0.1 wt.% and 2 wt.% MWCNT/PVDF strain sensors were fabricated using a spray-coating process and were chosen for piezoelectric and piezoresistive strain measurements, respectively. The sensitivity and accuracy of each characteristic were investigated using a supported beam under different excitation frequencies. The MWCNT/PVDF sensor was found to be sensitive at frequencies lower than 100 Hz and more noise was observed at high frequencies. At the same time, the piezoelectric characteristic was found to be sensitive and to contain less noise at the higher frequencies, which in this study were 100 Hz and 1000 Hz. However, the piezoelectric measurement was found not to be sensitive at very low frequencies. The tree branch 3D force sensor was introduced and used the fabricated strain sensing elements on its structure. The piezoresistive and piezoelectric films were attached at each beam, and reference strain gauges were attached on the opposite side for comparison and fusion method generation. Wheatstone bridge circuits were used for the piezoresistive sensors and strain gauges. By contrast, a charge amplifier circuit was used for the piezoelectric characteristic measurements. The 3D force sensor was excited at different operating frequencies in the Z-axis and the X-axis directions, while the 3D force sensor was assumed to perform similarly in the X-direction and the Y-direction. The piezoresistive, piezoelectric, and strain gauge measurements were used to generate the proposed DPPF and EPPF using the Fuzzy Logic and Global Optimization Toolboxes in MATLAB. These methods utilized the Sugeno FIS and the subtractive clustering technique to fuse the piezoresistive and piezoelectric measurements. Fusion was successfully performed at a single operating frequency using a single FIS in the DPPF method, while the EPPF method accurately fused both characteristics at the range of operating frequencies using a unique FIS. The method achieved a lower RMSE value compared to different nlhw actual strain estimation models. The DPPF method was tested and validated for different strain signal types using presumed Triangle and Square signal waves data. The DPPF has proven its effectiveness in fusing piezoresistive and piezoelectric measurements with different types of signals. The findings of this study indicate that the MWCNT/ PVDF measurement characteristics can be fused using the DPPF and EPPF methods and achieve a wide band strain sensor. However, the proposed fusion method is not restricted to strain measurements, but rather has the potential to fuse different measurements for a single phenomenon, where particular limitations restrict measurement characteristics.

9.2 Future work

The PPF method could be applied to different sensing applications where frequency or other phenomena influencing their performance could be improved through this fusion-based estimate. Then, these limitations could be overcome. Our results are promising and should be validated using an investigation with a greater number of frequencies on the MWCNT/ PVDF piezoresistive and piezoelectric characteristics. The proposed fusion methods have not been tested at all the bioinspired structures and a future study should verify the PPF based methods for these structures. A stack of piezoresistive and piezoelectric layers will result in a smaller sensing attachment space required to improve the NC sensor structure. We believe that our research will serve as a base for future studies on NC measurement fusion. A Printed

Circuit Board (PCB) circuits constriction for piezoresistive and piezoelectric NC sensors with short traces would minimize impedance mismatching that is suspected for the measurements' phase shifts. Future work should concentrate on constructing the 3D force sensor based on electrospun MWCNT/PVDF films using static or drum collector and enhancing the strain sensing sensitivity. Further research should also focus on producing a uniform or homogeneous NC film using an automated spray-coating machine. On a wider level, research is also needed to investigate the compatibility of the sensing elements and the proposed fusion method with the 3D force/torque sensor, which takes torque and moments into consideration. The current 3D force sensor can be miniaturized for different Instrument Assisted Soft Tissue Mobilization (IASTM) devices by scaling down the bio-inspired structure configuration and fabricating smaller MWCNT/PVDF sensing elements.

Future studies should investigate the natural frequencies of the proposed 3D force sensor's structures and how these frequencies influence on the measurement's bandwidth. Also, geometric optimization method could be used in order to create a bio-inspired structural design with higher sensitivity, lower force coupling, and a wider force range. In addition, the structure's natural frequencies under different loading directions could be optimized for the desired measurement bandwidth using such a technique. Increasing the structure's natural frequencies can be achieved by increasing the stiffness or decreasing the mass of the overall structural design and the four elastic beams. Increasing the natural frequencies of such structures will produce a higher measurement bandwidth but less strain sensitivity because of the lower deflection that could be achieved in the structure.

To mass-produce the proposed 3D force sensor, the PPF's FIS needs to be generated and tuned using a dataset. In many machine learning applications, better performance and more representation can be achieved by using more data, especially for complex problems. A minimum number of 500-1000 data points is used in some problems [127], while average problems utilize 10,000 - 100,000 data points and complex problems will use 100,000 - 1,000,000 data points. Also, approximately ten times the problem dimension's data points were used for the general machine learning problem. Because of the high dimensionality of the problems, the PPF based methods might need 100,000 - 1,000,000 data points to be generated to tune their FISs.

REFERENCES

[1] Z. Lou, H. Han, M. Zhou, J. Wan, Q. Sun, X. Zhou, and N. Gu, "Fabrication of magnetic conjugation clusters via intermolecular assembling for ultrasensitive surface plasmon resonance (spr) detection in a wide range of concentrations," *Analytical chemistry*, vol. 89, no. 24, pp. 13 472–13 479, 2017.

[2] J. Zhou, T. Yang, J. Chen, C. Wang, H. Zhang, and Y. Shao, "Two-dimensional nanomaterial-based plasmonic sensing applications: Advances and challenges," *Coordination Chemistry Reviews*, vol. 410, p. 213 218, 2020.

[3] C. Gau, H. Ko, and H. Chen, "Piezoresistive characteristics of mwnt nanocomposites and fabrication as a polymer pressure sensor," *Nanotechnology*, vol. 20, no. 18, p. 185 503, 2009.

[4] S. Borovik and Y. Sekisov, "Single-coil eddy current sensors and their application for monitoring the dangerous states of gas-turbine engines," *Sensors*, vol. 20, no. 7, p. 2107, 2020.

[5] C.-Y. Lin, Y.-Y. Fang, C.-W. Lin, J. J. Tunney, and K.-C. Ho, "Fabrication of nox gas sensors using in2o3–zno composite films," *Sensors and Actuators B: Chemical*, vol. 146, no. 1, pp. 28–34, 2010.

[6] B. Mitchell, J. Koo, I. Iordachita, P. Kazanzides, A. Kapoor, J. Handa, G. Hager, and R. Taylor, "Development and application of a new steady-hand manipulator for retinal surgery," in *Proceedings 2007 IEEE International Conference on Robotics and Automation*, IEEE, 2007, pp. 623–629.

[7] Y. Kakinuma, K. Igarashi, S. Katsura, and T. Aoyama, "Development of 5-axis polishing machine capable of simultaneous trajectory, posture, and force control," *CIRP Annals*, vol. 62, no. 1, pp. 379–382, 2013.

[8] R. A. Brookhuis, T. S. Lammerink, R. J. Wiegerink, M. J. de Boer, and M. C. Elwenspoek, "3d force sensor for biomechanical applications," *Sensors and actuators A: physical*, vol. 182, pp. 28–33, 2012.

[9] D. Trivedi, C. D. Rahn, W. M. Kier, and I. D. Walker, "Soft robotics: Biological inspiration, state of the art, and future research," *Applied bionics and biomechanics*, vol. 5, no. 3, pp. 99–117, 2008.

[10] P. Estevez, J. Bank, M. Porta, J. Wei, P. Sarro, M. Tichem, and U. Staufer, "6 dof force and torque sensor for micro-manipulation applications," *Sensors and Actuators A: Physical*, vol. 186, pp. 86–93, 2012.

[11] A. M. Alotaibi, S. Anwar, M. Terry Loghmani, and S. Chien, “Force sensing for an instrument-assisted soft tissue manipulation device,” *Journal of Medical Devices*, vol. 11, no. 3, 2017.

[12] D. Lee, H. P. Hong, M. J. Lee, C. W. Park, and N. K. Min, “A prototype high sensitivity load cell using single walled carbon nanotube strain gauges,” *Sensors and Actuators A: Physical*, vol. 180, pp. 120–126, 2012.

[13] S. Iijima, “Helical microtubules of graphitic carbon,” *nature*, vol. 354, no. 6348, pp. 56–58, 1991.

[14] J.-P. Salvetat, J.-M. Bonard, N. Thomson, A. Kulik, L. Forro, W. Benoit, and L. Zuppiroli, “Mechanical properties of carbon nanotubes,” *Applied Physics A*, vol. 69, no. 3, pp. 255–260, 1999.

[15] R. S. Ruoff and D. C. Lorents, “Mechanical and thermal properties of carbon nanotubes,” *carbon*, vol. 33, no. 7, pp. 925–930, 1995.

[16] K. Yoshino, H. Kajii, H. Araki, T. Sonoda, H. Take, and S. Lee, “Electrical and optical properties of conducting polymer-fullerene and conducting polymer-carbon nanotube composites,” *Fullerene science and technology*, vol. 7, no. 4, pp. 695–711, 1999.

[17] Z. Yao, C. L. Kane, and C. Dekker, “High-field electrical transport in single-wall carbon nanotubes,” *Physical Review Letters*, vol. 84, no. 13, p. 2941, 2000.

[18] P. Kim, L. Shi, A. Majumdar, and P. L. McEuen, “Thermal transport measurements of individual multiwalled nanotubes,” *Physical review letters*, vol. 87, no. 21, p. 215 502, 2001.

[19] C. Yu, L. Shi, Z. Yao, D. Li, and A. Majumdar, “Thermal conductance and thermopower of an individual single-wall carbon nanotube,” *Nano letters*, vol. 5, no. 9, pp. 1842–1846, 2005.

[20] J. Sandler, J. Kirk, I. Kinloch, M. Shaffer, and A. Windle, “Ultra-low electrical percolation threshold in carbon-nanotube-epoxy composites,” *Polymer*, vol. 44, no. 19, pp. 5893–5899, 2003.

[21] K. Kalaitzidou, H. Fukushima, and L. T. Drzal, “A new compounding method for exfoliated graphite–polypropylene nanocomposites with enhanced flexural properties and lower percolation threshold,” *Composites Science and Technology*, vol. 67, no. 10, pp. 2045–2051, 2007.

[22] A. Celzard, E. McRae, C. Deleuze, M. Dufort, G. Furdin, and J. Marêché, "Critical concentration in percolating systems containing a high-aspect-ratio filler," *Physical Review B*, vol. 53, no. 10, p. 6209, 1996.

[23] S. H. Munson-McGee, "Estimation of the critical concentration in an anisotropic percolation network," *Physical Review B*, vol. 43, no. 4, p. 3331, 1991.

[24] I. Alig, P. Pötschke, D. Lellinger, T. Skipa, S. Pegel, G. R. Kasaliwal, and T. Villmow, "Establishment, morphology and properties of carbon nanotube networks in polymer melts," *Polymer*, vol. 53, no. 1, pp. 4–28, 2012.

[25] M. Moniruzzaman and K. I. Winey, "Polymer nanocomposites containing carbon nanotubes," *Macromolecules*, vol. 39, no. 16, pp. 5194–5205, 2006.

[26] N. Hu, H. Fukunaga, S. Atobe, Y. Liu, J. Li, *et al.*, "Piezoresistive strain sensors made from carbon nanotubes based polymer nanocomposites," *Sensors*, vol. 11, no. 11, pp. 10 691–10 723, 2011.

[27] B. Hu, N. Hu, Y. Li, K. Akagi, W. Yuan, T. Watanabe, and Y. Cai, "Multi-scale numerical simulations on piezoresistivity of cnt/polymer nanocomposites," *Nanoscale research letters*, vol. 7, no. 1, p. 402, 2012.

[28] C. Li, E. T. Thostenson, and T.-W. Chou, "Dominant role of tunneling resistance in the electrical conductivity of carbon nanotube–based composites," *Applied Physics Letters*, vol. 91, no. 22, p. 223 114, 2007.

[29] A. V. Shirinov and W. K. Schomburg, "Pressure sensor from a pvdf film," *Sensors and actuators A: Physical*, vol. 142, no. 1, pp. 48–55, 2008.

[30] R. Pérez, M. Král, and H. Bleuler, "Study of polyvinylidene fluoride (pvdf) based bimorph actuators for laser scanning actuation at khz frequency range," *Sensors and Actuators A: Physical*, vol. 183, pp. 84–94, 2012.

[31] V. Rathod, D. R. Mahapatra, A. Jain, and A. Gayathri, "Characterization of a large-area pvdf thin film for electro-mechanical and ultrasonic sensing applications," *Sensors and Actuators A: Physical*, vol. 163, no. 1, pp. 164–171, 2010.

[32] A. Glück, W. Halder, G. Lindner, H. Müller, and P. Weindler, "Pvdf-excited resonance sensors for gas flow and humidity measurements," *Sensors and Actuators B: Chemical*, vol. 19, no. 1-3, pp. 554–557, 1994.

[33] J. Xu, M. J. Dapino, D. Gallego-Perez, and D. Hansford, "Microphone based on polyvinylidene fluoride (pvdf) micro-pillars and patterned electrodes," *Sensors and Actuators A: Physical*, vol. 153, no. 1, pp. 24–32, 2009.

[34] C. J. Sielmann, J. R. Busch, B. Stoeber, and K. Walus, “Inkjet printed all-polymer flexural plate wave sensors,” *IEEE Sensors Journal*, vol. 13, no. 10, pp. 4005–4013, 2013.

[35] D. Vatansever, R. Hadimani, T. Shah, and E. Siores, “An investigation of energy harvesting from renewable sources with pvdf and pzt,” *Smart Materials and Structures*, vol. 20, no. 5, p. 055 019, 2011.

[36] A. Ramaratnam and N. Jalili, “Reinforcement of piezoelectric polymers with carbon nanotubes: Pathway to next-generation sensors,” *Journal of Intelligent Material Systems and Structures*, vol. 17, no. 3, pp. 199–208, 2006.

[37] J. Kim, K. J. Loh, and J. P. Lynch, “Piezoelectric polymeric thin films tuned by carbon nanotube fillers,” in *Sensors and Smart Structures Technologies for Civil, Mechanical, and Aerospace Systems 2008*, International Society for Optics and Photonics, vol. 6932, 2008, p. 693 232.

[38] J. S. Lee, G. H. Kim, W. N. Kim, K. H. Oh, H. T. Kim, S. S. Hwang, and S. M. Hong, “Crystal structure and ferroelectric properties of poly (vinylidene fluoride)-carbon nano tube nanocomposite film,” *Molecular Crystals and Liquid Crystals*, vol. 491, no. 1, pp. 247–254, 2008.

[39] M. Sanati, A. Sandwell, H. Mostaghimi, and S. S. Park, “Development of nanocomposite-based strain sensor with piezoelectric and piezoresistive properties,” *Sensors*, vol. 18, no. 11, p. 3789, 2018.

[40] D. He, L. Weiting, R. Yuan, F. Xin, and C. STEFANINI, “Preliminary study on piezoresistive and piezoelectric properties of a double-layer soft material for tactile sensing,” *Materials Science*, vol. 21, no. 2, pp. 238–243, 2015.

[41] S. Khan, W. Dang, L. Lorenzelli, and R. Dahiya, “Flexible pressure sensors based on screen-printed p (vdf-trfe) and p (vdf-trfe)/mwcnts,” *IEEE Transactions on Semiconductor Manufacturing*, vol. 28, no. 4, pp. 486–493, 2015.

[42] A. M. Alotaibi, S. Anwar, M. T. Loghmani, and S. Chien, “Development of a force sensing instrument assisted soft tissue mobilization device,” in *ASME 2016 International Mechanical Engineering Congress and Exposition*, American Society of Mechanical Engineers Digital Collection, 2016.

[43] M.-K. Kang, S. Lee, and J.-H. Kim, “Shape optimization of a mechanically decoupled six-axis force/torque sensor,” *Sensors and Actuators A: Physical*, vol. 209, pp. 41–51, 2014.

[44] Y. Lu, L. Chen, P. Wang, B. Zhang, Y. Zhao, and B. Hu, “Statics and stiffness analysis of a novel six-component force/torque sensor with 3-rpps compliant parallel structure,” *Mechanism and Machine Theory*, vol. 62, pp. 99–111, 2013.

[45] Y. Hou, D. Zeng, J. Yao, K. Kang, L. Lu, and Y. Zhao, “Optimal design of a hyperstatic stewart platform-based force/torque sensor with genetic algorithms,” *Mechatronics*, vol. 19, no. 2, pp. 199–204, 2009.

[46] A. M. Alotaibi and S. Anwar, “Analysis of bio-inspired structures for 3d force sensing using virtual prototyping,” in *ASME International Mechanical Engineering Congress and Exposition*, American Society of Mechanical Engineers, vol. 59407, 2019, V003T04A074.

[47] H. S. Alam, D. Soetraprawata, *et al.*, “The structural design of six-axis force/torque sensor using virtual prototyping technique,” *Journal of Scientific Research and Reports*, pp. 120–131, 2015.

[48] S. Sareh, A. Jiang, A. Faragasso, Y. Noh, T. Nanayakkara, P. Dasgupta, L. D. Seneviratne, H. A. Wurdemann, and K. Althoefer, “Bio-inspired tactile sensor sleeve for surgical soft manipulators,” in *2014 IEEE International Conference on Robotics and Automation (ICRA)*, IEEE, 2014, pp. 1454–1459.

[49] Z. Zeng, M. Liu, H. Xu, Y. Liao, F. Duan, L.-m. Zhou, H. Jin, Z. Zhang, and Z. Su, “Ultra-broadband frequency responsive sensor based on lightweight and flexible carbon nanostructured polymeric nanocomposites,” *Carbon*, vol. 121, pp. 490–501, 2017.

[50] Y. Liao, F. Duan, H. Zhang, Y. Lu, Z. Zeng, M. Liu, H. Xu, C. Gao, L.-m. Zhou, H. Jin, *et al.*, “Ultrafast response of spray-on nanocomposite piezoresistive sensors to broadband ultrasound,” *Carbon*, vol. 143, pp. 743–751, 2019.

[51] C.-M. Wu, M.-H. Chou, and W.-Y. Zeng, “Piezoelectric response of aligned electrospun polyvinylidene fluoride/carbon nanotube nanofibrous membranes,” *Nanomaterials*, vol. 8, no. 6, p. 420, 2018.

[52] K. Ke, Y. Wang, K. Zhang, Y. Luo, W. Yang, B.-H. Xie, and M.-B. Yang, “Melt viscoelasticity, electrical conductivity, and crystallization of pvdf/mwcnt composites: Effect of the dispersion of mwcnts,” *Journal of Applied Polymer Science*, vol. 125, no. S1, E49–E57, 2012.

[53] M. Han, Y. C. Chan, W. Liu, S. Zhang, and H. Zhang, “Low frequency pvdf piezoelectric energy harvester with combined d31 and d33 operating modes,” in *The 8th Annual IEEE International Conference on Nano/Micro Engineered and Molecular Systems*, IEEE, 2013, pp. 440–443.

[54] E. Fontananova, M. Bahattab, S. Aljlil, M. Alowairdy, G. Rinaldi, D. Vuono, J. Nagy, E. Drioli, and G. Di Profio, “From hydrophobic to hydrophilic polyvinylidenefluoride (pvdf) membranes by gaining new insight into material’s properties,” *RSC Advances*, vol. 5, no. 69, pp. 56 219–56 231, 2015.

[55] D. Dhakras, V. Borkar, S. Ogale, and J. Jog, “Enhanced piezoresponse of electrospun pvdf mats with a touch of nickel chloride hexahydrate salt,” *Nanoscale*, vol. 4, no. 3, pp. 752–756, 2012.

[56] S. K. Mahadeva, J. Berring, K. Walus, and B. Stoeber, “Effect of poling time and grid voltage on phase transition and piezoelectricity of poly (vinyledene fluoride) thin films using corona poling,” *Journal of Physics D: Applied Physics*, vol. 46, no. 28, p. 285 305, 2013.

[57] V. Sencadas, R. Gregorio Jr, and S. Lanceros-Méndez, “α to β phase transformation and microestructural changes of pvdf films induced by uniaxial stretch,” *Journal of Macromolecular Science®*, vol. 48, no. 3, pp. 514–525, 2009.

[58] H. Ning, N. Hu, T. Kamata, J. Qiu, X. Han, L. Zhou, C. Chang, Y. Liu, L. Wu, H. Ji, *et al.*, “Improved piezoelectric properties of poly (vinylidene fluoride) nanocomposites containing multi-walled carbon nanotubes,” *Smart materials and structures*, vol. 22, no. 6, p. 065 011, 2013.

[59] P. Martins, A. Lopes, and S. Lanceros-Mendez, “Electroactive phases of poly (vinylidene fluoride): Determination, processing and applications,” *Progress in polymer science*, vol. 39, no. 4, pp. 683–706, 2014.

[60] R. K. Layek, S. Samanta, D. P. Chatterjee, and A. K. Nandi, “Physical and mechanical properties of poly (methyl methacrylate)-functionalized graphene/poly (vinylidine fluoride) nanocomposites: Piezoelectric β polymorph formation,” *Polymer*, vol. 51, no. 24, pp. 5846–5856, 2010.

[61] S. Park *et al.*, “Carbon nanotube reinforced polymeric nanocomposites for sensing and monitoring,” 2015.

[62] F. Lux, “Models proposed to explain the electrical conductivity of mixtures made of conductive and insulating materials,” *Journal of materials science*, vol. 28, no. 2, pp. 285–301, 1993.

[63] S. Frankland, V. Harik, G. Odegard, D. Brenner, and T. Gates, “The stress–strain behavior of polymer–nanotube composites from molecular dynamics simulation,” *Composites Science and Technology*, vol. 63, no. 11, pp. 1655–1661, 2003.

[64] G. M. Odegard, T. Gates, K. Wise, C. Park, and E. Siochi, “Constitutive modeling of nanotube–reinforced polymer composites,” *Composites science and technology*, vol. 63, no. 11, pp. 1671–1687, 2003.

[65] C. Li and T.-W. Chou, “Multiscale modeling of carbon nanotube reinforced polymer composites,” *Journal of nanoscience and nanotechnology*, vol. 3, no. 5, pp. 423–430, 2003.

[66] R. Hill, “Elastic properties of reinforced solids: Some theoretical principles,” *Journal of the Mechanics and Physics of Solids*, vol. 11, no. 5, pp. 357–372, 1963.

[67] F. Fisher, R. Bradshaw, and L. C. Brinson, “Fiber waviness in nanotube-reinforced polymer composites—i: Modulus predictions using effective nanotube properties,” *Composites Science and Technology*, vol. 63, no. 11, pp. 1689–1703, 2003.

[68] D.-L. Shi, X.-Q. Feng, Y. Y. Huang, K.-C. Hwang, and H. Gao, “The effect of nanotube waviness and agglomeration on the elastic property of carbon nanotube-reinforced composites,” *J. Eng. Mater. Technol.*, vol. 126, no. 3, pp. 250–257, 2004.

[69] R. G. Ghanem and P. D. Spanos, “Stochastic finite element method: Response statistics,” in *Stochastic finite elements: a spectral approach*, Springer, 1991, pp. 101–119.

[70] L. Graham and S. Baxter, “Simulation of local material properties based on moving-window gmc,” *Probabilistic Engineering Mechanics*, vol. 16, no. 4, pp. 295–305, 2001.

[71] C. Li and T.-W. Chou, “Electrical conductivities of composites with aligned carbon nanotubes,” *Journal of nanoscience and nanotechnology*, vol. 9, no. 4, pp. 2518–2524, 2009.

[72] M. Taya, W. Kim, and K. Ono, “Piezoresistivity of a short fiber/elastomer matrix composite,” *Mechanics of materials*, vol. 28, no. 1-4, pp. 53–59, 1998.

[73] N. Hu, Y. Karube, C. Yan, Z. Masuda, and H. Fukunaga, “Tunneling effect in a polymer/carbon nanotube nanocomposite strain sensor,” *Acta Materialia*, vol. 56, no. 13, pp. 2929–2936, 2008.

[74] A. Sanli, A. Benchirouf, C. Muller, and O. Kanoun, “Piezoresistive characterization of multi-walled carbon nanotube-epoxy based flexible strain sensitive films by impedance spectroscopy,” *Composites Science and Technology*, vol. 122, pp. 18–26, 2016.

[75] E. Garcıa-Macıas, A. Downey, A. D’Alessandro, R. Castro-Triguero, S. Laflamme, and F. Ubertini, “Enhanced lumped circuit model for smart nanocomposite cement-based sensors under dynamic compressive loading conditions,” *Sensors and Actuators A: Physical*, vol. 260, pp. 45–57, 2017.

[76] S. Wansom, N. Kidner, L. Woo, and T. O. Mason, “Ac-impedance response of multi-walled carbon nanotube/cement composites,” *Cement and Concrete Composites*, vol. 28, no. 6, pp. 509–519, 2006.

[77] D. L. Hall and S. A. McMullen, *Mathematical techniques in multisensor data fusion*. Artech House, 2004.

[78] W. Elmenreich, “An introduction to sensor fusion,” *Vienna University of Technology, Austria*, vol. 502, pp. 1–28, 2002.

[79] Q. Jiang, X. Jin, G. Chen, S.-J. Lee, X. Cui, S. Yao, and L. Wu, “Two-scale decomposition-based multifocus image fusion framework combined with image morphology and fuzzy set theory,” *Information sciences*, vol. 541, pp. 442–474, 2020.

[80] K. Zhang, Y. Huang, X. Yuan, H. Ma, and C. Zhao, “Infrared and visible image fusion based on intuitionistic fuzzy sets,” *Infrared Physics & Technology*, vol. 105, p. 103 124, 2020.

[81] Y. Yang, Y. Que, S. Huang, and P. Lin, “Multimodal sensor medical image fusion based on type-2 fuzzy logic in nsct domain,” *IEEE Sensors Journal*, vol. 16, no. 10, pp. 3735–3745, 2016.

[82] P. Balasubramaniam and V. Ananthi, “Image fusion using intuitionistic fuzzy sets,” *Information Fusion*, vol. 20, pp. 21–30, 2014.

[83] D. Fraser and J. Potter, “The optimum linear smoother as a combination of two optimum linear filters,” *IEEE Transactions on automatic control*, vol. 14, no. 4, pp. 387–390, 1969.

[84] J. R. Raol, *Multi-sensor data fusion with MATLAB*. CRC press, 2009.

[85] D. Egfin Nirmala, V. Vaidehi, and S. I. Gandhi, “Data fusion using fuzzy logic for multi target tracking,” in *Proceedings of International Radar Symposium India*, 2005, pp. 75–80.

[86] S. Kashyap and J. Raol, “Fuzzy logic applications in filtering and fusion for target tracking,” *Defence Science Journal*, vol. 58, no. 1, p. 120, 2008.

[87] J. Yao, H. Zhang, X. Xiang, H. Bai, and Y. Zhao, “A 3-d printed redundant six-component force sensor with eight parallel limbs,” *Sensors and Actuators A: Physical*, vol. 247, pp. 90–97, 2016.

[88] C. Yuan, L.-P. Luo, Q. Yuan, J. Wu, R.-J. Yan, H. Kim, K.-S. Shin, and C.-S. Han, "Development and evaluation of a compact 6-axis force/moment sensor with a serial structure for the humanoid robot foot," *Measurement*, vol. 70, pp. 110–122, 2015.

[89] U. Kim, D.-H. Lee, Y. B. Kim, D.-Y. Seok, and H. R. Choi, "A novel six-axis force/torque sensor for robotic applications," *IEEE/ASME Transactions on Mechatronics*, vol. 22, no. 3, pp. 1381–1391, 2016.

[90] *Creo Parametric (2017)*, PTC, Boston, Massachusetts, 2017.

[91] SHARCNET, *Appendix a. glossary of general terms,* [Online; Accessed: 01-Apr-2019], 2013. [Online]. Available: https://www.sharcnet.ca/my/front/..

[92] Smithereen Pest Management Services, *Spiders*, [Online; Accessed: 28-Apr-2019], 2019. [Online]. Available: https://www.smithereen.com/residential/spider-removal-service..

[93] Turtle Time, Inc., *Anatomy*, [Online; Accessed: 01-Apr-2019], 2019. [Online]. Available: https://turtletime.org/sea-turtles/anatomy/..

[94] G. Domokos and P. L. Várkonyi, "Geometry and self-righting of turtles," *Proceedings of the Royal Society B: Biological Sciences*, vol. 275, no. 1630, pp. 11–17, 2008.

[95] Space for life, *Top view of the ideal structure*, [Online; Accessed: 01-Apr-2019], 2019. [Online]. Available: http://m.espacepourlavie.ca/en/file/6735..

[96] Ansys., *Ansys workbench*, [Online; Accessed: 01-Apr-2019], 2019. [Online]. Available: https://www.ansys.com/..

[97] L. Li, M. Zhang, M. Rong, and W. Ruan, "Studies on the transformation process of pvdf from α to β phase by stretching," *RSC Advances*, vol. 4, no. 8, pp. 3938–3943, 2014.

[98] TI.com, *Ina333 data sheet, product information and support*, [Online; Accessed: 01-Jun-2021], 2021. [Online]. Available: https://www.ti.com/product/INA333..

[99] TI.com., *Ref5025 data sheet, product information and support*, [Online; Accessed: 01-Jun-2021], 2021. [Online]. Available: https://www.ti.com/product/REF5025..

[100] T. J. Ross *et al.*, *Fuzzy logic with engineering applications.* Wiley Online Library, 2017, vol. 4.

[101] C.-C. Lee, "Fuzzy logic in control systems: Fuzzy logic controller. i and ii," *IEEE Transactions on systems, man, and cybernetics*, vol. 20, no. 2, pp. 404–418, 1990.

[102] M. Sugeno, “An introductory survey of fuzzy control,” *Information sciences*, vol. 36, no. 1-2, pp. 59–83, 1985.

[103] Mathworks. (2020). “Sugeno fuzzy inference system - matla.”

[104] *MATLAB version 9.7.0.1296695 (R2019b)*, The Mathworks, Inc., Natick, Massachusetts, 2019.

[105] Mathworks. (2020). “Tuning fuzzy inference systems- matlab $+.2777em\Gamma$”3026$+.2777em$ simulink.”

[106] Mathworks. (2020). “Fuzzy clustering- matlab & simulink.”

[107] J. C. Bezdek, *Pattern recognition with fuzzy objective function algorithms*. Springer Science & Business Media, 2013.

[108] Mathworks. (2020). “Fuzzy c-means clustering - matlab fcm.”

[109] S. L. Chiu, “Fuzzy model identification based on cluster estimation,” *Journal of Intelligent & fuzzy systems*, vol. 2, no. 3, pp. 267–278, 1994.

[110] Mathworks. (2020). “Find cluster centers using subtractive clustering - matlab subclust.”

[111] J. Mendel, H. Hagras, W.-W. Tan, W. W. Melek, and H. Ying, *Introduction to type-2 fuzzy logic control: theory and applications*. John Wiley & Sons, 2014.

[112] Mathworks. (2020). “Convert type-1 fuzzy inference system into type-2 fuzzy inference system - matlab converttotype2.”

[113] N. N. Karnik and J. M. Mendel, “Centroid of a type-2 fuzzy set,” *information SCiences*, vol. 132, no. 1-4, pp. 195–220, 2001.

[114] T. J. Ross *et al.*, *Fuzzy logic with engineering applications*. Wiley Online Library, 2004, vol. 2.

[115] R. S. Figliola and D. E. Beasley, *Theory and design for mechanical measurements*, 2001.

[116] J. Sirohi and I. Chopra, “Fundamental understanding of piezoelectric strain sensors,” *Journal of intelligent material systems and structures*, vol. 11, no. 4, pp. 246–257, 2000.

[117] Z. Ounaies, C. Park, K. Wise, E. Siochi, and J. Harrison, “Electrical properties of single wall carbon nanotube reinforced polyimide composites,” *Composites science and technology*, vol. 63, no. 11, pp. 1637–1646, 2003.

[118] C. Hu, C. Liu, L. Chen, and S. Fan, “Semiconductor behaviors of low loading multiwall carbon nanotube/poly (dimethylsiloxane) composites,” *Applied Physics Letters*, vol. 95, no. 10, p. 103 103, 2009.

[119] A. Alizadeh Sahraei, M. Ayati, M. Baniassadi, D. Rodrigue, M. Baghani, and Y. Abdi, “Ac and dc electrical behavior of mwcnt/epoxy nanocomposite near percolation threshold: Equivalent circuits and percolation limits,” *Journal of Applied Physics*, vol. 123, no. 10, p. 105 109, 2018.

[120] N. Shehata, E. Elnabawy, M. Abdelkader, A. H. Hassanin, M. Salah, R. Nair, and S. Ahmad Bhat, “Static-aligned piezoelectric poly (vinylidene fluoride) electrospun nanofibers/mwcnt composite membrane: Facile method,” *Polymers*, vol. 10, no. 9, p. 965, 2018.

[121] A. M. Vinogradov, S. C. Schumacher, and E. M. Rassi, “Dynamic response of the piezoelectric polymer pvdf,” *International Journal of Applied Electromagnetics and Mechanics*, vol. 22, no. 1-2, pp. 39–51, 2005.

[122] Mathworks. (2021). “System identification toolbox,” [Online]. Available: https://www.mathworks.com/help/ident/index.html..

[123] Mathworks. (2021). “Piecewise-linear nonlinearity estimator object,” [Online]. Available: https://www.mathworks.com/help/ident/ref/pwlinear.html..

[124] Mathworks. (2021). “Sigmoid network function,” [Online]. Available: https://www.mathworks.com/help/ident/ref/sigmoidnet.html..

[125] M. Sugeno, *Industrial applications of fuzzy control*. Elsevier Science Inc., 1985.

[126] Mathworks, *Type-2 fuzzy inference systems- matlab and simulink*, 2020. [Online]. Available: https://www.mathworks.com/help/fuzzy/type-2-fuzzy-inference-systems..

[127] Quora. (2021). “How much data is required for machine learning?” [Online]. Available: https://www.quora.com/How-much-data-is-required-for-machine-learning.

A. OUTPUT MEMBERSHIP FUNCTIONS (MFS) APPENDIX

Table A.1. Output MFs of DPPF's FISs under Z-loading.

Test- Hz	Fis	Output MFs	a_i	b_i	c_i
Z-2HZ	+X	out1cluster1	-18.6921	-4.3283	4.63E-05
		out1cluster2	-6.042	-5.5301	4.99E-05
		out1cluster3	3.6091	-4.8991	-3.15E-05
		out1cluster4	3.7416	-3.4612	2.38E-05
		out1cluster5	-1024.3	559.7861	-0.0467
		out1cluster6	-3732.9	3265.2	0.2674
		out1cluster7	-14.91	-3.6186	0.000282
		out1cluster8	-89.3313	11.7371	-0.0011
		out1cluster9	-1064.6	515.2736	0.0667
		out1cluster10	-3872.4	2929.9	-0.2937
	-Y	out1cluster1	-5.7835	5.1515	-2.83E-06
		out1cluster2	28.2659	-3.4234	-0.0048
		out1cluster3	18.3309	2.9623	0.0041
	-X	out1cluster1	11.76	11.653	0.001
		out1cluster2	11.8362	12.8343	-0.0011
		out1cluster3	15.8392	28.2399	-9.36E-05
		out1cluster4	16.2731	28.1546	2.58E-05
	+Y	out1cluster1	-1.1242	1.6413	1.15E-05
		out1cluster2	0.1947	2.0732	-2.81E-05
		out1cluster3	-0.8625	0.8262	1.09E-05
		out1cluster4	-0.4849	0.7868	-1.3E-05
		out1cluster5	-11.4761	55.9432	-0.000585
		out1cluster6	-0.907	0.4297	1.43E-05
		out1cluster7	0.9669	1.5211	7.19E-05
		out1cluster8	0.0308	0.0408	-1.49E-05
		out1cluster9	2.8924	-8.9447	0.000245
		out1cluster10	0.4942	-0.393	-1.62E-05
		out1cluster11	-1.2275	0.2507	1.79E-05
		out1cluster12	-0.6764	0.9381	1.44E-05
		out1cluster13	7.0307	29.0944	-0.0011
		out1cluster14	-0.8533	0.6338	1.19E-05
		out1cluster15	-0.5852	1.1704	-1.21E-05
		out1cluster16	-0.5096	0.9907	-5.67E-06
		out1cluster17	1.586	18.0592	-5.87E-05
Z-5Hz	+X	out1cluster1	-0.4792	0.504	-1.43E-07
		out1cluster2	-0.4726	0.4946	9.4E-08
		out1cluster3	-0.444	0.4753	1.51E-08
	-Y	out1cluster1	-4.2569	-6.2197	-0.000118
		out1cluster2	0.1485	-12.1865	0.000209
		out1cluster3	36.1703	1.8492	0.000104
		out1cluster4	42.3428	-54.1537	0.000308
		out1cluster5	-47.3886	31.181	-0.000179
		out1cluster6	-10.5971	-18.9448	9.07E-05
		out1cluster7	15.7728	33.5159	-0.000122
	-X	out1cluster1	-4.2569	-6.2197	-0.000118
		out1cluster2	0.1485	-12.1865	0.000209
		out1cluster3	36.1703	1.8492	0.000104
		out1cluster4	42.3428	-54.1537	0.000308
		out1cluster5	-47.3886	31.181	-0.000179
		out1cluster6	-10.5971	-18.9448	9.07E-05
		out1cluster7	15.7728	33.5159	-0.000122
	+Y	out1cluster1	-0.3148	0.3876	4.12E-07
		out1cluster2	-0.2754	0.3356	-1.16E-07
		out1cluster3	-0.2431	0.3427	-1.71E-07
Z-10HZ	+X	out1cluster1	-2.2896	1.9093	9.68E-06
		out1cluster2	-2.4167	2.0011	-1.09E-05
		out1cluster3	12.5578	-4.3778	-6.26E-04
		out1cluster4	13.2965	-4.8177	6.48E-04
	-Y	out1cluster1	-3.3416	0.1096	1.49E-04
		out1cluster2	-3.0242	0.1551	-1.31E-04
		out1cluster3	-10.9777	10.8339	-4.29E-04
		out1cluster4	-11.2774	10.8188	4.37E-04
	-X	out1cluster1	-1.1007	-0.2414	7.21E-05
		out1cluster2	-1.1507	-0.1864	-6.92E-05
		out1cluster3	2.7315	-1.4938	-1.08E-04
		out1cluster4	2.5059	-1.3117	1.02E-04
	+Y	out1cluster1	0.0178	1.0664	-4.43E-05
		out1cluster2	0.3024	0.9825	5.34E-05
		out1cluster3	-0.7207	3.5961	-3.78E-05
		out1cluster4	-0.7469	3.8243	3.82E-05
		out1cluster1	26.3974	-13.903	-5.44E-04
Z-100HZ	+X	out1cluster2	10.4712	-1.1882	2.50E-04
		out1cluster3	16.507	17.6723	1.56E-04
		out1cluster4	9.2137	15.3821	8.62E-05
	-Y	out1cluster1	16.9416	-0.293	-2.80E-04
		out1cluster2	5.7185	0.5228	3.00E-05
		out1cluster3	5.6718	9.4297	-7.63E-05
		out1cluster4	-8.0349	25.0062	3.26E-04
	-X	out1cluster1	16.7447	21.4876	-6.25E-04
		out1cluster2	16.9537	21.9658	6.36E-04
		out1cluster3	5.48E+03	-4.32E+03	-0.2811
		out1cluster4	5.51E+03	-4.34E+03	0.2812
	+Y	out1cluster1	-10.9161	-63.219	1.13E-04
		out1cluster2	-12.6432	-65.0578	-1.12E-04
		out1cluster3	-9.58E+03	3.91E+03	-0.1768
		out1cluster4	-8.11E+03	4.98E+03	-0.2846
		out1cluster5	-8.32E+03	4.95E+03	0.2933
		out1cluster6	224.3264	110.743	-0.0035
		out1cluster7	236.8641	113.1056	0.0036
		out1cluster8	-29.0329	-465.914	0.0041
		out1cluster9	-9.40E+03	3.89E+03	0.1734
		out1cluster10	-32.414	-470.359	-0.0042

Table A.2. Output MFs of DPPF's FISs under X-loading.

Test- Hz	Fis	Output MFs	a_i	b_i	c_i
X-2HZ	+X	out1cluster1	-84.192	-197.934	-0.0025
		out1cluster2	-41.974	-44.6608	-0.0014
		out1cluster3	-12.1306	-55.1845	0.0043
		out1cluster4	-223.624	153.4198	0.0475
		out1cluster5	-2.05E+04	-6.14E+03	-0.4208
		out1cluster6	2.90E+03	519.6405	0.1269
		out1cluster7	-415.835	-619.978	-0.0398
		out1cluster8	-472.083	-921.506	0.1049
		out1cluster9	-713.214	5.33E+03	0.3265
		out1cluster10	-9.12E+03	-2.80E+03	-1.3921
		out1cluster11	-3.38E+03	-2.37E+03	0.7935
		out1cluster12	-1.67E+04	1.64E+04	5.0209
		out1cluster13	-1.90E+03	-5.68E+03	1.2734
		out1cluster14	1.41E+05	-1.46E+05	101.1167
		out1cluster15	-1.78E+04	8.96E+03	-9.3378
		out1cluster16	-3.25E+04	4.57E+03	-1.7929
		out1cluster17	2.39E+03	-126.361	-0.8759
		out1cluster18	-1.85E+03	1.04E+03	-0.5501
		out1cluster19	2.10E+05	-1.22E+05	-96.9144
	-Y	out1cluster1	12.439	-8.2027	-2.03E-04
		out1cluster2	8.5709	-8.4527	1.60E-04
		out1cluster3	5.9945	-5.3571	2.00E-04
		out1cluster4	8.5439	0.7184	-1.81E-04
		out1cluster5	-30.741	99.2914	-0.0016
		out1cluster6	-272.544	995.1122	0.0378
		out1cluster7	140.1235	13.3553	0.0031
		out1cluster8	21.001	239.9118	0.0129
		out1cluster9	131.3706	91.1069	-0.0023
		out1cluster10	-457.382	1.25E+03	-0.0711
	-X	out1cluster1	-1.6974	1.6674	-4.48E-05
		out1cluster2	-1.9878	1.5274	-6.62E-05
		out1cluster3	-2.1631	1.4805	-1.34E-05
		out1cluster4	-1.3983	1.2891	5.45E-05
	+Y	out1cluster1	-0.9117	0.8113	-4.93E-06
		out1cluster2	-0.7996	1.1097	3.37E-06
		out1cluster3	-0.8713	1.0594	-3.27E-06
		out1cluster4	-0.8954	0.5327	-6.27E-06
		out1cluster5	2.5174	4.3588	1.04E-05
		out1cluster6	-1.1236	2.1871	8.37E-06
		out1cluster7	532.9211	310.299	0.0073
		out1cluster8	11.8428	2.8521	-1.15E-04
		out1cluster9	0.7994	-7.7464	5.99E-05
		out1cluster10	-1.8207	-8.2315	-7.84E-06
		out1cluster11	3.14E+04	-1.53E+04	0.1366
		out1cluster12	-32.6398	-457.466	0.0022
		out1cluster13	611.6531	41.6244	-0.0135
		out1cluster14	28.9781	-226.91	-5.02E-04
		out1cluster15	9.23E+03	-1.10E+04	0.0037
		out1cluster16	3.88E+03	-7.15E+03	-0.1516
		out1cluster17	-0.6209	1.7248	1.68E-06
		out1cluster18	5.61E+03	-4.65E+03	-0.1231
		out1cluster19	2.02E+03	-4.64E+03	0.046
		out1cluster20	9.01E+03	523.555	0.1059
		out1cluster21	2.65E+04	-2.53E+04	-0.1973
X-5HZ	+X	out1cluster1	0.2788	0.043	1.85E-04
		out1cluster2	0.0864	0.198	-1.67E-04
		out1cluster3	30.5643	-29.9217	0.0065
		out1cluster4	24.4701	-23.3402	-0.0049
		out1cluster5	3.3951	0.2147	-4.89E-04
		out1cluster6	2.802	0.3415	4.17E-04
		out1cluster7	25.2346	-39.2645	-0.0064
		out1cluster8	18.4633	-29.4487	0.0046
		out1cluster9	10.1426	3.0929	-4.32E-04
		out1cluster10	10.3811	5.5059	7.49E-04
	-Y	out1cluster1	-1.4905	-1.3609	6.29E-05
		out1cluster2	-1.7096	-1.8262	-8.50E-05
		out1cluster3	6.1372	-4.9052	-1.17E-04
		out1cluster4	6.9134	-5.9286	1.36E-04
	-X	out1cluster1	65.4606	-9.5707	0.0047
		out1cluster2	58.244	-1.3455	-0.0046
		out1cluster3	59.1946	1.3564	0.0039
		out1cluster4	176.1687	103.0262	-0.015
		out1cluster5	1.96E+03	2.35E+03	-0.2239
		out1cluster6	1.01E+03	560.8735	0.002
		out1cluster7	-34.1221	-59.51	-0.0207
		out1cluster8	1.34E+03	1.06E+03	0.2491
		out1cluster9	1.51E+04	4.53E+04	-6.0318
		out1cluster10	1.85E+03	1.09E+04	1.0874
		out1cluster11	-3.33E+05	-1.98E+05	-21.3774
X-5HZ		out1cluster12	-2.17E+03	-1.99E+03	0.0216
		out1cluster13	-1.22E+05	9.97E+04	-59.0082
		out1cluster14	-6.42E+03	8.75E+03	-1.162
		out1cluster15	-1.04E+04	-3.71E+03	0.1403
		out1cluster16	-4.59E+05	-1.31E+05	-38.4287
		out1cluster17	-6.25E+04	-4.54E+04	10.5055
	+Y	out1cluster1	-0.52	0.3224	8.26E-06
		out1cluster2	-0.593	0.1932	-1.21E-05
		out1cluster3	-0.5366	0.426	-5.05E-06
		out1cluster4	-0.5706	0.3016	5.30E-06
X-10 HZ	+X	out1cluster1	-0.545	1.5057	-3.50E-05
		out1cluster2	-0.3735	1.1334	6.25E-06
		out1cluster3	-0.5479	0.446	-3.48E-05
		out1cluster4	-0.5204	0.6507	2.33E-05
		out1cluster5	-1.296	1.0616	-5.79E-05
		out1cluster6	-1.2937	1.0608	5.78E-05
		out1cluster7	-1.144	0.4083	-5.05E-05
		out1cluster8	-1.1734	0.4324	5.11E-05
		out1cluster9	-1.1996	0.7083	-4.84E-05
		out1cluster10	-1.2263	0.709	4.99E-05
		out1cluster11	-1.1099	0.1439	5.87E-05
		out1cluster12	-0.923	0.2902	-4.77E-05
		out1cluster13	-1.3863	1.6408	8.36E-05
		out1cluster14	-1.4065	1.6581	-8.55E-05
		out1cluster15	-0.5414	-0.3193	8.14E-05
	-Y	out1cluster1	1.6482	8.9167	-7.46E-05
		out1cluster2	-1.3315	14.9083	1.04E-04
		out1cluster3	-35.2767	20.956	-1.29E-04
		out1cluster4	-23.4032	14.5	8.09E-05
		out1cluster5	2.2076	-4.6058	2.01E-05
		out1cluster6	3.2392	-5.5306	-2.22E-05
		out1cluster7	12.8294	-10.2837	4.36E-05
		out1cluster8	7.2401	-8.4009	2.91E-05
		out1cluster9	14.757	-12.4949	-4.92E-05
		out1cluster10	8.4732	-9.6109	-3.30E-05
	-X	out1cluster1	-1.6459	1.5646	2.77E-06
		out1cluster2	-1.7662	1.6133	3.58E-06
		out1cluster3	-0.7788	-0.9548	1.46E-04
		out1cluster4	-0.7207	-0.853	-1.43E-04
	+Y	out1cluster1	-1.191	1.016	-4.67E-06
		out1cluster2	-1.5697	1.3578	5.96E-06
		out1cluster3	-6.0682	10.2577	3.79E-05
		out1cluster4	-5.9101	5.4346	6.99E-06
		out1cluster5	3.2722	2.2541	-2.41E-05
		out1cluster6	11.0544	-0.1955	6.01E-05
		out1cluster7	-10.9899	3.3524	-3.18E-05
		out1cluster8	-7.0721	6.7829	-2.65E-05
		out1cluster9	-1.0801	1.1647	4.62E-06
		out1cluster10	-1.084	1.1524	-4.58E-06
		out1cluster11	0.1461	0.017	7.21E-07
		out1cluster12	-0.1317	0.2919	-1.67E-06
X-100 HZ	+X	out1cluster1	-1.4752	-0.4392	-2.49E-04
		out1cluster2	-2.6495	-0.1985	3.63E-04
		out1cluster3	-0.249	-0.8498	-1.17E-04
		out1cluster4	-1.4303	0.5691	9.24E-06
	-Y	out1cluster1	1.044	-1.1937	-4.61E-06
		out1cluster2	0.7511	-1.3216	1.01E-05
		out1cluster3	3.3557	-2.4532	3.09E-05
		out1cluster4	3.4843	-2.8565	-3.39E-05
	-X	out1cluster1	760.4255	-805.295	-0.0829
		out1cluster2	7.11E+03	-8.57E+03	1.0141
		out1cluster3	-4.60E+03	-9.58E+03	-2.8552
		out1cluster4	7.77E+03	4.45E+03	-1.2368
		out1cluster5	9.31E+03	-1.61E+03	2.3239
X-100 HZ	-X	out1cluster6	8.66E+03	-9.33E+03	-1.1557
		out1cluster7	3.69E+03	-1.41E+04	1.7218
		out1cluster8	2.71E+03	-1.29E+04	-1.5927
		out1cluster9	-8.01E+03	-4.75E+03	1.2893
		out1cluster10	675.0596	-937.228	0.0829
	+Y	out1cluster1	0.3918	0.8488	2.47E-05
		out1cluster2	-1.8983	-0.1998	2.77E-05
		out1cluster3	1.6663	-6.4185	6.07E-05
		out1cluster4	3.8806	-8.2207	-9.16E-05

Table A.3. Output MFs of EPPF's FISs for +X and +Y beams.

EPPF Test	Fis	Output MFs	a_i	b_i	c_i
X axis	+X	out1cluster1	3.73E+04	-7.23E+04	34.4906
		out1cluster2	6.15E+05	-5.25E+05	-148.138
		out1cluster3	3.24E+03	-3.49E+04	-0.6165
		out1cluster4	3.02E+04	-6.51E+05	155.2163
		out1cluster5	7.97E+05	-1.40E+06	-103.075
		out1cluster6	5.68E+04	-7.26E+04	-17.7237
		out1cluster7	2.84E+05	-1.71E+06	86.5956
		out1cluster8	1.60E+05	-9.61E+03	-84.437
		out1cluster9	1.64E+03	5.72E+03	-0.515
		out1cluster10	-2.84E+04	-4.11E+04	9.0149
		out1cluster11	2.08E+03	-4.51E+03	0.638
		out1cluster12	-8.04E+04	-1.67E+04	-41.5549
		out1cluster13	821.2761	-4.04E+03	-2.1087
		out1cluster14	1.46E+04	5.22E+03	-8.0885
		out1cluster15	-3.32E+04	-3.82E+03	-3.7645
		out1cluster16	-9.01E+03	-3.49E+03	-4.4817
		out1cluster17	-2.55E+04	4.59E+04	51.9311
		out1cluster18	204.0004	-1.24E+03	-0.4195
		out1cluster19	-1.31E+03	-1.37E+03	0.9266
Z axis	+X	out1cluster1	2.3511	-1.9337	-1.37E-05
		out1cluster2	1.884	7.2925	2.08E-04
		out1cluster3	-3.2969	5.1804	5.79E-05
		out1cluster4	0.2978	3.7088	-2.51E-05
		out1cluster5	-3.3198	5.2125	1.35E-05
		out1cluster6	1.4941	3.0858	2.91E-05
		out1cluster7	-5.1885	2.0377	7.53E-05
		out1cluster8	-4.4972	3.3208	-7.06E-06
		out1cluster9	-3.789	4.6766	4.15E-05
		out1cluster10	-3.5959	3.0177	-2.66E-05
		out1cluster11	-3.8889	4.7522	-4.17E-05
		out1cluster12	-3.7156	2.4385	3.56E-05
		out1cluster13	-4.2426	6.0324	-5.72E-05
		out1cluster14	-4.1947	3.4113	-3.36E-05
		out1cluster15	-4.2267	4.9222	4.16E-05
		out1cluster16	-4.1755	3.2601	3.45E-05
		out1cluster17	-4.865	8.147	-7.17E-05
		out1cluster18	-5.6256	4.5834	-4.86E-05
		out1cluster19	-5.1309	4.1396	3.61E-05
		out1cluster20	-3.3615	4.1612	2.43E-05
		out1cluster21	-10.1428	11.3692	-1.98E-06
		out1cluster22	-7.6057	7.1526	2.12E-06
		out1cluster23	-5.2313	7.5352	-5.51E-05
		out1cluster24	-4.5678	4.1432	3.79E-05
		out1cluster25	-2.5143	0.86	-4.16E-05
		out1cluster26	-0.26	-0.0495	-2.30E-07
		out1cluster27	-1.4331	0.6805	-1.91E-05
		out1cluster28	-2.5192	-0.3389	7.91E-05
		out1cluster29	-0.8505	1.3421	1.22E-05
		out1cluster30	-2.2786	-0.4761	6.95E-05
		out1cluster31	1.0591	0.2776	4.67E-05
		out1cluster32	0.0868	0.0649	-1.68E-05
		out1cluster33	1.6689	-3.4776	7.20E-05
X axis	+Y	out1cluster1	-0.9977	0.9919	6.96E-08
		out1cluster2	-1.1185	1.0659	-1.02E-07
		out1cluster3	-1.1222	1.1164	-5.55E-07
Z axis	+Y	out1cluster1	14.1233	-3.7205	6.90E-04
		out1cluster2	12.9294	-2.5603	-6.22E-04
		out1cluster3	9.7391	-6.9035	-4.63E-04
		out1cluster4	10.1483	-3.7944	3.51E-04
		out1cluster5	-7.7934	8.2718	1.98E-04
		out1cluster6	-7.266	9.7416	-2.08E-04

Table A.4. Output MFs of DPPF's FISs using data.

Test- Hz	Fis	Output MFs	a_i	b_i	c_i
0.1 Hz	a	out1cluster1	-0.8458	4.0471	1.41E-05
		out1cluster2	-0.5058	-4.8181	-1.40E-04
1 HZ	b	out1cluster1	-1.0722	1.2215	1.70E-04
		out1cluster2	-4.2313	0.4295	-4.50E-04
		out1cluster3	-0.8776	2.2633	3.83E-05
		out1cluster4	-2.3535	0.8841	-5.69E-04
		out1cluster5	-2.9421	1.5752	1.63E-04
100 HZ	c	out1cluster1	-0.96	0.2288	1.00E-05
		out1cluster2	-0.726	0.1023	3.65E-06

Table A.5. Output MFs of DPPF's FISs for Square and Triangular wave signals test.

Test	Output MFs	a_i	b_i	c_i
square signal	out1cluster1	0	0	0.1668
	out1cluster2	0	0	-0.2501
triangular signal	out1cluster1	0.2062	0	0.005
	out1cluster2	0.3059	0	-0.0085